

# **Search for compressed mass Higgsino production with low-momentum lepton tracks with the CMS experiment**

VON DER FAKULTÄT FÜR PHYSIK DER UNIVERSITÄT HAMBURG ZUR  
ERLANGUNG DES AKADEMISCHEN GRADES EINES DOKTORS DER  
NATURWISSENSCHAFTEN GENEHMIGTE DISSERTATION

VORGELEGT VON

YUVAL NISSAN

IM AUGUST 2022





**Abstract** This is the abstract

# Contents

<b>1</b>	<b>Introduction</b>	<b>1</b>
<b>2</b>	<b>Quantum Field Theory and The Standard Model</b>	<b>3</b>
2.1	Quantum field theory . . . . .	3
2.2	The Standard Model of particle physics . . . . .	3
2.2.1	The particle content . . . . .	3
<b>3</b>	<b>Supersymmetry</b>	<b>5</b>
3.0.1	Phenomenology of Higgsino production . . . . .	5
<b>4</b>	<b>Experimental setup</b>	<b>7</b>
4.1	The Large Hadron Collider . . . . .	7
4.2	The Compact Muon Solenoid experiment . . . . .	7
4.3	Simulation of events . . . . .	7
<b>5</b>	<b>Object reconstruction and identification of particles and jets</b>	<b>9</b>
5.1	Track reconstruction . . . . .	9
5.2	Electrons . . . . .	9
5.3	Muons . . . . .	9
5.4	Jets . . . . .	9
<b>6</b>	<b>Search for compressed Higgsinos with soft lepton tracks</b>	<b>11</b>
6.1	Signal models . . . . .	11
6.2	Previous searches . . . . .	11
6.3	Search strategy . . . . .	12
6.3.1	Final state with two muons . . . . .	12
6.3.2	Final state with one lepton and one track . . . . .	12
6.4	Signal signature and base selection . . . . .	13
6.4.1	Missing transverse energy . . . . .	13
6.4.2	Jets and hardronic activity . . . . .	13
6.4.3	Base selection . . . . .	14
6.4.4	Lepton kinematics . . . . .	17
6.4.4.1	Lepton $\eta$ and transverse momentum $p_T$ . . . . .	17
6.4.4.2	Invariant mass $m_{\ell\ell}$ . . . . .	20
6.4.4.3	Lepton separation $\Delta R$ . . . . .	21
6.4.5	Main drivers of sensitivity . . . . .	24
6.5	Simulated samples . . . . .	25
6.5.1	Standard Model simulated samples . . . . .	25
6.5.2	Signal simulated samples . . . . .	25
6.6	Object definition and selection . . . . .	26
6.6.1	Electrons . . . . .	26

6.6.2	Muons . . . . .	31
6.6.3	Scale factors . . . . .	35
6.6.4	Missing transverse energy . . . . .	40
6.6.5	Jets . . . . .	40
6.6.6	Tracks and multivariate selection . . . . .	41
6.6.7	Isolation . . . . .	45
6.7	Trigger . . . . .	49
6.8	Event selection . . . . .	50
6.8.1	Baseline selection . . . . .	50
6.8.2	Category selection . . . . .	51
6.8.2.1	Dilepton selection . . . . .	51
6.8.2.2	Exclusive track selection . . . . .	51
6.8.3	Boosted decision trees . . . . .	52
6.8.3.1	Dimuon category . . . . .	52
6.8.3.2	Exclusive track category . . . . .	55
6.9	Characterization and estimation of the Standard Model backgrounds . . . . .	58
6.9.1	Characterization of the Standard Model backgrounds . . . . .	58
6.9.1.1	Dimuon category . . . . .	60
6.9.1.2	Exclusive track category . . . . .	62
6.9.2	Estimation of the Standard Model backgrounds . . . . .	64
6.9.2.1	Jetty background estimation . . . . .	65
6.9.2.2	Ditau Drell-Yann background estimation . . . . .	67
6.9.2.3	Exclusive track background estimation . . . . .	70
6.10	Data control region plots . . . . .	72
6.11	Signal regions definition and optimization . . . . .	75
6.12	Systematic uncertainties . . . . .	77
6.12.1	Data driven transfer factors . . . . .	77
6.12.2	Data driven shape uncertainties . . . . .	77
6.12.3	Simulated background uncertainties . . . . .	78
6.13	Data quality aspects and background validation . . . . .	80
6.13.1	L1 prefire issue in 2016 and 2017 data . . . . .	80
6.13.2	EE noise in 2017 data . . . . .	80
6.13.3	HEM failure in 2018 data . . . . .	80
6.13.4	Same-sign validation plots . . . . .	80
6.14	Results and interpretation . . . . .	82
7	Summary	83
8	Latex stuff	85
8.1	Some examples . . . . .	85
8.1.1	Multiline comment . . . . .	85
8.1.2	Fixme note . . . . .	85
8.1.3	Tables . . . . .	85
8.1.4	Cross References . . . . .	85
8.1.5	Particles . . . . .	85
8.1.6	Citing . . . . .	85
8.1.7	Glossary . . . . .	85
8.1.8	Acronyms . . . . .	86
8.1.9	fractions . . . . .	86
8.1.10	Quarantine . . . . .	86

## *CONTENTS*

Glossary	89
Acronyms	91

## *CONTENTS*

# **Chapter 1**

## **Introduction**

This is a line in introduction. This is the introduction to the thesis.



# **Chapter 2**

## **Quantum Field Theory and The Standard Model**

**2.1 Quantum field theory**

**2.2 The Standard Model of particle physics**

**2.2.1 The particle content**



# Chapter 3

## Supersymmetry

### 3.0.1 Phenomenology of Higgsino production



# **Chapter 4**

## **Experimental setup**

One of the most useful methods to study the subatomic world of particle physics uses particle colliders. In such machines, particles are accelerated to very high speeds and energies, and smashed into each other. The particles that emerge from the collisions are then measured in a particle detector and then studied and analyzed. At the time of writing this thesis, the largest and most high energy collider to date is the Large Hadron Collider (LHC) located in Geneva, Switzerland, operated by the European Organization for Nuclear Research (CERN). For the present work, data from the Compact Muon Solenoid (CMS) experiment has been analyzed. In this chapter, the LHC is described in 4.1, while the CMS experiment is described in 4.2.

### **4.1 The Large Hadron Collider**

### **4.2 The Compact Muon Solenoid experiment**

### **4.3 Simulation of events**



# **Chapter 5**

## **Object reconstruction and identification of particles and jets**

### **5.1 Track reconstruction**

This is the track reconstruction page.

### **5.2 Electrons**

### **5.3 Muons**

### **5.4 Jets**



# Chapter 6

## Search for compressed Higgsinos with soft lepton tracks

### 6.1 Signal models

The signal models considered in this analysis are based on **Fixme Note:** fill in signal model stuff.

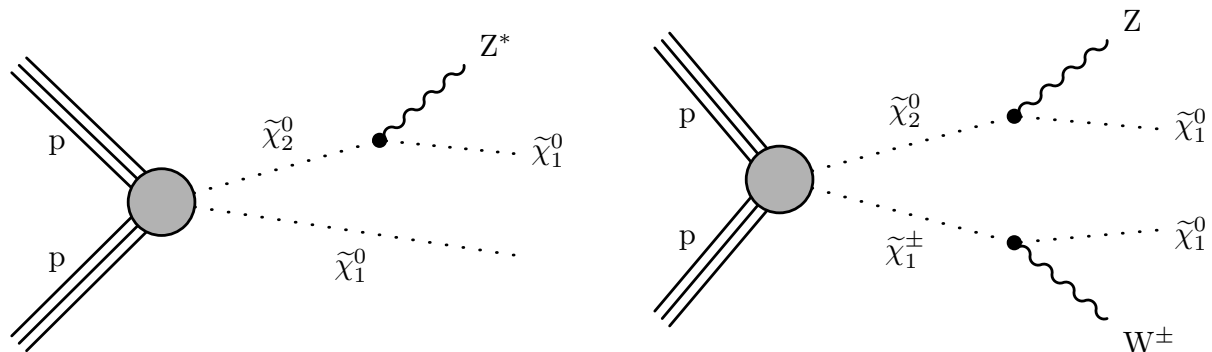


Figure 6.1: Production and decay of electroweakinos in the higgsino simplified model through  $\tilde{\chi}_2^0 \tilde{\chi}_1^0$  (left) and  $\tilde{\chi}_2^0 \tilde{\chi}_1^\pm$  (right).

**Fixme Note:** make sure we define the different deltaM somewhere

### 6.2 Previous searches

## 6.3 Search strategy

### 6.3.1 Final state with two muons

### 6.3.2 Final state with one lepton and one track

## 6.4 Signal signature and base selection

To develop an effective analysis strategy, the signal kinematics are studied and exploited. The production and decay of electroweakinos give rise to unique event characteristics that can be leveraged to differentiate the signal from the Standard Model (SM) background. Distributions of key observables from signal and background processes are compared in order to define a pre-selection or set of base cuts that retains the maximum signal while rejecting as much background as possible. All the following distributions of key observables were generated by weighting the simulated data to the Run II luminosity of  $\mathcal{L} = 135 \text{ fb}^{-1}$  and requiring at least one jet in the event with  $p_T \geq 30 \text{ GeV}$  and  $|\eta| < 2.4$ . Discussion is provided for each event property, and the incorporation of additional selection criteria is specified building toward the base selection.

### 6.4.1 Missing transverse energy

A driving factor for most searches for Dark Matter (DM) at the LHC is the presence of a DM candidate in the final state. The identity and properties of the particle (or particles in the case of multiple DM candidates) vary, but they do have much in common. In this Supersymmetry (SUSY) search, the DM candidate is the Lightest Supersymmetric Particle (LSP), assumed to be a neutralino. A neutral particle that does not interact electromagnetically or via the strong force (i.e., is colorless) will not be detected and will leave traces in the form of a transverse momentum imbalance, which is referred to as  $E_T^{\text{miss}}$  (missing transverse energy or missing transverse momentum). Because of R-parity conservation, the signal contains two DM candidates in the final state, which are the LSPs, the neutralinos  $\tilde{\chi}_1^0$ . Therefore, a considerable magnitude of  $E_T^{\text{miss}}$  is expected in the signal. As described in Section 6.6.4, a suitable proxy for the  $E_T^{\text{miss}}$  is the missing transverse hadronic energy, or  $H_T^{\text{miss}}$ , which is highly correlated with  $E_T^{\text{miss}}$ , but better suited to the definition of lepton isolation and its use in the background estimation methods. Both  $E_T^{\text{miss}}$  and  $H_T^{\text{miss}}$  observables are examined in Figure 6.2.

As expected,  $E_T^{\text{miss}}$  and  $H_T^{\text{miss}}$  are largely unaffected by the different choices for  $\Delta m$ , while the higgsino parameter  $\mu$  affects the distributions mainly through its falling production cross section as a function of the higgsino parameter  $\mu$ . The region of interest in order to be efficient with respect to the triggers is located at  $H_T^{\text{miss}} \geq 220 \text{ GeV}$ , as discussed in Section 6.7. Although this is a harsh and inefficient cut, it becomes apparent when examining the SM background in both regions of  $H_T^{\text{miss}} < 220 \text{ GeV}$  and  $H_T^{\text{miss}} \geq 220 \text{ GeV}$  to conclude that most of the sensitivity comes from the  $H_T^{\text{miss}} \geq 220 \text{ GeV}$  region, as the production of real  $H_T^{\text{miss}}$  (or  $E_T^{\text{miss}}$ ) results from the production of neutrinos in the event. These are much less common than Quantum Chromodynamics (QCD) events that dominate the  $H_T^{\text{miss}} < 220 \text{ GeV}$  region.

### 6.4.2 Jets and hardronic activity

As mentioned in the previous section, signal events tend to have small momentum imbalance. In order to induce significant missing transverse energy, some additional activity must take place within the events, and this most often comes in the form of one or more Initial State Radiation (ISR) jets. An ISR jet is created when one of the incoming protons emits radiation (such as a quark or a gluon) before the interaction. If a jet with sufficiently high  $p_T$  is emitted, the remainder of the interaction is recoiled against this jet and imparts momentum onto the system of invisible particles in the opposite direction. As a result, the boosted neutralinos  $\tilde{\chi}_1^0$  give rise to higher  $H_T^{\text{miss}}$ . As described in Section 6.6.5, the jets are required to have  $p_T \geq 30 \text{ GeV}$  and be located within the tracker acceptance ( $|\eta| < 2.4$ ). At least one such jet is required in each event. The distributions of the number of jets and the leading jet  $p_T$  are displayed in Figure 6.3.

The signal signature rarely includes a b-jet, that is, a jet resulting from the hadronization of a bottom quark. However, standard model top quark pair production leads to a large numbers

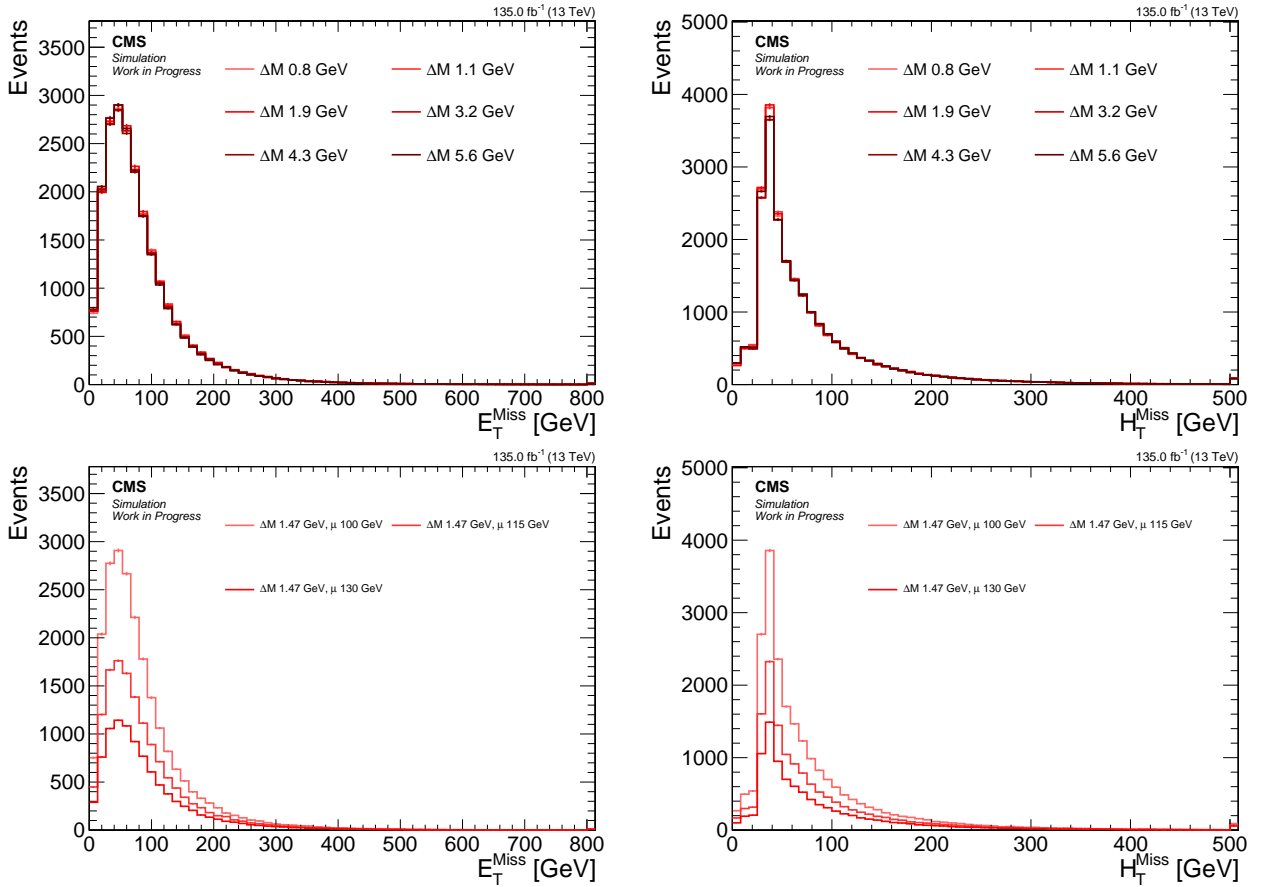


Figure 6.2: Signal distributions of  $E_T^{\text{miss}}$  (left) and  $H_T^{\text{miss}}$  (right) comparing various  $\Delta m$  with a fixed higgsino parameter  $\mu = 100\text{ GeV}$  (upper), and comparing various  $\mu$  with fixed  $\Delta m = 1.47\text{ GeV}$  (lower).

of events with significant missing transverse energy and two or more b-jets. To reject this background, events are vetoed if a b-jet is identified in the event. As described in Section 6.6.5, the DEEPCSV bottom flavor tagging discriminant with a medium working point is used. The multiplicity of b-tagged jets is shown in Figure 6.4, where the choice of number of b-tagged jets equals to zero appears well-justified.

As an ISR jet is required in the event, it is expected that the  $E_T^{\text{miss}}$  and the  $H_T^{\text{miss}}$  will be directed in the opposite direction of the jet, or at an azimuthal angle close to  $\pi$ . This feature is not as clearly observed in events with multiple jets in the SM background, such as those arising from QCD, where the missing transverse energy tends to align with the leading or sub-leading jet. To reduce the QCD background, a requirement of  $\min \Delta\phi(\vec{H}_T^{\text{miss}}, \vec{j}) > 0.4$  is imposed.

### 6.4.3 Base selection

The section is recapped by summarizing the base selection of the analysis. The base selection, also known interchangeably as the preselection, is applied to all analysis categories. It is listed in Table 6.4.3.

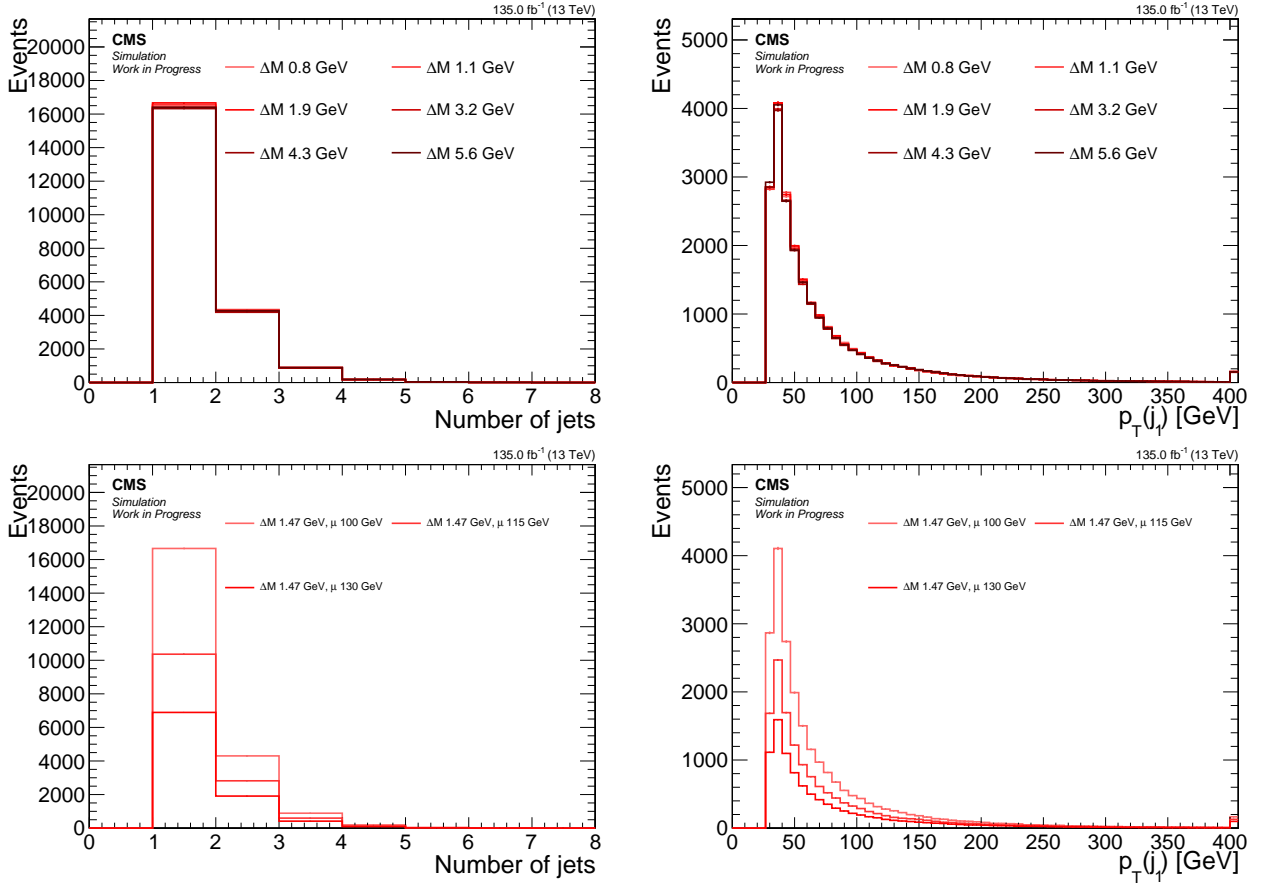


Figure 6.3: Signal distributions of *number of jets* (left) and *leading jet  $p_T$*  (right) comparing various  $\Delta m$  with a fixed higgsino parameter  $\mu = 100$  GeV (upper), and comparing various  $\mu$  with fixed  $\Delta m = 1.47$  GeV (lower).

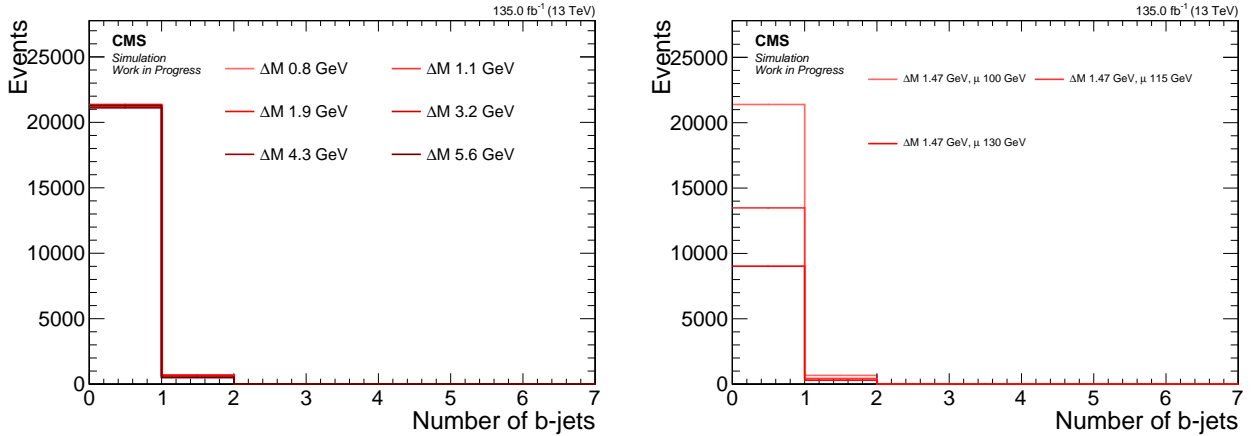


Figure 6.4: Signal distributions of *number of b-tagged jets* comparing various  $\Delta m$  with a fixed higgsino parameter  $\mu = 100$  GeV (left), and comparing various  $\mu$  with fixed  $\Delta m = 1.47$  GeV (right).

Table 6.1: The preselection criteria, which are applied to all analysis categories.

Variable	Value
$H_T^{\text{miss}} [\text{GeV}]$	$> 220$
$N_{\text{jets}} (p_T \geq 30 \text{ GeV} \text{ and }  \eta  < 2.4)$	$\geq 1$
$N_{\text{b-jets}} (p_T \geq 30 \text{ GeV} \text{ and }  \eta  < 2.4)$	$= 0$
$\min \Delta\phi (\vec{H}_T^{\text{miss}}, \vec{j})$	$> 0.4$

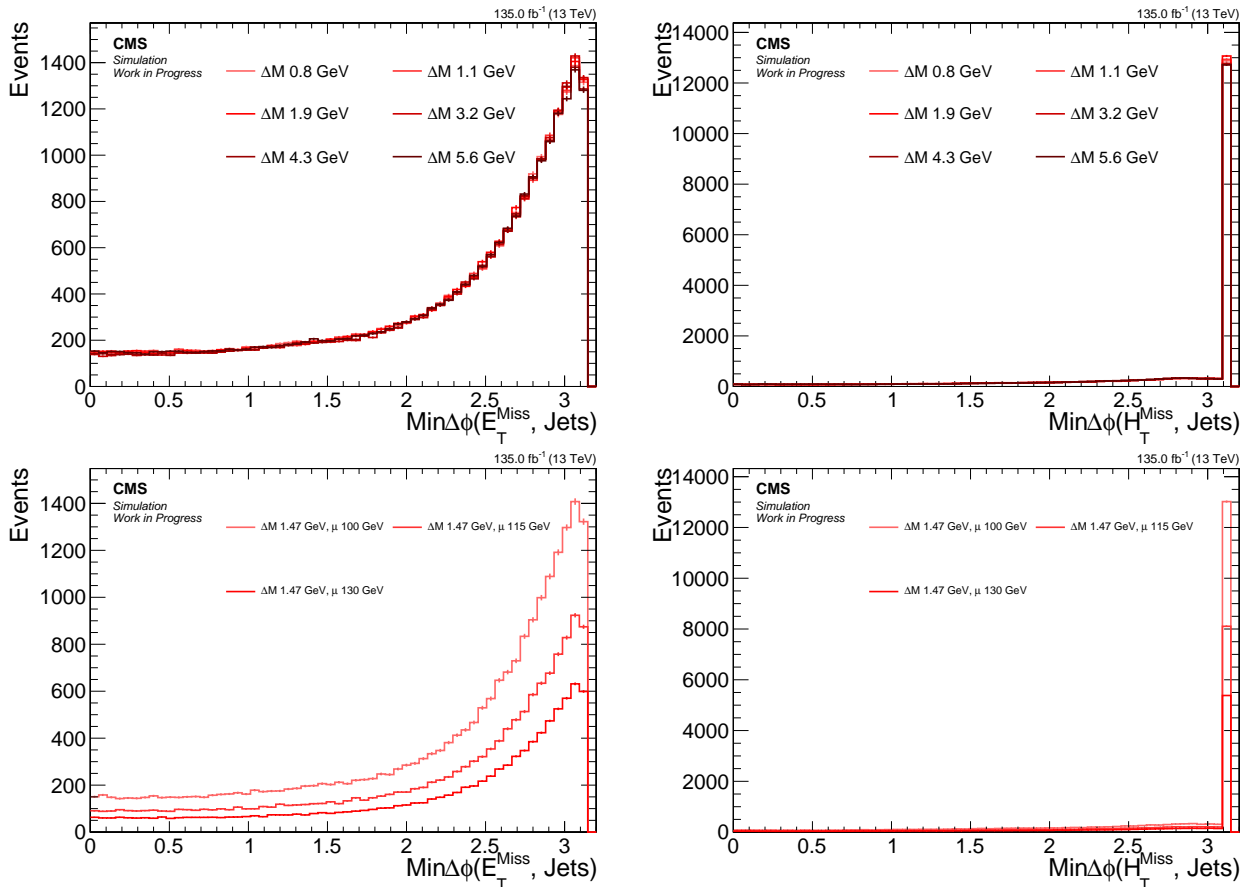


Figure 6.5: Signal distributions of  $\text{min} \Delta\phi(\vec{E}_T^{\text{miss}}, \vec{j})$  (left) and  $\text{min} \Delta\phi(\vec{H}_T^{\text{miss}}, \vec{j})$  (right) comparing various  $\Delta m$  with a fixed higgsino parameter  $\mu = 100 \text{ GeV}$  (upper), and comparing various  $\mu$  with fixed  $\Delta m = 1.47 \text{ GeV}$  (lower).

### 6.4.4 Lepton kinematics

The hadronic component of signal events has been the focus up until this point. However, the dilepton system contains the most distinctive features of the signal. To fully understand the unique phase space of the dilepton system, generator level distributions are examined first, followed by an exploration of the effects of reconstruction on those observables. Since the dimuon category is the most sensitive and because the logic applies analogously to the two-electron final state, the electron category is excluded from the following sections. The lepton kinematics change dramatically as a function of  $\Delta m$ . In contrast, the higgsino parameter  $\mu$  effects almost only the overall normalization due to the different production cross section. Therefore, the higgsino parameter is set to  $\mu = 100$  GeV in the following sections, with the  $\Delta m$  varied.

#### 6.4.4.1 Lepton $\eta$ and transverse momentum $p_T$

The signal acceptance and sensitivity are significantly impacted by the thresholds of the transverse momentum  $p_T$  distribution of the muons that make it through the reconstruction and identification. Details of the muon reconstruction and identification procedures are discussed in Section 5.3. The selection applied to the muons in this analysis is described in Section 6.6.2 and referred to as the *analysis selection*. This section aims to examine the importance of the  $p_T$  on the signal and its dilepton kinematic distributions.

The generator level distribution of  $p_T$ , or the so-called *truth* distributions, which do not exhibit any detector or reconstruction features, are examined first. The distribution of reconstructed  $p_T$  is then compared with the generator level distribution in Figure 6.6.

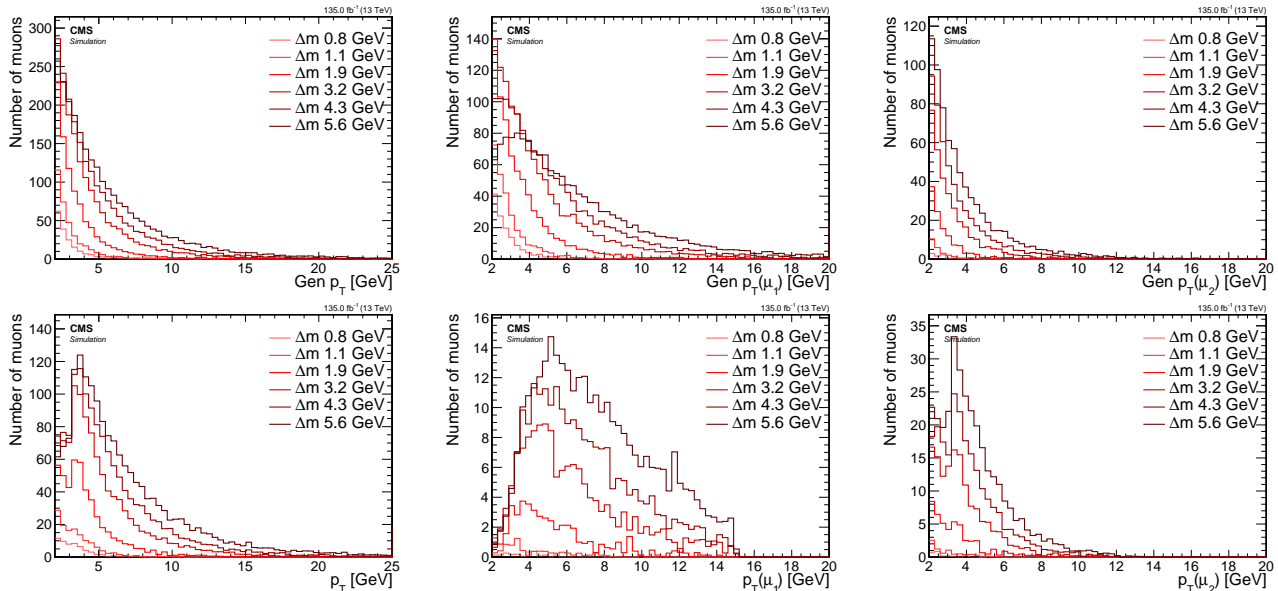


Figure 6.6: Signal  $p_T$  distributions for inclusive (left), leading muon  $\mu_1$  (middle), subleading muon  $\mu_2$  (right) at generator level (top) and reconstruction level passing analysis selection (bottom).

When comparing the generator level and reconstruction level inclusive  $p_T$  distributions, it becomes apparent that a reshaping occurs around 3 GeV. A significant proportion of the generated muons with  $p_T < 3$  GeV are lost in the reconstruction process. The subleading muon  $p_T$  distribution at the reconstruction level has a camel shape, whereby the efficiency drops below a  $p_T$  of 3 GeV to about half its maximum value and is only partially regained at  $p_T > 3$  GeV. This effect is due to the detector geometry and is more clearly visible when splitting the  $p_T$  distribution into a barrel ( $|\eta| < 1.2$ ) and encaps ( $|\eta| \geq 1.2$ ) portions, as shown in Figure 6.7.

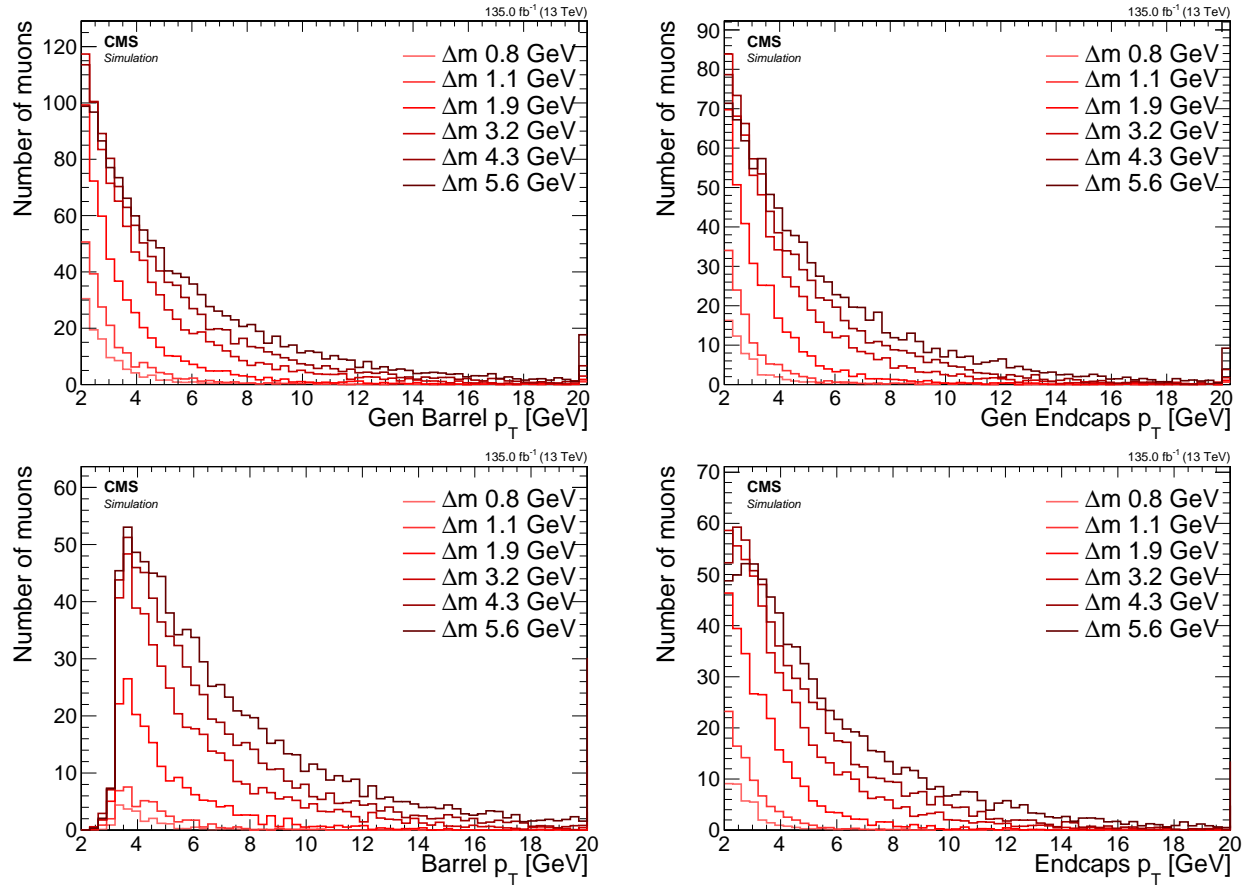


Figure 6.7: Signal inclusive  $p_T$  distributions for barrel  $|\eta| < 1.2$  (left) and endcaps  $|\eta| \geq 1.2$  (right) at generator level (top) and reconstruction level passing analysis selection (bottom).

When comparing the generator level distribution of the barrel muons on the top left with its reconstructed counterpart on the bottom left, Figure 6.7 shows that the barrel, shown on the left, is almost completely unable to reconstruct muons with  $p_T < 3$  GeV, while the endcaps, shown on the right, are able to do so. As demonstrated in the upcoming sections on  $m_{\ell\ell}$  and  $\Delta R$  (see 6.4.4.2 and 6.4.4.3), the relationship between these observables has consequences for the reshaping of kinematic distributions, as well as for signal acceptance in general. Access to low  $\Delta m$  signal points is crucially dependent on the low  $p_T$  region of  $2 \leq p_T \leq 3.5$  GeV, which is mainly achieved with the help of the muon chamber endcaps, as can be seen here.

Since the barrel and endcaps are separated by different regions of  $\eta$ ,  $|\eta| < 1.2$  for barrel and  $|\eta| \geq 1.2$  for endcaps, the muon  $\eta$  distributions merit further examination as well. They can be seen at Figure 6.8. The dimuon analysis channel only selects muons within the tracker range of  $|\eta| < 2.4$ . This is why the muons with  $|\eta| > 2.4$  are not present in the reconstruction plots on the bottom. It can be seen that the main effect of going from the inclusive  $|\eta|$  at the generator level to the reconstructed counterpart is the flattening of the distribution due to the loss of muons with  $|\eta| < 1.2$  in the barrel for muons with  $p_T < 3$  GeV.

With the understanding of the reconstruction effects on the  $p_T$  and  $\eta$  distributions of the muons, an examination of other kinematic variables of the dilepton system is now possible.

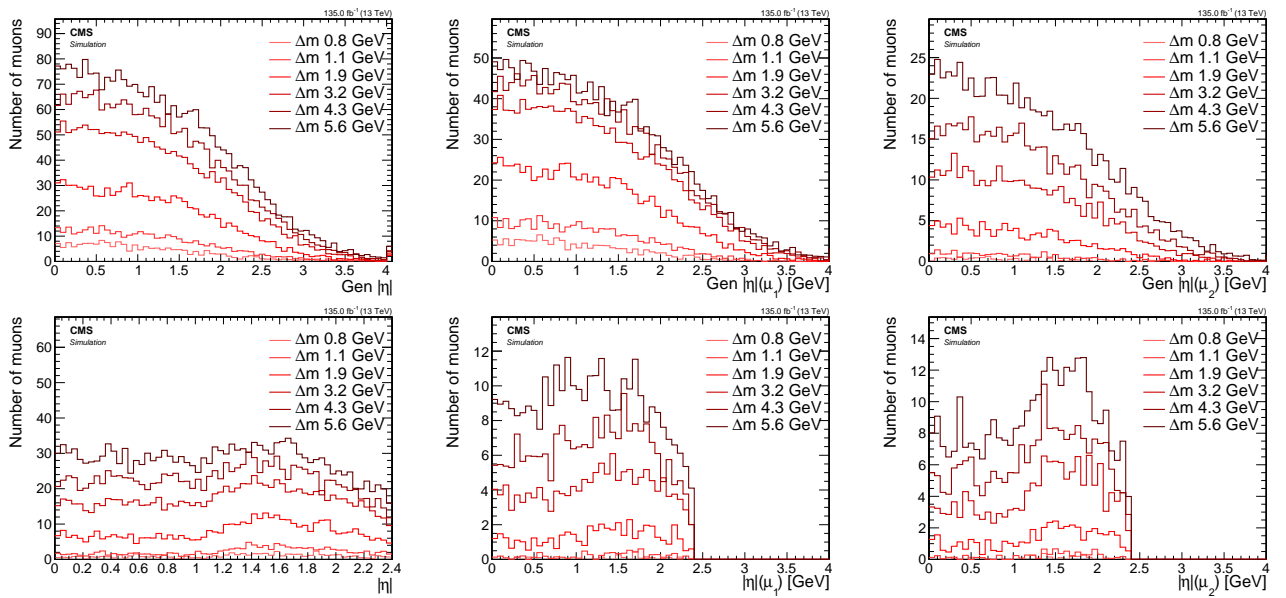


Figure 6.8: Signal  $|\eta|$  distributions for inclusive (left), leading muon  $\mu_1$  (middle), subleading muon  $\mu_2$  (right) at generator level (top) and reconstruction level passing analysis selection (bottom).

#### 6.4.4.2 Invariant mass $m_{\ell\ell}$

The invariant mass of the two leptons resulting from the decay of the  $\tilde{\chi}_2^0$  has a unique shape due to the limited allowed phase space of the 3-body decay. As the  $\tilde{\chi}_2^0$  decays into  $\tilde{\chi}_1^0$  and  $\ell^+\ell^-$  through a  $Z^*$ , the allowed phase space of the dilepton pair is restricted to the mass difference between  $\tilde{\chi}_2^0$  and  $\tilde{\chi}_1^0$ , that is,  $\Delta m$ . Therefore, the  $m_{\ell\ell}$  distribution is expected to have an edge at  $\Delta m$ . Distributions of the generator level invariant mass can be seen in Figure 6.9.

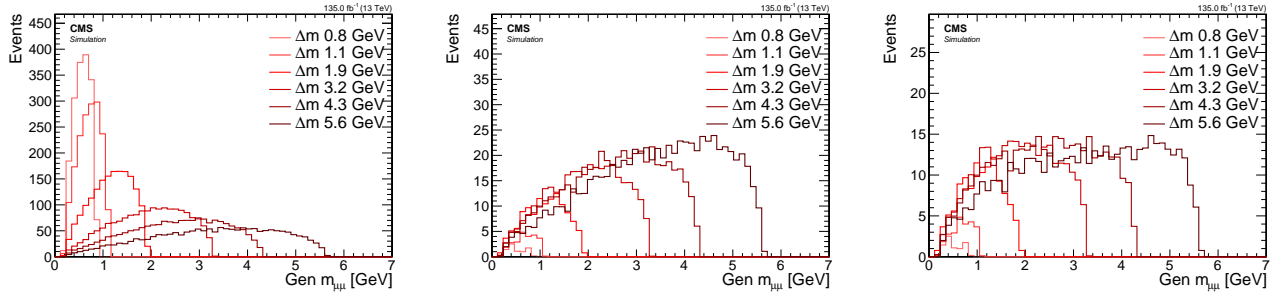


Figure 6.9: Signal generator level  $m_{\ell\ell}$  distributions with no cuts (left), with  $p_T(\mu_i) > 2 \text{ GeV}$ ,  $i = 1, 2$  (middle) and with the SOS orthogonality condition:  $p_T(\mu_i) > 2 \text{ GeV}$ ,  $p_T(\mu_2) \leq 3.5 \text{ GeV}$  or  $\Delta R \leq 0.3$  (right).

The inclusive distribution of the invariant mass of the muons  $m_{\mu\mu}$  is shown on the left. The edge of the  $m_{\mu\mu}$  distribution for each signal point is located right at the corresponding  $\Delta m$ . However, when the muons  $p_T$  is required to be  $p_T \geq 2 \text{ GeV}$ , the shape of the distribution shifts, due to the lower efficiency for small  $\Delta m$  values, as depicted in the middle plot. Lastly, the effect of orthogonalizing phase space to the SOS analysis is demonstrated in the rightmost plot. The effect is strongest in high  $\Delta m$  and quite subtle in low  $\Delta m$ .

To explain the reshaping that occurs to the  $m_{\mu\mu}$  distribution, the relationship between the  $p_T$  of the muons and the invariant mass is examined. One signal with low  $\Delta m$  of 1.13 GeV and one with high  $\Delta m$  of 5.63 GeV are selected for this analysis. The distributions are shown in Figure 6.10, leading muon denoted  $\mu_1$  while subleading muon is denoted  $\mu_2$ .

Earlier, it was established that the invariant mass distribution has an edge at  $\Delta m$ , and the value of  $\Delta m$  can be read from these plots. Another interesting feature is a lower edge in the  $\Delta m$  distribution at around  $\sim 0.2 \text{ GeV}$ , which is due to each muon having a mass of around  $\sim 0.1 \text{ GeV}$ . It is now clear that by requiring both muons to have  $p_T \geq 2 \text{ GeV}$ , a significant portion of the signal is lost. This effect becomes particularly substantial for the low  $\Delta m = 1.13 \text{ GeV}$  (top row). The magnitude of this effect is quantified by a cutflow, shown in Table 6.4.4.2, where each row represents a cut, and its efficiency is calculated by dividing the number of events passing the cut by the number of events in the previous line. The first line the number of events with exactly 2 muons at the generator level with at least one jet with  $p_T \geq 30 \text{ GeV}$  and  $|\eta| < 2.4$ . The event number is weighted to Run II luminosity of  $\mathcal{L} = 135 \text{ fb}^{-1}$ .

Table 6.2: Generator level efficiency on muons selections

Cut	Weighted number of events		Efficiency	
	$\Delta m = 1.13 \text{ GeV}$	$\Delta m = 5.63 \text{ GeV}$	$\Delta m = 1.13 \text{ GeV}$	$\Delta m = 5.63 \text{ GeV}$
Baseline	1710.7	1743.9	-	-
$p_T \geq 2 \text{ GeV}$	24.7	724.9	0.015	0.41
SOS orthogonality	24.7	490.6	1	0.68

Table 6.4.4.2 shows that for the low  $\Delta m$  of 1.13 GeV, the acceptance of the signal is significantly reduced by the  $p_T \geq 2 \text{ GeV}$  cut, with only 1.5% of the signal remaining. In contrast, the

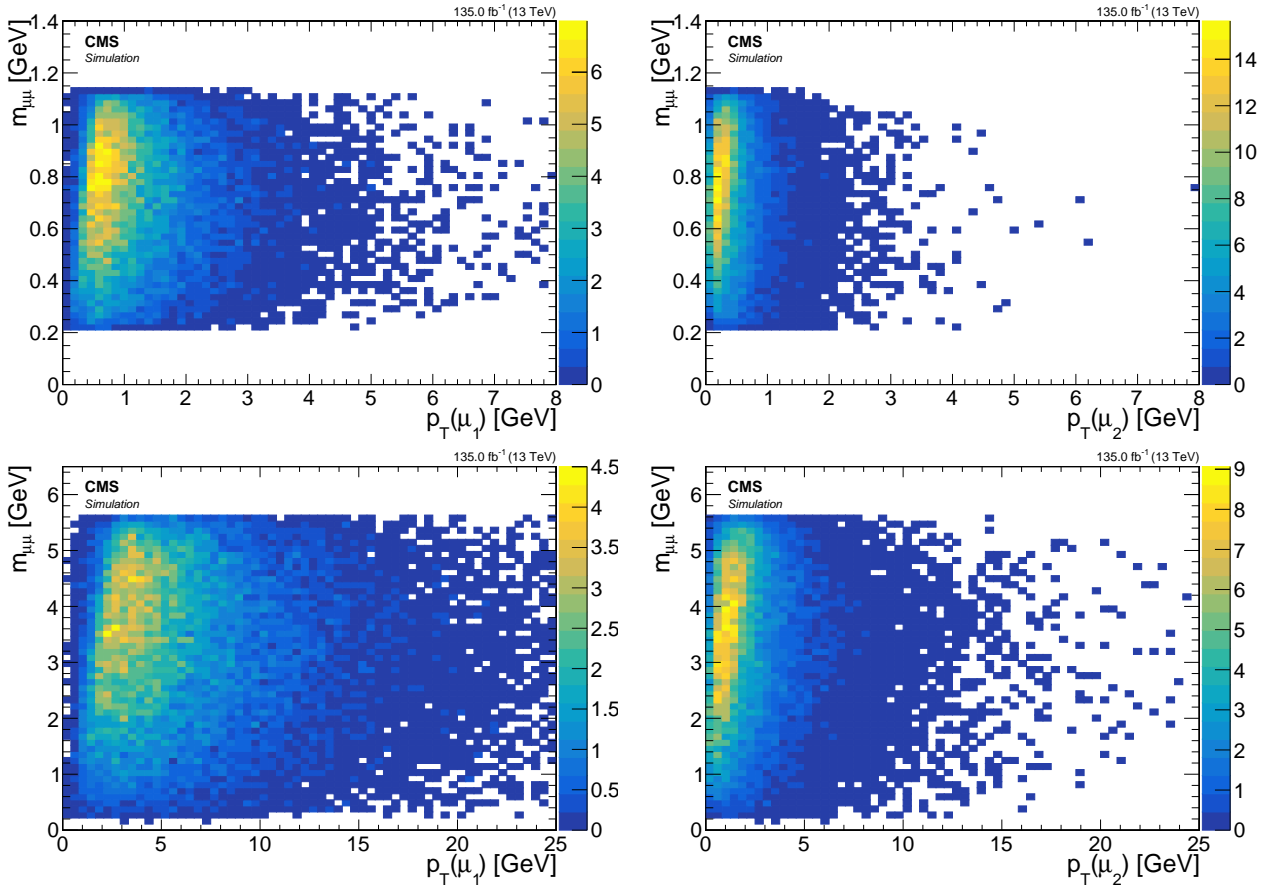


Figure 6.10: Signal  $m_{\mu\mu}$  vs.  $p_T$  for leading lepton  $\mu_1$  (left) and subleading lepton  $\mu_2$  (right) for  $\Delta m = 1.13 \text{ GeV}$  (top) and  $\Delta m = 5.63 \text{ GeV}$  (bottom).

orthogonality condition of requiring  $p_T(\mu_2) \leq 3.5 \text{ GeV}$  or  $\Delta R(\ell\ell) \leq 0.3$  does not affect it any further. The situation is different for the high  $\Delta m$  of  $5.63 \text{ GeV}$ , where the  $p_T$  cut rejects more than half of the signal and the SOS orthogonality condition rejects an additional two thirds.

It has been established that the  $p_T$  thresholds affect the  $m_{\ell\ell}$  distribution due to the relationship between the two variables. Next, it is investigated how the reconstruction discussed in Section 6.4.4.1 impacts the  $m_{\mu\mu}$  distribution. The distributions of the reconstructed  $m_{\mu\mu}$  can be seen in Figure 6.11. Comparing these distributions to the two right plots in Figure 6.9 not only are fewer events surviving the reconstruction, but also some  $\Delta m$  model points are peaking between  $1 \text{ GeV}$  to  $2 \text{ GeV}$  with the SOS orthogonality condition applied.

#### 6.4.4.3 Lepton separation $\Delta R$

The lepton separation is defined by the equation  $\Delta R = \sqrt{(\Delta\eta)^2 + (\Delta\phi)^2}$ , where  $\eta$  represents the pseudorapidity and  $\phi$  is the azimuthal angle measured in radians. The value of  $\Delta R$  is significant in this analysis because the produced leptons tend to be located in close proximity to each other and therefore are not easily isolated according to standard definitions. Special attention is given to ensuring that the collimated nature of the leptons can be used to differentiate signal leptons from the non-isolated leptons in the SM background. It is worth noting that, for the purposes of orthogonality, the requirement of  $\Delta R(\ell\ell) > 0.3$  utilized in previous SOS analyses [1] is reverted.

Similar to the invariant mass discussed in Section 6.4.4.2, we examine the distributions of  $\Delta R$  for various  $\Delta m$  options with different cuts applied to observe their effect. The left plot of Figure 6.12 shows that roughly the same number of events are produced for all  $\Delta m$  model

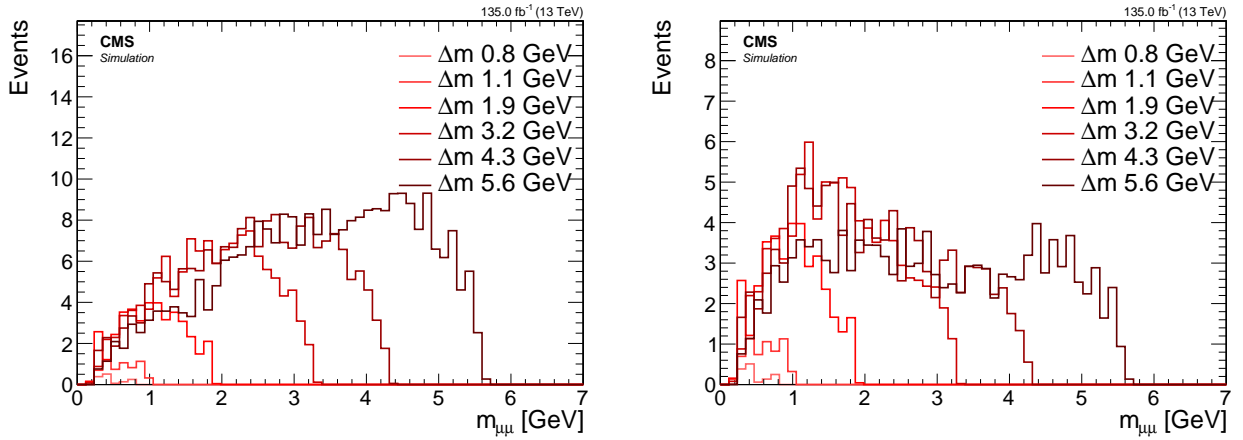


Figure 6.11: Distributions of reconstructed  $m_{\mu\mu}$  in signal events with analysis selection (left) and the additional SOS orthogonality condition (right).

points. However, when applying a cut of  $p_T(\mu) > 2 \text{ GeV}$ , a hierarchy of  $\Delta m$  points emerges, with fewer events as  $\Delta m$  becomes smaller (middle plot). The spike on the right plot is due to the SOS orthogonality condition, which requires  $\Delta R(\ell\ell) \leq 0.3$  as one of two conditions that must be satisfied.

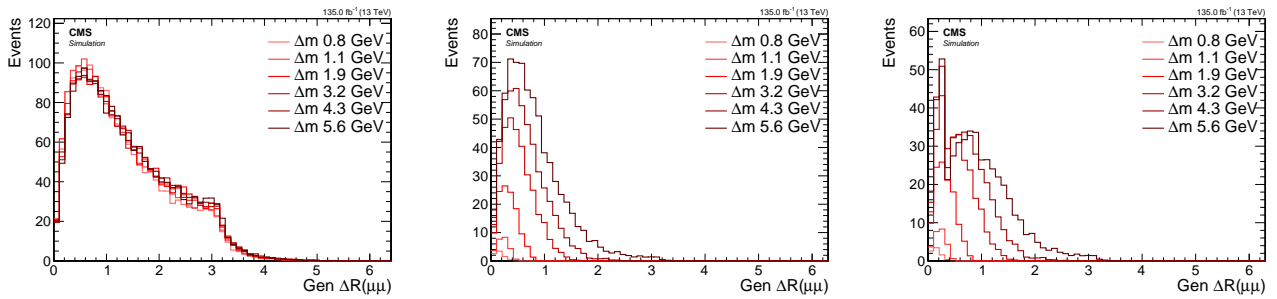


Figure 6.12: Signal generator level  $\Delta R$  distributions with no cuts (left), with  $p_T(\mu_i) > 2 \text{ GeV}$ ,  $i = 1, 2$  (middle) and with SOS orthogonality condition  $p_T(\mu_i) > 2 \text{ GeV}$ ,  $p_T(\mu_2) \leq 3.5 \text{ GeV}$  or  $\Delta R \leq 0.3$  (right).

To understand the shaping and hierarchy formation due to the  $p_T$  cut, the  $p_T$  of the muons is plotted vs.  $\Delta R(\ell\ell)$  in Figure 6.13. Requiring  $p_T(\mu_2) \geq 2 \text{ GeV}$  for  $\Delta m = 1.13 \text{ GeV}$  limits the range of  $\Delta R(\mu\mu)$  to less than 0.4, while leaving a large range exceeding 3 for the  $\Delta m = 5.63 \text{ GeV}$  model point. To gain access and sensitivity to the low  $\Delta m$  model points, allowing small  $\Delta R(\ell\ell)$  values, less than 0.3 is necessary, even before considering the reconstruction efficiency of the leptons. In the next sections, the study of reconstructed leptons and the isolation criteria will enable the retention of signal points with highly-columnated lepton pairs, as further explored in Section 6.6.7.

As seen in Section 6.4.4.2 for  $m_{\mu\mu}$ , reconstruction has an effect on both the shape and overall count of events. The effects on the  $\Delta R(\mu\mu)$  distributions are investigated in Figure 6.14.

Comparing Figure 6.14 and Figure 6.12, the main effect of the reconstruction on the  $\Delta R(\mu\mu)$  is the overall normalization, which is due to reconstruction efficiency.

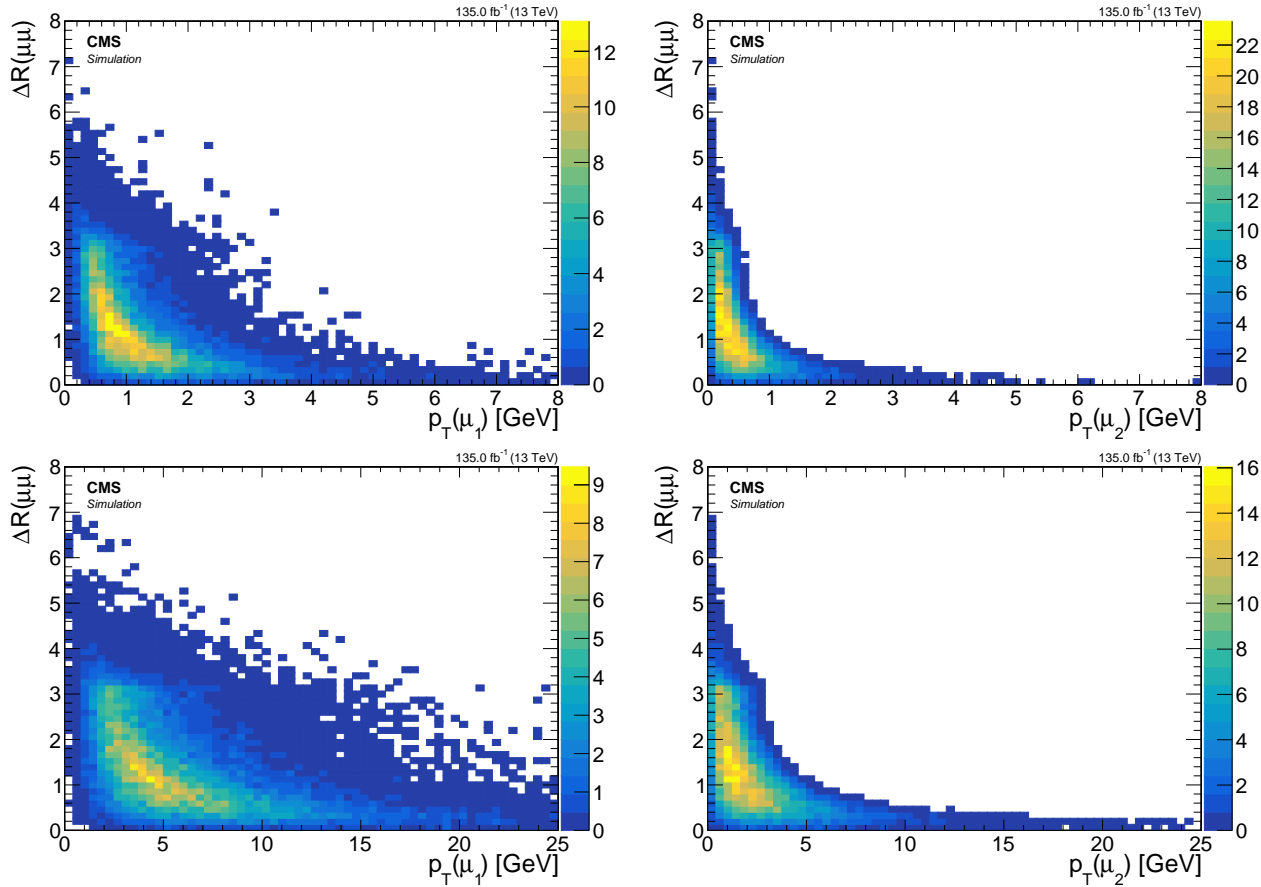


Figure 6.13: Event distributions in the plane of  $\Delta R(\mu\mu)$  vs.  $p_T$  for leading lepton  $\mu_1$  (left) and subleading lepton  $\mu_2$  (right) for signal models with  $\Delta m = 1.13 \text{ GeV}$  (top) and  $\Delta m = 5.63 \text{ GeV}$  (bottom).

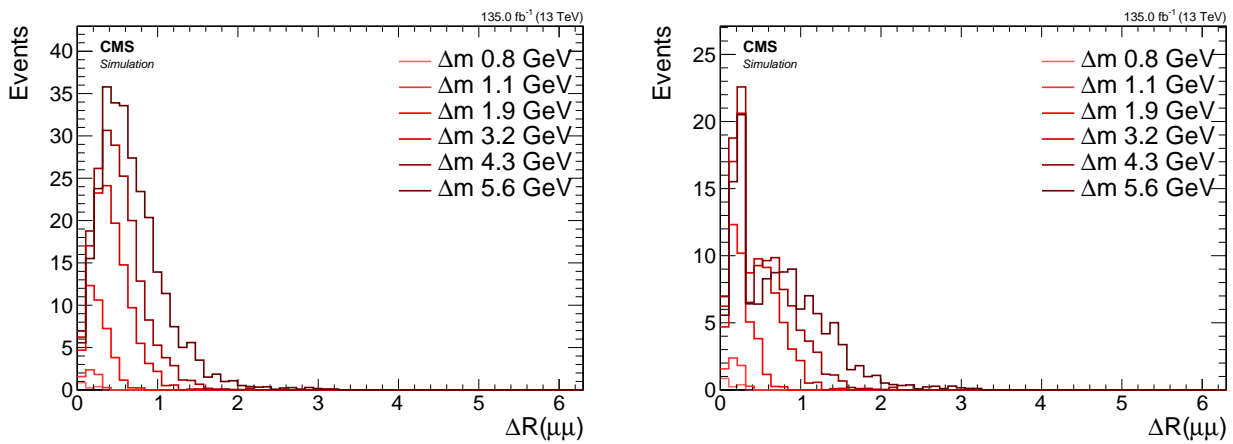


Figure 6.14: Distributions of the reconstructed  $\Delta R(\mu\mu)$  with preselection applied (left) and the additional SOS orthogonality condition (right).

### 6.4.5 Main drivers of sensitivity

The above studies reveal the main drivers of the sensitivity to different model points of this analysis, and may inform future analysis strategies that expand on the current work. This section has not explicitly included SM background in the plots, making it hard to conclude what effects changing the cuts to  $E_T^{\text{miss}}$  or other event level observables might have. However, it is very clear from examining the dilepton kinematics that for low  $\Delta m$  model points, regions with low  $p_T$  and  $\Delta R$  contain the bulk of the signal events. Another driver of the sensitivity at all  $\Delta m$  model points is the luminosity, since the production cross section drops as a function of the higgsino mass parameter  $\mu$ .

The next sections will explore how to lower the threshold on the muon transverse momentum and deal with collimated leptons that might pose a challenge in regards to the isolation criterion.

## 6.5 Simulated samples

### 6.5.1 Standard Model simulated samples

### 6.5.2 Signal simulated samples

## 6.6 Object definition and selection

In Section 5, the reconstruction and identification of objects in the detector were presented. Additionally, the signal signature was studied in Section 6.4. In this section, an object selection is devised to obtain a sample of objects that is as pure as possible with respect to the target leptons, while still retaining as much signal as possible. As discussed in Section 6.3, the focus is on selecting opposite-charged, same-flavor leptons  $\ell^+\ell^-$  resulting from the  $\tilde{\chi}_2^0$  that decays into a  $\tilde{\chi}_1^0$  via a  $Z^*$ , i.e.,  $\tilde{\chi}_2^0 \rightarrow \tilde{\chi}_1^0 \ell^+ \ell^-$ . Two choices of  $\Delta m^0$  are presented in the following section: a relatively high  $\Delta m^0$  of  $\Delta m^0 = 5.63\text{ GeV}$  and a low  $\Delta m^0$  of  $\Delta m^0 = 1.92\text{ GeV}$ , but not so low as to prevent enough electrons from surviving the initial reconstruction  $p_T$  threshold of 5 GeV. The higgsino parameter is fixed at  $\mu = 100\text{ GeV}$ .

In Section 6.4, the base selection required at least one jet in the event with  $p_T \geq 30\text{ GeV}$  and  $|\eta| < 2.4$ , without any other selections. However, unlike in that section, objects are not weighted to any luminosity in this section, as the focus is on the proportion between object types. Two types of leptons are differentiated: those originating from the targeted decay  $\tilde{\chi}_2^0 \rightarrow \tilde{\chi}_1^0 \ell^+ \ell^-$ , shown in blue, and those that do not, referred to as *other*, shown in yellow. Signal leptons are marked as such by matching a reconstructed lepton to a generator level lepton, which has been confirmed to have the  $\tilde{\chi}_2^0$  as its parent. Leptons marked as *other* may have been misreconstructed, misidentified, or may be a result of the hadronisation process in a jet (such as the ISR jet). The goal is to select as many blue leptons as possible while rejecting as many yellow ones as possible. In the following sections, the term *efficiency* refers to the proportion of signal leptons passing a selection, divided by the initial number of signal leptons, and the term *purity* refers to the proportion of signal leptons (blue) to the sum of the signal leptons and *other* leptons (yellow). In other words, the goal is to find a selection with high efficiency and high purity. However, these two quantities can sometimes compete with each other, requiring compromises.

### 6.6.1 Electrons

The electrons are subject to an initial reconstruction  $p_T$  threshold of 5 GeV, and are reconstructed using a loose working point, as described in Section 5. The first distribution of interest regarding the electrons is their spatial separation from the leading jet in the event, denoted as  $\Delta R(j_1, e)$ . The distributions can be seen in Figure 6.15.

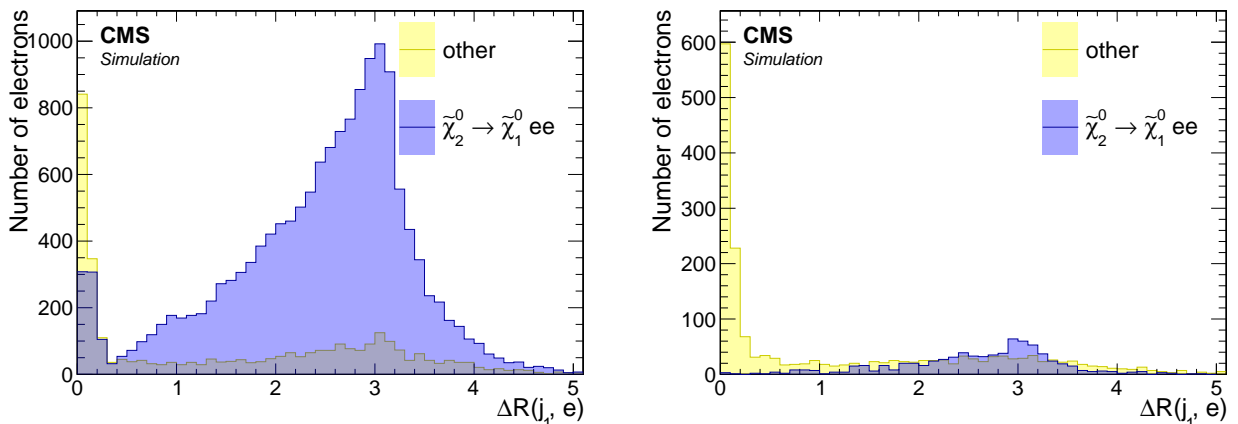


Figure 6.15: Spatial separation between reconstructed electrons with loose ID and the leading jet  $\Delta R(j_1, e)$  for  $\Delta m = 5.63\text{ GeV}$  (left) and  $\Delta m = 1.92\text{ GeV}$  (right).

The plots in Figure 6.15 reveal two key features. The first one has already been discussed in Section 6.4, which is that probing lower  $\Delta m$  necessitates access to low  $p_T$  leptons. Therefore,

the threshold of  $p_T \geq 5$  GeV on the electrons leads to reduced signal acceptance. This is evident from the difference between the high and low  $\Delta m$  cases. The second interesting feature is that the signal electrons are predominantly located outside the leading jet. This is because the leading jet is typically an ISR jet, which boosts the  $\tilde{\chi}_2^0 \tilde{\chi}_1^0$  system away from it, causing them to be back-to-back. Thus, a cut of  $\Delta R(j_1, e) > 0.4$  is made to account for this.

In this step, the  $p_T$  distributions of electrons are examined by applying the  $\Delta R(j_1, e) > 0.4$  cut. It is observed that the  $p_T$  distribution depends heavily on the  $\Delta m$ , which has been previously demonstrated for muons in Section 6.4.4.1. While the distributions in that section were plotted using generator level muons, the  $p_T$  distributions for electrons follow the same trend. Thus, a choice must be made regarding which  $\Delta m$  to prioritize, and the lower  $\Delta m$  case is chosen for increased sensitivity. However, the two choices are compared in Figure 6.16.

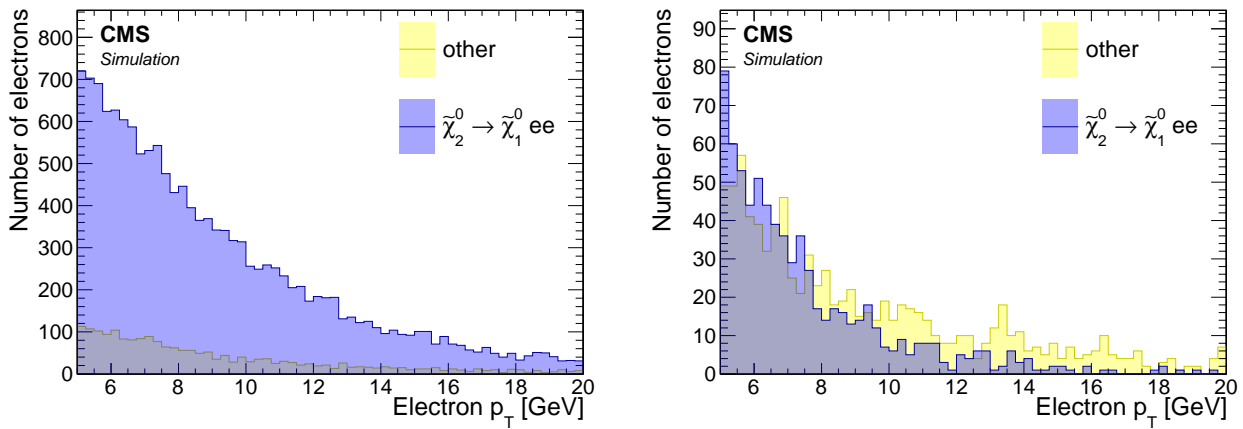


Figure 6.16:  $p_T$  distribution of reconstructed electrons with loose ID for  $\Delta m = 5.63$  GeV (left) and  $\Delta m = 1.92$  GeV (right). Cut of  $\Delta R(j_1, e) > 0.4$  applied.

As expected, the  $p_T$  distribution of the electrons falls more rapidly for the low  $\Delta m$  case. It is observed that there are hardly any electrons surviving above 15 GeV. Therefore, a cut of  $p_T < 15$  GeV is chosen.

The  $\eta$  distribution is interesting to look at, as seen in Figure 6.17, after the previous cuts to gain a better understanding of where most of the non-signal electrons originate from.

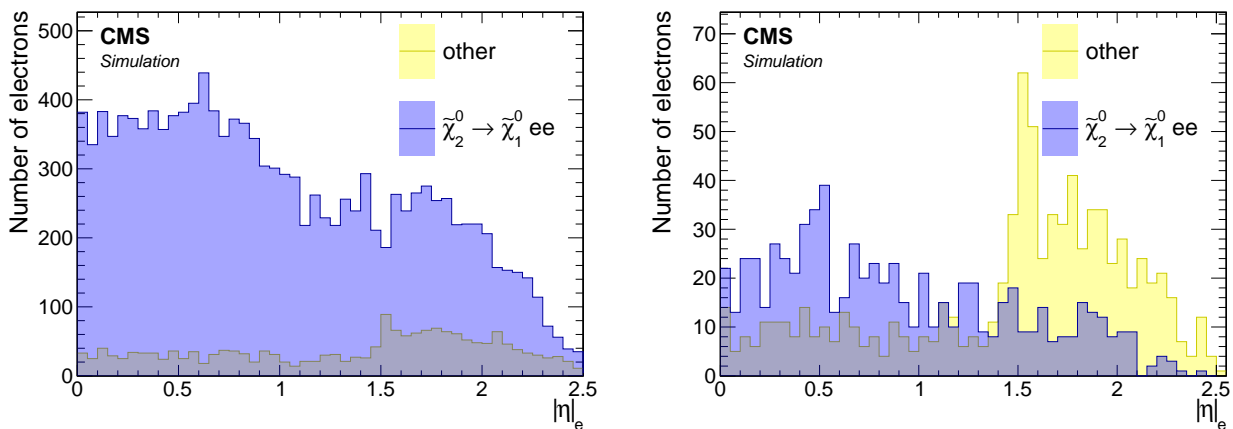


Figure 6.17:  $|\eta|$  distribution of reconstructed electrons with loose ID for  $\Delta m = 5.63$  GeV (left) and  $\Delta m = 1.92$  GeV (right). Cuts of  $\Delta R(j_1, e) > 0.4$  and  $p_T < 15$  GeV are applied.

For the  $\Delta m = 1.92$  GeV case, it can be clearly seen that the endcaps of the Electromagnetic Calorimeter (ECAL) are performing worse compared to the barrel ( $|\eta| < 1.48$ ). The transition

is easily noticeable through a sharp drop in purity at the transition. It is even worse for low- $p_T$  electrons than for higher- $p_T$  ones.

To determine whether a tighter working point for the electron-identification is beneficial, the effects of requiring either a medium or a tight working point are investigated. The working point previously used in the distributions is the loose working point. Two bins labeled *fail* and *pass* are plotted to correspond to whether the electron fails or passes the identification criteria of medium or tight working points. These bins are shown in Figure 6.18.

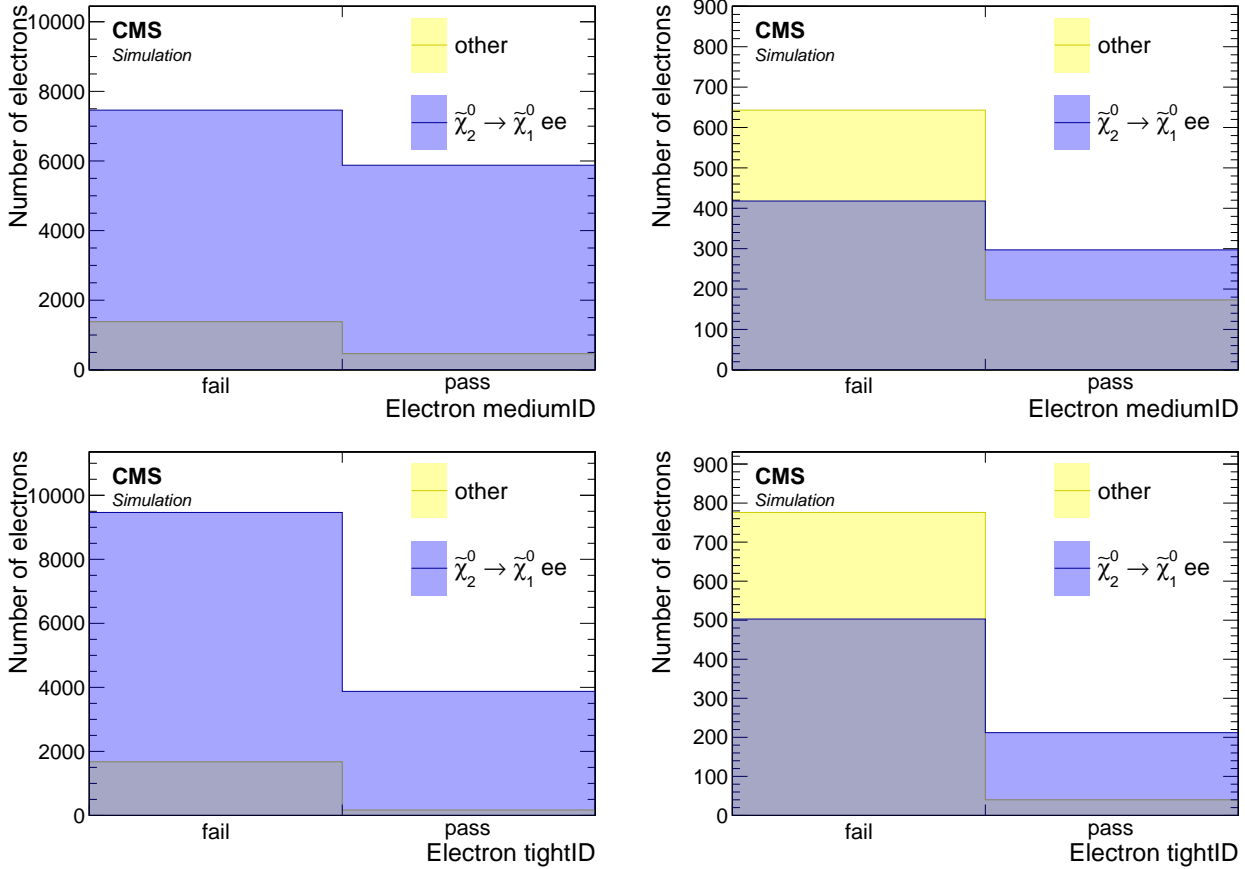


Figure 6.18: Medium (top) and tight (bottom) ID working points distributions of reconstructed electrons for  $\Delta m = 5.63 \text{ GeV}$  (left) and  $\Delta m = 1.92 \text{ GeV}$  (right). Cuts of  $\Delta R(j_1, e) > 0.4$  and  $p_T < 15 \text{ GeV}$  are applied.

Selecting a medium or a tight working point is equivalent to choosing the relevant right *pass* bin (top for medium, bottom for tight), and rejecting the electrons on the left *fail* bin. It can be seen that considerable amount of non-signal electrons are rejected in the low  $\Delta m$  case by picking either a medium or tight working points, but a significant number of signal electrons are also lost. Therefore, using these selections is not very efficient and results in low signal acceptance. A decision is made to use a loose working point for the electrons, and instead rely on isolation to achieve higher purity. The effect of isolation on the purity of the electrons is therefore also examined. The jet-isolation is discussed in detail in Section 6.6.7, but for the sake of completeness, its effect on the purity of the electrons is also shown here. The custom jet-isolation is compared with the standard definition of lepton isolation, which does not take into account the possibility that two electrons can be produced close to each other (small  $\Delta R$ ), as is the case in the signal. The isolation distributions are shown in Figure 6.19.

It is observed that the standard lepton isolation is not efficient for both  $\Delta m$  cases, while the custom jet-isolation performs well in terms of signal electron efficiency and successfully rejects a considerable amount of non-signal electrons. This results in a purer sample of electrons, and

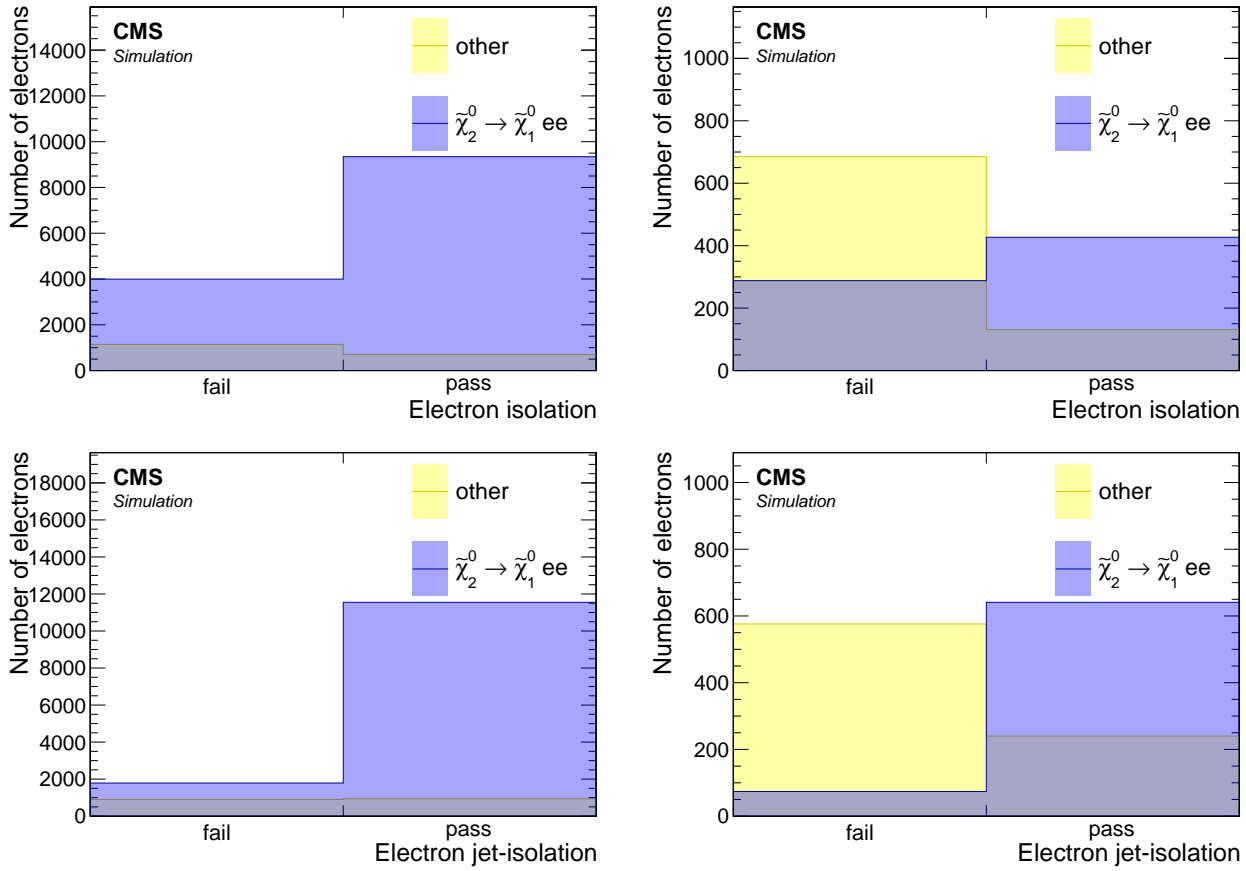


Figure 6.19: Standard isolation (top) and custom jet-isolation (bottom) distributions of reconstructed electrons with loose ID for  $\Delta m = 5.63$  GeV (left) and  $\Delta m = 1.92$  GeV (right). Cuts of  $\Delta R(j_1, e) > 0.4$  and  $p_T < 15$  GeV are applied.

thus the choice of custom jet-isolation is concluded to be favorable. The effect of this choice on the  $\eta$  distribution is also examined in Figure 6.20, concluding the selection of electrons.

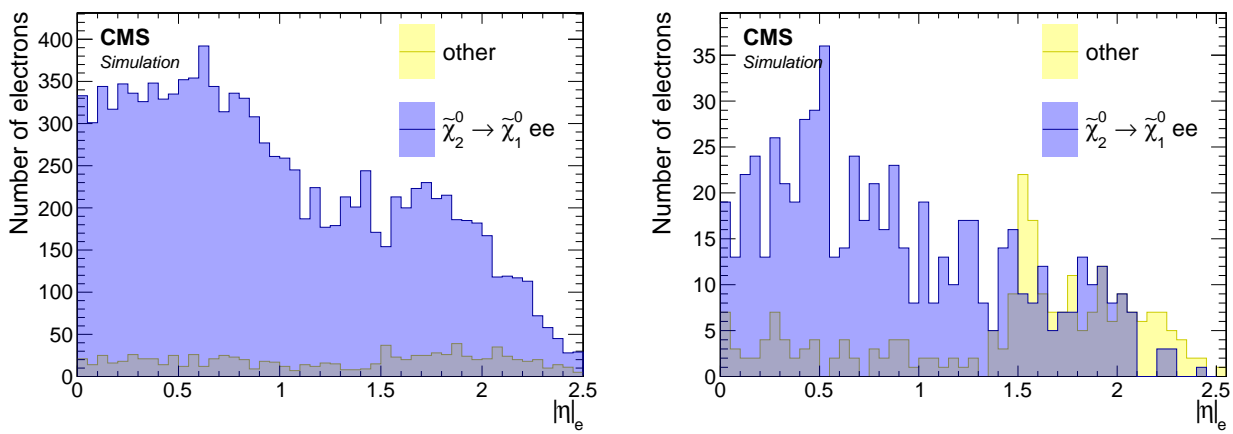


Figure 6.20:  $|\eta|$  distribution of reconstructed electrons with loose ID passing jet-isolation for  $\Delta m = 5.63$  GeV (left) and  $\Delta m = 1.92$  GeV (right). Cuts of  $\Delta R(j_1, e) > 0.4$  and  $p_T < 15$  GeV are applied.

Distributions in Figure 6.20 show that the custom jet-isolation has further purified the electron selection while retaining signal electrons, compared to distributions in Figure 6.17.

To summarize this section, the following is the full selection of the analysis electrons:

- $5 < p_T < 15 \text{ GeV}$
- $|\eta| < 2.5$
- $\Delta R(j_1, e) > 0.4$
- loose ID working point
- pass jet-isolation

## 6.6.2 Muons

In contrast to electrons, the initial reconstruction  $p_T$  threshold for muons is not set to 5 GeV. Hence, the possibility of lowering the  $p_T$  threshold as much as possible is explored. This was motivated in section 6.4.4.1 where it was observed that the lower the  $\Delta m$  to be probed, the lower the  $p_T$  threshold has to be. Similarly to the electrons case, the initial working point choice for reconstructed muons is loose (see 5). A similar procedure to the electron case is followed. The spatial separation of muons from the leading jet in the event,  $\Delta R(j_1, \mu)$ , is the first distribution examined. As shown in Figure 6.7, the muon endcaps are capable of reconstructing muons with  $p_T < 3$  GeV while the barrel cannot. Therefore, it makes sense to look at a split view of barrel and endcaps for the following distributions at 6.21.

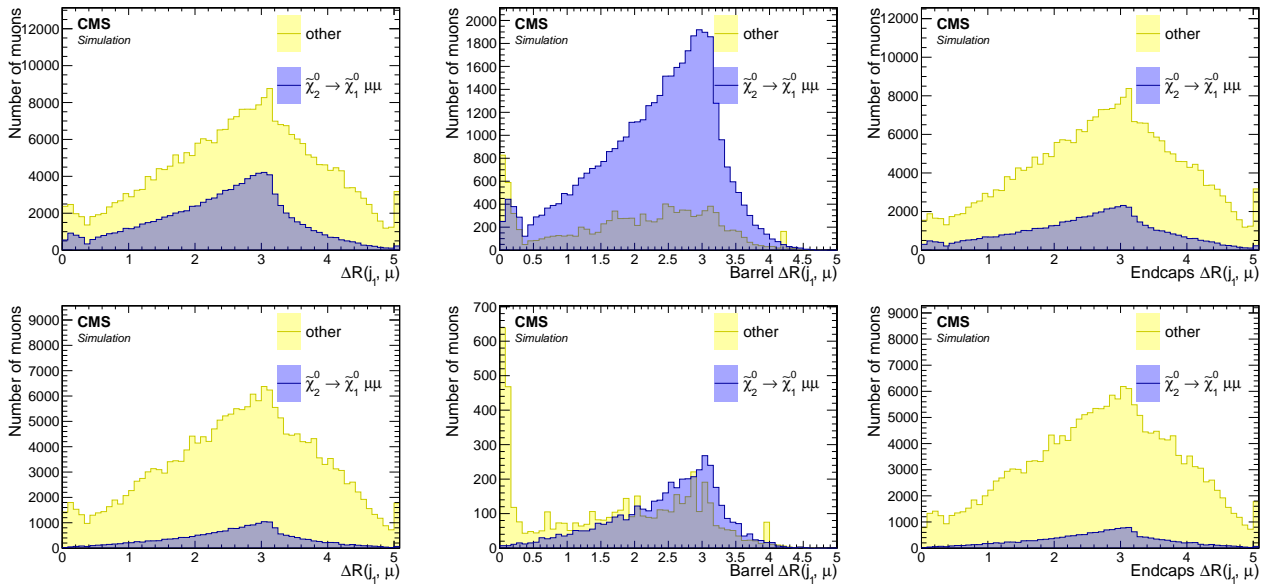


Figure 6.21: Spatial separation between reconstructed muons with loose ID and the leading jet  $\Delta R(j_1, \mu)$  for  $\Delta m = 5.63$  GeV (top) and  $\Delta m = 1.92$  GeV (bottom) in the inclusive case (left), barrel (middle) and endcaps (right).

Since the muons in the endcaps have lower  $p_T$  than the muons in the barrel, which is only able to reconstruct muons with  $p_T > 3$  GeV, the purity in the endcaps is much lower than the purity in the barrel. The selection being constructed here attempts to further purify the muons. Muons with  $\Delta R(j_1, \mu) > 0.4$  are selected like in the electrons case, and this selection will apply for the rest of the section.

Next, the  $p_T$  distributions are examined. The previous cut of  $\Delta R(j_1, \mu) > 0.4$  is applied. As seen in Section 6.4.4.1, the  $p_T$  distribution depends strongly on  $\Delta m$ , and the low  $\Delta m$  acceptance is favored to be more sensitive to it. The  $p_T$  distributions seen in Figure 6.22 suggest a cut identical to the electron case of  $p_T < 15$  GeV. It is worth mentioning that the  $p_T$  of the muons are fed into the training of the Boosted Decision Tree (BDT) for further refinement, and therefore the exact value is being determined here quite loosely. The actual maximum value of the  $p_T$  of the muons will depend on the BDT cut being used to define the signal region.

The feature discussed earlier, whereby the endcaps are capable of reconstructing muons with lower  $p_T$  and therefore have worse purity than the barrel, is reiterated here. It is important to stress that the worse purity is due to a much higher efficiency, and as long as the muons can be purified further, it is not necessarily a bad thing. The bulk of the non-signal muons populate the region of  $p_T < 2$  GeV, and the ratio of signal muons to non-signal muons is very low in that region. An additional cut of  $p_T > 2$  GeV is therefore made. Another way of looking at the effect of this cut is by examining the  $|\eta|$  distribution before and after the  $p_T$  cut, which can be

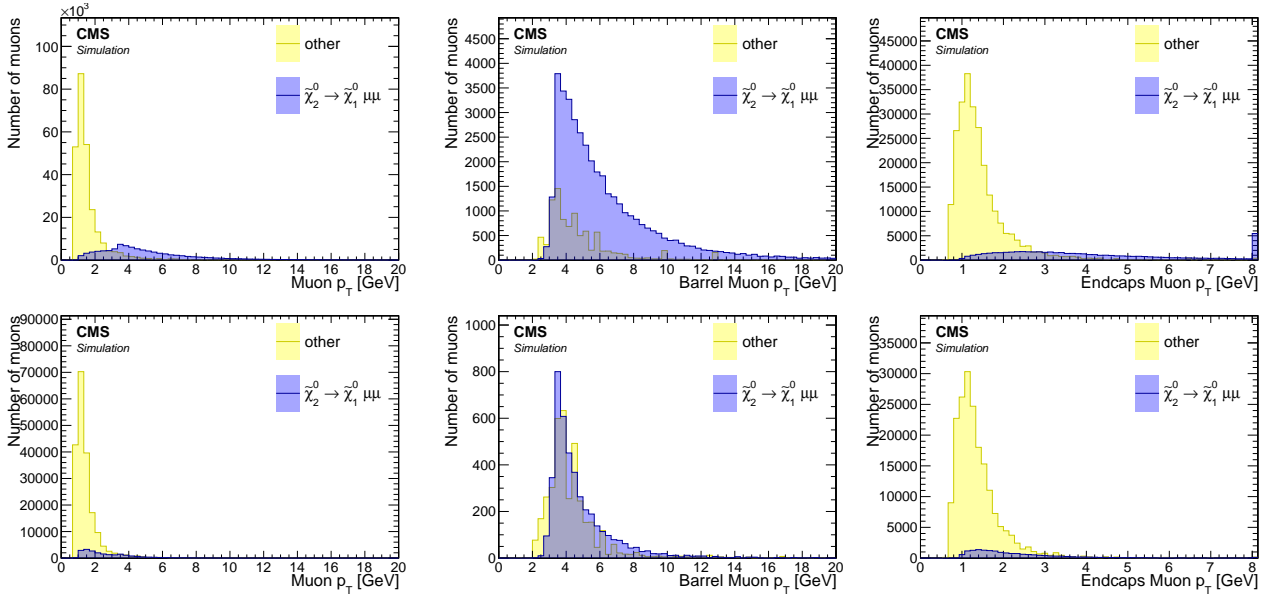


Figure 6.22: Reconstructed muons  $p_T$  distribution with loose ID for  $\Delta m = 5.63 \text{ GeV}$  (top) and  $\Delta m = 1.92 \text{ GeV}$  (bottom) in the inclusive case (left), barrel (middle) and endcaps (right). Cuts of  $\Delta R(j_1, \mu) > 0.4$  and  $p_T < 15 \text{ GeV}$  are applied.

seen in Figure 6.23.

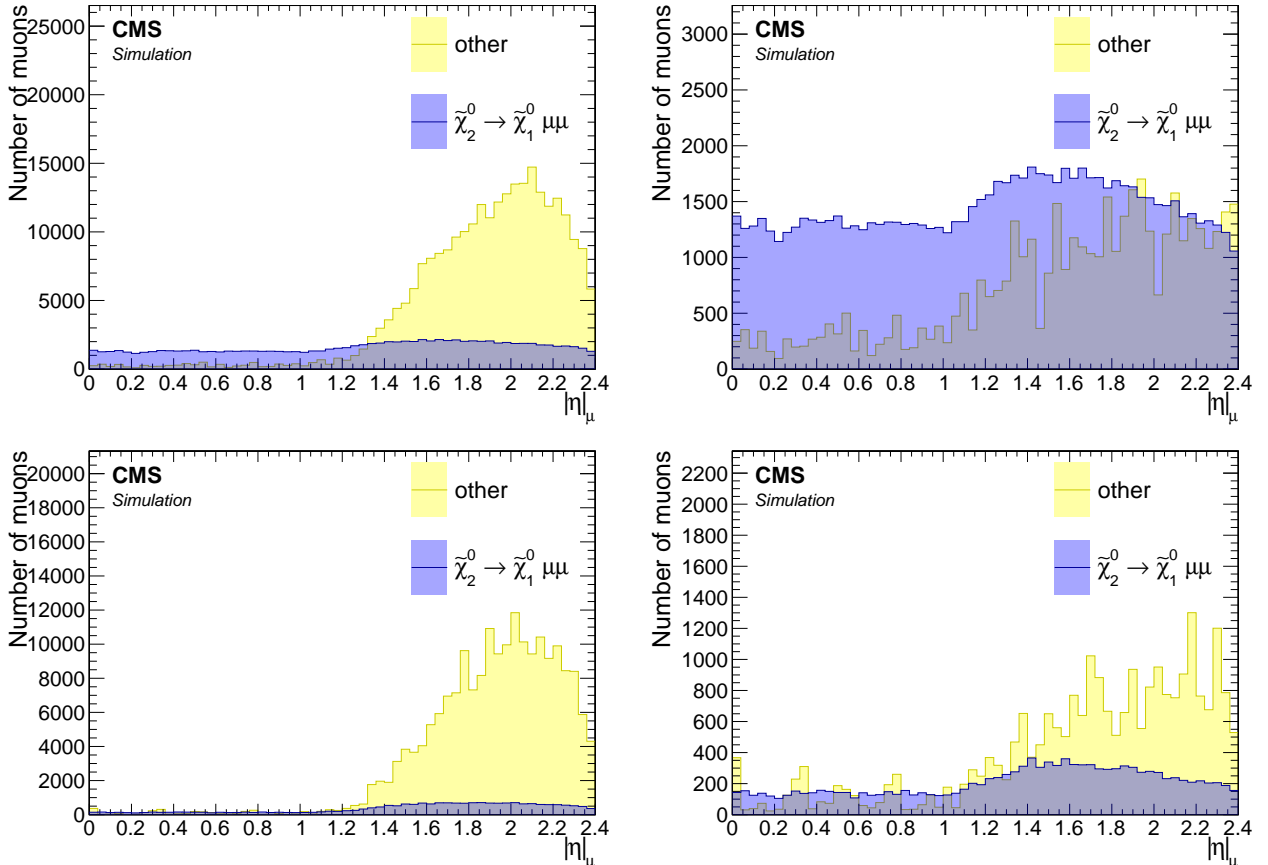


Figure 6.23:  $|\eta|$  distribution of reconstructed muons with loose ID for  $\Delta m = 5.63 \text{ GeV}$  (top) and  $\Delta m = 1.92 \text{ GeV}$  (bottom) without (left) and with (right)  $p_T > 2 \text{ GeV}$  cut. Cut of  $\Delta R(j_1, \mu) > 0.4$  is also applied.

To see if requiring a tighter working point for the muon-identification is beneficial, it is

necessary to test the effects of requiring either a medium working point, or a tight one. Two bins labeled *fail* and *pass* are plotted, which correspond to whether the muon passes or fails the identification criteria of a medium or tight working points.

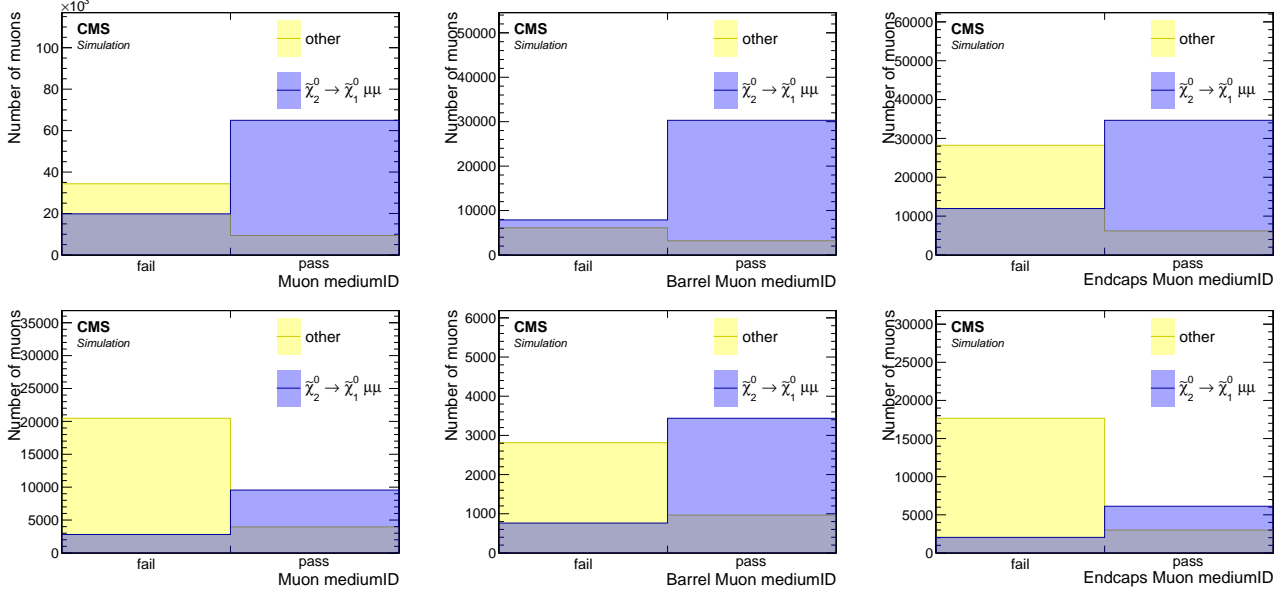


Figure 6.24: Medium ID working point distributions of reconstructed muons for  $\Delta m = 5.63 \text{ GeV}$  (top) and  $\Delta m = 1.92 \text{ GeV}$  (bottom) in the inclusive  $p_T$  case (left), barrel (middle) and endcaps (right). Cuts of  $\Delta R(j_1, \mu) > 0.4$ ,  $p_T > 2 \text{ GeV}$  and  $p_T < 15 \text{ GeV}$  are applied.

Comparing the medium working point in Figure 6.24 to the tight working point in Figure 6.25, it is apparent that the medium working point is very beneficial in purifying the muons. However, when the tight working point is used, a significant number of wanted signal-muons are lost without a significant gain in purity. Therefore, the medium ID working point is chosen.

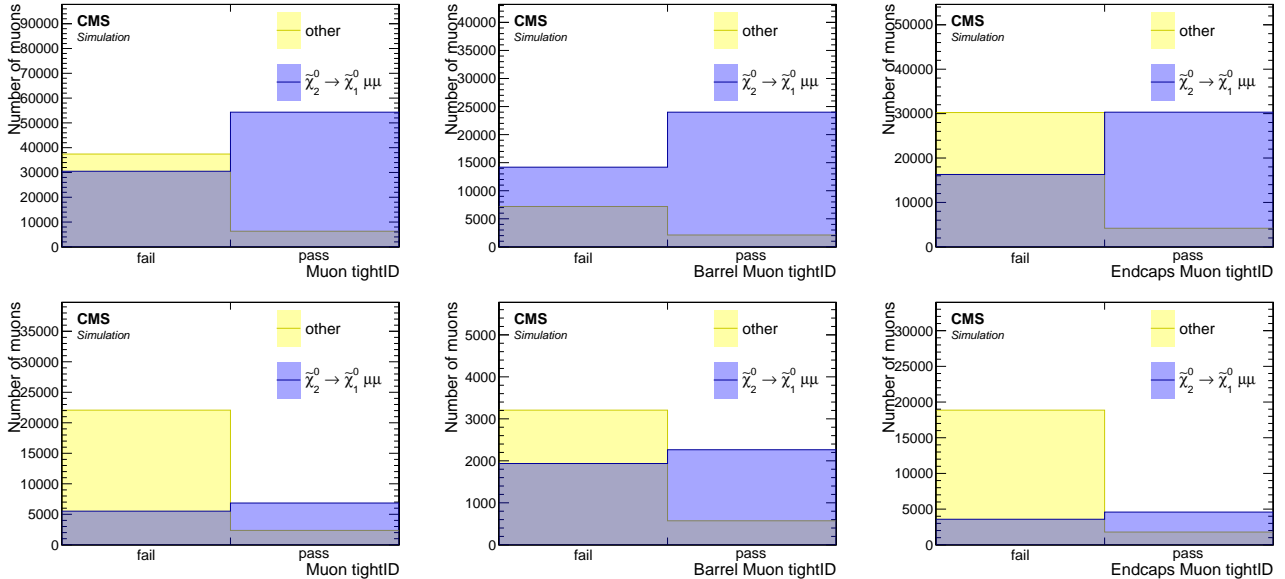


Figure 6.25: Tight ID working point distributions of reconstructed muons for  $\Delta m = 5.63 \text{ GeV}$  (top) and  $\Delta m = 1.92 \text{ GeV}$  (bottom) in the inclusive  $p_T$  case (left), barrel (middle) and endcaps (right). Cuts of  $\Delta R(j_1, \mu) > 0.4$ ,  $p_T > 2 \text{ GeV}$  and  $p_T < 15 \text{ GeV}$  are applied.

The custom jet-isolation was designed to reject SM background while retaining signal, as described in Section 6.6.7. For electrons, as shown in Figure 6.19, it effectively purified the

selection and eliminated the need for a tighter identification working point. As for muons, although a medium working point is relied upon to perform this task, the effects of the isolation on signal muons are still of interest. Figure 6.26 shows that a small price is paid by requiring the isolation. However, as will be seen in Section 6.6.7, the sensitivity is increased by rejecting a lot of SM background in the process.

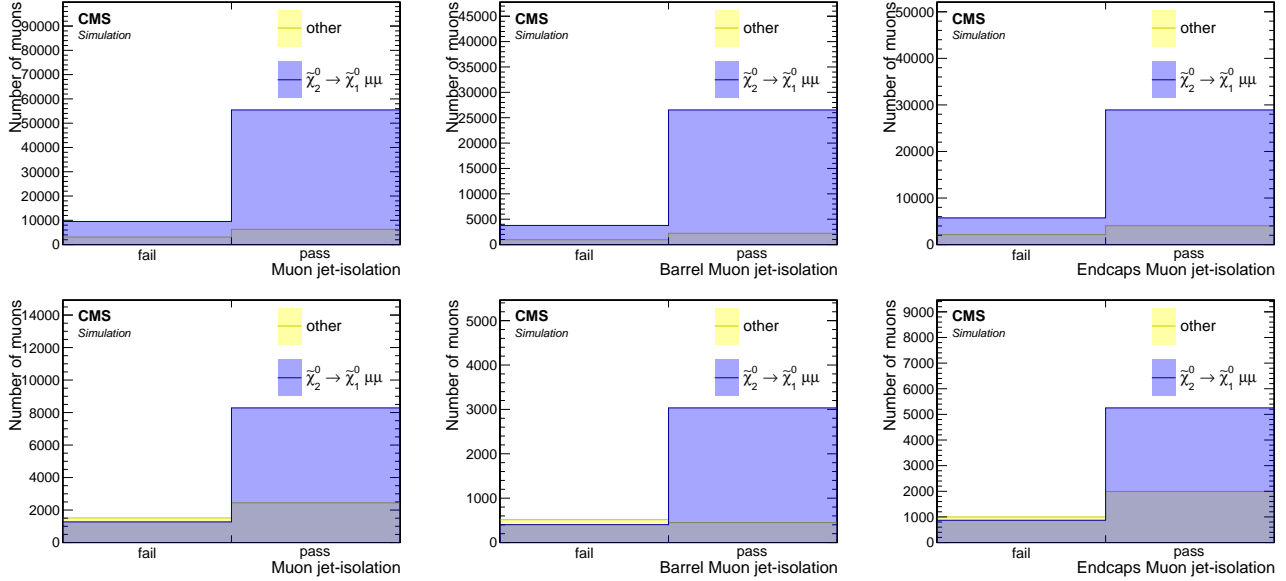


Figure 6.26: Jet-isolation distributions of reconstructed muons with medium ID for  $\Delta m = 5.63 \text{ GeV}$  (top) and  $\Delta m = 1.92 \text{ GeV}$  (bottom) in the inclusive  $p_T$  case (left), barrel (middle) and endcaps (right). Cuts of  $\Delta R(j_1, \mu) > 0.4$ ,  $p_T > 2 \text{ GeV}$  and  $p_T < 15 \text{ GeV}$  are applied.

To summarize this section, the following is the full selection of the analysis muons:

- $2 < p_T < 15 \text{ GeV}$
- $|\eta| < 2.4$
- $\Delta R(j_1, \mu) > 0.4$
- medium ID working point
- pass jet-isolation

### 6.6.3 Scale factors

In Section 6.6.1 and Section 6.6.2, the selection applied to electrons and muons respectively was studied, and a choice was made regarding the identification working point. Simulation was exclusively used to draw conclusions about the identification efficiency of the leptons. However, relying solely on Monte Carlo (MC) simulation can produce significant systematic errors due to imperfections in modeling both the data and the detector response. Therefore, measuring the identification efficiency in data is necessary to correct any potentially false efficiency rates in the simulation. The term *efficiency* refers to the probability of reconstructing or identifying a lepton. For a lepton  $\ell$ , the identification efficiency is defined as:

$$\varepsilon_{\ell}^{\text{ID}} = \frac{N_{\ell}(\text{ID})}{N_{\ell}(\text{produced})} \quad (6.1)$$

In MC simulation, the number of produced leptons is the same as the number of generated leptons. However, in data, the efficiency must be measured using a data-driven method. Once the efficiencies have been measured both in simulation and data, a correction factor called the Scale Factor (SF) can be applied to the simulation to correct any discrepancies that may arise. Scale factors are defined as the ratio between the efficiency in data and the efficiency in simulation:

$$\text{SF}_{\ell}^{\text{ID}} = \frac{\varepsilon_{\ell}^{\text{ID,Data}}}{\varepsilon_{\ell}^{\text{ID,MC}}}, \quad (6.2)$$

dropping the superscript ID, this becomes:

$$\text{SF}_{\ell} = \frac{\varepsilon_{\ell}^{\text{Data}}}{\varepsilon_{\ell}^{\text{MC}}}. \quad (6.3)$$

Once the relevant SF have been determined, they are applied to every lepton that passes the object selection in the event. The scale factors for loose-ID electrons in the relevant  $p_{\text{T}}$  range have been centrally measured by the corresponding working group and are applied to the selected electrons. As determined in Section 6.6.2, the analysis signal muon's lower  $p_{\text{T}}$  threshold is 2 GeV, which is low. Scale factors for medium ID leptons with  $p_{\text{T}} \geq 2 \text{ GeV}$  were computed centrally by the Muon Physics Object Group (POG). However, the scale factors were computed by requiring  $\Delta R > 0.5$  between the muons, as mentioned in [2, 3], and while they match the muons'  $p_{\text{T}}$  range and identification working point,  $\Delta R < 0.5$  is one of the drivers of sensitivity, as seen in Section 6.4.4.3. Therefore, it is necessary to validate the scale factors in that region and show that the efficiencies have no  $\Delta R$  dependence. To do so, the efficiencies in different  $\Delta R$  regions are calculated.

In order to measure such efficiencies in data, one must identify desired leptons with low and easily reducible fakes. A widely used method to perform such a data-driven task is the Tag & Probe method. This involves examining a mass resonance such as Z, J/ $\psi$  or Y to select particles of the desired type, and probing the efficiency of a particular selection criterion on those particles. The mass resonance then decays into two same-flavor opposite charged pairs of leptons, forming a peak on top of a background. To measure the efficiency of low  $p_{\text{T}}$  muons, dimuon events around the J/ $\psi$  mass window are chosen. One muon is labeled as a ‘tag’ and the other as a ‘probe’. The tag muon is selected with a very tight selection resulting in high certainty that the object corresponds to a real produced muon. The probe is given a loose selection but constrained to be consistent with a product of a J/ $\psi$ , almost certainly originating from a real muon as well. The background is easily removed by fitting the shape of the J/ $\psi$ . The probe is then subjected to cuts or constraints, used to measure a particular efficiency. This

study aims to show that the efficiency to identify a muon with a medium ID working point from a track has no  $\Delta R$  dependence. Therefore, the efficiency in question is defined as:

$$\varepsilon_\mu^{\text{ID}} = \frac{N_\mu^{\text{ID}}}{N_t}. \quad (6.4)$$

The denominator probe used in the study refers to a track that has passed a loose selection, while the numerator probe track is required to match a medium ID working point muon. To determine the number of objects passing a selection, a fit is performed on data and MC samples to measure the corresponding efficiencies.

This study was conducted for the year 2016. The 2016 samples listed in Section 6.5.1 are used for MC. To ensure the independence of the tagged muon from the triggered object, a single electron trigger is used for data. The corresponding data set is measured to be  $36.02 \text{ fb}^{-1}$  using the BRIL Work Suite [4]. The following trigger paths are utilized:

- `HLT_Ele27_WPTight_Gsf_v*`,
- `HLT_Ele27_eta2p1_WP Loose_Gsf_v*`,
- `HLT_Ele32_WPTight_Gsf_v*`,
- `HLT_Ele35_WPTight_Gsf_v*`.

An offline loose ID electron with  $p_T > 27 \text{ GeV}$  is then selected. The requirements to select a tag & probe pair are defined in Table 6.6.3.

Table 6.3: Selection criteria for Tags and Probes

Tag	Probe
medium ID muon	isolated track
$p_T \geq 5 \text{ GeV}$	$2 \leq p_T \leq 20 \text{ GeV}$ ( $p_T \geq 3 \text{ GeV}$ for barrel)
$ \eta  < 2.4$	opposite-sign in invariant mass window $[2.5, 3.5] \text{ GeV}$

A fit is then performed in an invariant mass window around the  $J/\psi$  peak of  $[2.5, 3.5] \text{ GeV}$ . The signal fit uses a crystal ball function, and the continuum is fit with a 6th order polynomial. The fit is repeated twice, where the denominator is based on probe tracks, and the numerator uses medium ID muons that have been matched to those tracks. The  $\Delta R$  range has been split into three, and the  $|\eta|$  of the muons has been divided into barrel ( $|\eta| < 1.2$ ) and endcaps ( $1.2 < |\eta| < 2.4$ ). Simulation fits are shown in Figure 6.27 for the barrel, and Figure 6.28 for the endcaps. Data fits are shown in Figure 6.29 for the barrel, and in Figure 6.30 for the endcaps.

The efficiencies and corresponding scale factors can be seen in Figure 6.31. The scale factors are statistically consistent with unity and show no discernible  $\Delta R$  dependence. A similar study was carried out with simulation and data for 2017 and 2018 in [5], and no  $\Delta R$  dependence was observed either. As a result of these studies, the recommendation from the POG is to use the calculated scale factors provided by them with an additional systematic uncertainty of 1% for muons with  $p_T < 20 \text{ GeV}$ .

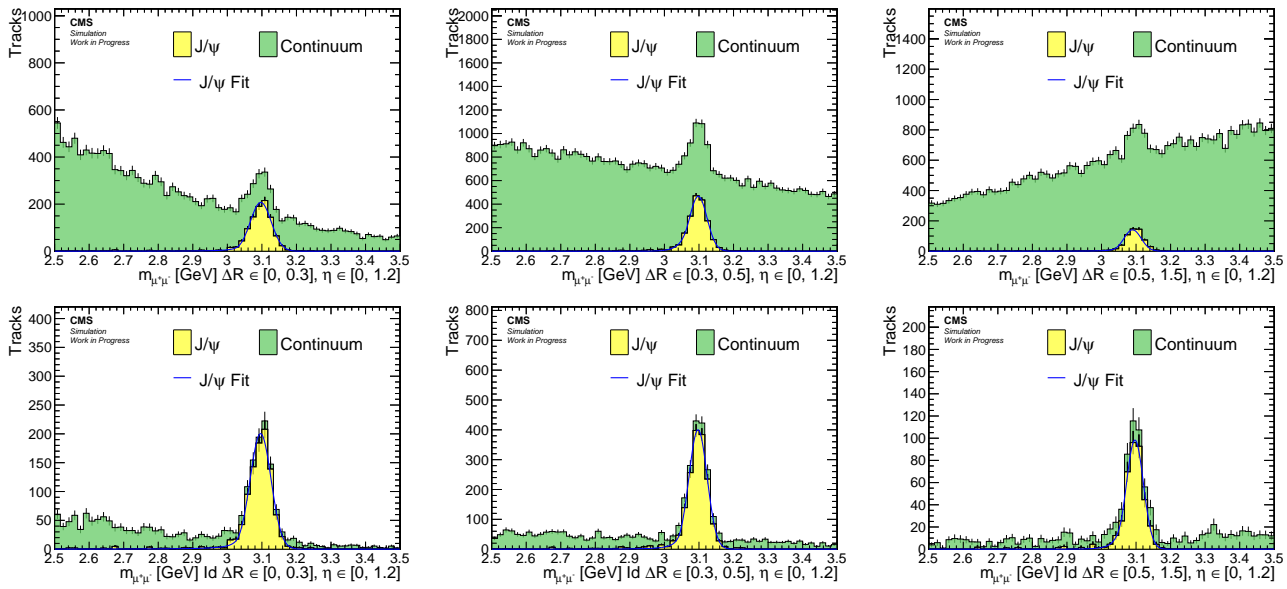


Figure 6.27: Simulation barrel muons fits for denominator (top) and numerator (bottom) for  $0 < \Delta R < 0.3$  (left),  $0.3 < \Delta R < 0.5$  (center),  $0.5 < \Delta R < 1.5$  (right)

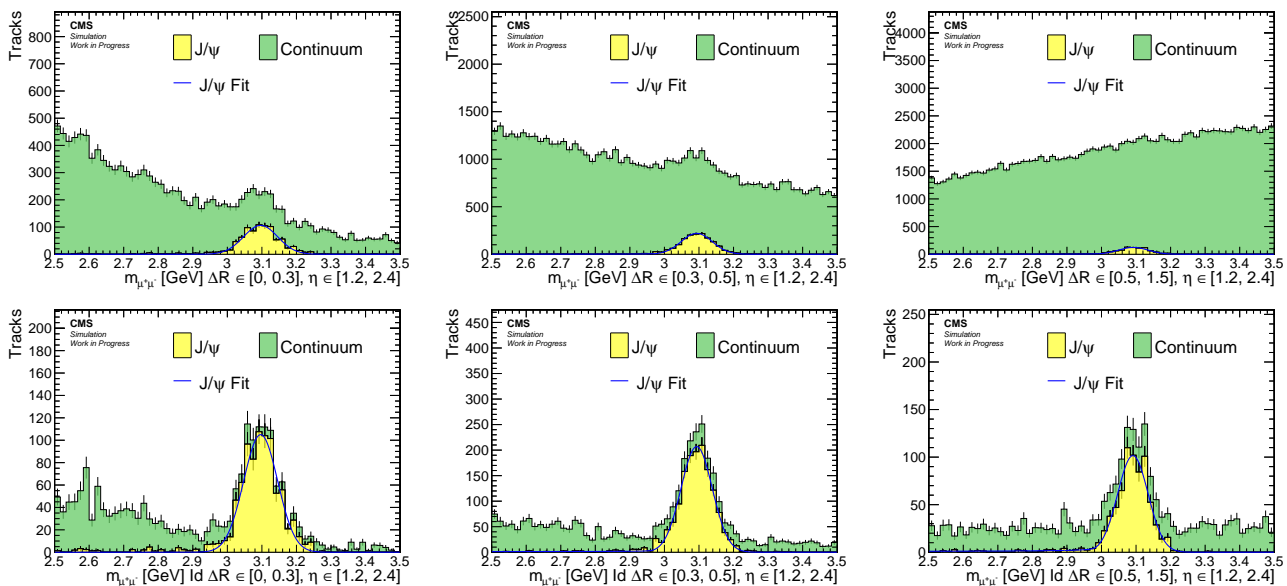


Figure 6.28: Simulation endcaps muons fits for denominator (top) and numerator (bottom) for  $0 < \Delta R < 0.3$  (left),  $0.3 < \Delta R < 0.5$  (center),  $0.5 < \Delta R < 1.5$  (right)

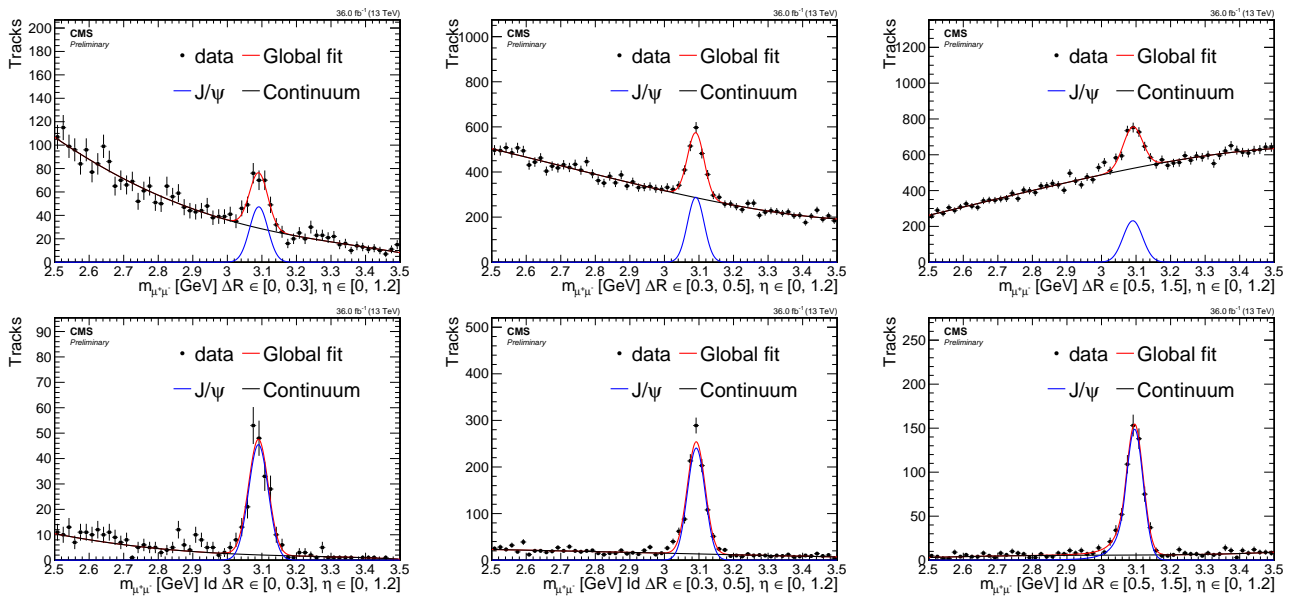


Figure 6.29: Data barrel muons fits for denominator (top) and numerator (bottom) for  $0 < \Delta R < 0.3$  (left),  $0.3 < \Delta R < 0.5$  (center),  $0.5 < \Delta R < 1.5$  (right)

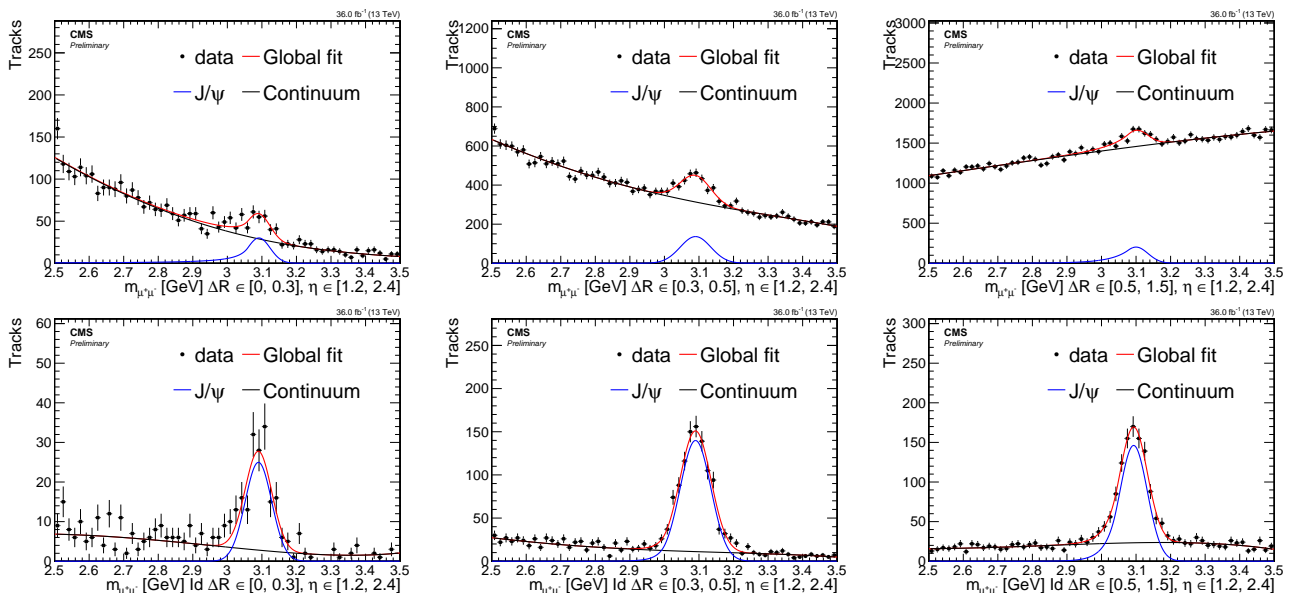


Figure 6.30: Data endcaps muons fits for denominator (top) and numerator (bottom) for  $0 < \Delta R < 0.3$  (left),  $0.3 < \Delta R < 0.5$  (center),  $0.5 < \Delta R < 1.5$  (right)

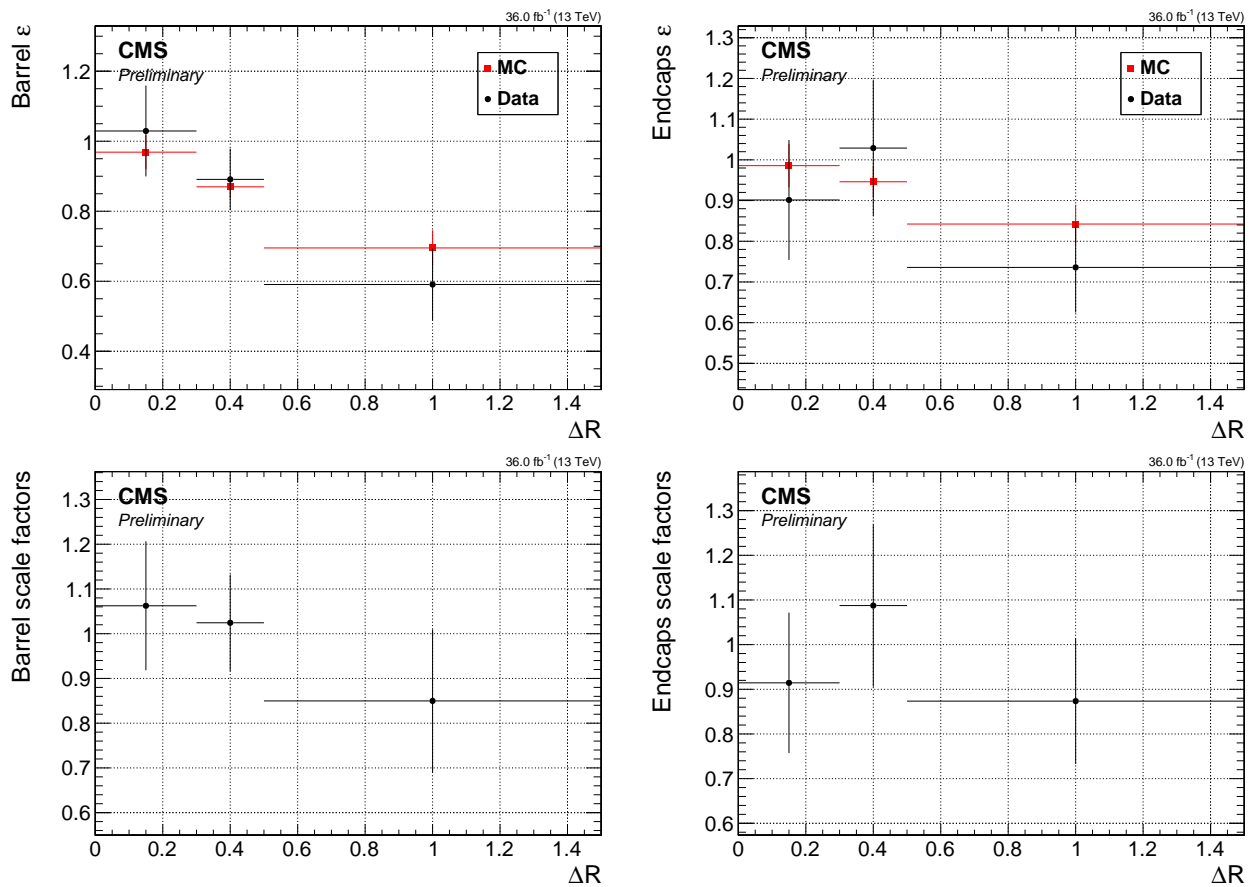


Figure 6.31: Efficiencies (top) and scale factors (bottom) for barrel muons (left) and endcaps muons (right).

### 6.6.4 Missing transverse energy

The importance of measuring the missing transverse momentum (or energy) in this analysis has been discussed in Section 6.4.1. It has been concluded that the missing transverse momentum is an essential ingredient in the analysis strategy. It is used to trigger events online and in the offline event level selection to boost sensitivity. Two standard measures of the momentum imbalance in the events are  $\vec{E}_T^{\text{miss}}$  (or  $\vec{p}_T^{\text{miss}}$  by a different symbol) and  $\vec{H}_T^{\text{miss}}$ . Although  $\vec{E}_T^{\text{miss}}$  and  $\vec{p}_T^{\text{miss}}$  have different symbols and are referred to by different names (missing transverse energy and missing transverse momentum respectively), they are defined in the same way and used interchangeably. Mathematically,  $\vec{E}_T^{\text{miss}}$  is defined as follows:

$$\vec{E}_T^{\text{miss}} = \vec{p}_T^{\text{miss}} = - \sum_i \vec{p}_T(i) \quad (6.5)$$

where the summation is done on all particle flow candidates. Therefore, the missing transverse energy serves as a measure of particles that evade detection, such as weakly interacting particles. Mismeasurements of visible particles and additional energy deposits from sources such as Pile-Up (PU), jet energy response and detector noise can affect this observable, so it undergoes further correction to mitigate these effects. The correction process considers jets with  $p_T$  greater than 10 GeV. Full details of the corrections can be found in [6].

An alternative measurement to the missing transverse momentum is  $\vec{H}_T^{\text{miss}}$ , which is sometimes referred to as *missing hardronic activity*. Instead of considering all particle flow candidates in the sum, this measurement only takes into account jets with  $p_T$  greater than 30 GeV and  $|\eta| < 5$ :

$$\vec{H}_T^{\text{miss}} = - \sum_i^{\text{jets}} \vec{p}_T(i) \quad (6.6)$$

The observable  $\vec{H}_T^{\text{miss}}$  is favored over  $\vec{E}_T^{\text{miss}}$  in this analysis, since the jet isolation, defined in Section 6.6.7, uses jets with  $p_T$  greater than 30 GeV, while a sideband is defined using the range of  $p_T \in [15, 30]$  GeV of jets, which is then used for the data-driven background estimation method in Section 6.9.2.1. Both observables,  $\vec{E}_T^{\text{miss}}$  and  $\vec{H}_T^{\text{miss}}$ , have equivalent scalar quantities,  $E_T^{\text{miss}}$  and  $H_T^{\text{miss}}$  respectively, which can be obtained by taking the magnitude of their vectorial counterpart.

### 6.6.5 Jets

The reconstruction and identification of jets are described in Section 5.4. Jets used in the analysis are reconstructed by clustering the Particle Flow (PF) candidates using FASTJET and the anti- $k_T$  algorithm [7] with a size parameter of 0.4. Tagging of  $b$  quark jets is performed using the multivariate technique DEEPCSV with a medium working point, also known as the Combined Secondary Vertex (CSV) algorithm. Jets are required to have a transverse momentum  $p_T > 30$  GeV and  $|\eta| < 2.4$ .

### 6.6.6 Tracks and multivariate selection

The leptons  $\ell^+\ell^-$  produced in the decay  $\tilde{\chi}_2^0 \rightarrow \tilde{\chi}_1^0\ell^+\ell^-$  tend to have mostly very low transverse momentum  $p_T$ . It has been shown in Section 5 that the identification and reconstruction of the muons worsen with lower  $p_T$ . Therefore, the aim of the exclusive track category is to attempt and recover lost leptons that were not reconstructed or identified. As seen in Section 5.1, the tracking efficiency at the  $p_T$  ranges used in this analysis is well above 99%, allowing the recovery of some of the tracks that correspond to the missing leptons by applying knowledge about the event kinematics specific to the signal. Thus, the exclusive track category does not enhance the lepton identification in the general case, but recovers missed tracks in this specific signal signature.

To identify which track corresponds to the miss-identified lepton in a given signal event, a Boosted Decision Tree (BDT) is trained. Four separate BDTs are trained, corresponding to the lepton flavor (muon or electron) and the phase of the tracker (phase 0 for 2016, and phase 1 for 2017-2018). All BDTs use a common structure of 200 trees with a maximum depth of 3, and are trained with AdaBoost and GiniIndex separation using the TMVA package [8]. Default values are used for all other parameters.

Tracks from the privately produced FASTSIM signal simulations listed in Section 6.5.2 are used for training. The full range of simulated higgsino parameter  $\mu$  (or the mass of  $\tilde{\chi}_1^\pm$  in the case of phase 1) is considered, but only the range of  $\Delta m$  that this analysis targets. For phase 0,  $\Delta m^0$  is chosen from the range  $[0.3, 4.3]$  GeV and  $\mu$  from  $[100 - 130]$  GeV, while for phase 1,  $\Delta m^\pm$  is chosen from  $[0.3 - 4.6]$  GeV and  $\mu$  from  $[100 - 500]$  GeV. Signal events are split into signal tracks and background tracks, with signal tracks originating from the decay  $\tilde{\chi}_2^0 \rightarrow \tilde{\chi}_1^0\ell^+\ell^-$  and matching the missing generated lepton in the generator level particles collection, while background tracks do not match the wanted leptons. Therefore, the BDTs are useful for rejecting in-signal background of unwanted tracks. The samples for muons contain 9408 (10964) signal tracks and 99996 (151380) background tracks for phase 0 (phase 1). For electrons the samples contain 2364 (2288) signal tracks and 104065 (159713) background tracks for phase 0 (phase 1). The training samples are then tested against test samples of equal size. The distributions of the testing samples that overlay on the training samples can be seen in Figure 6.33.

A pre-selection is applied to all tracks in the collection obtained by the standard track reconstruction sequences. This pre-selection ensures that only properly-reconstructed, isolated, and prompt tracks are considered. The selected tracks must also have trajectories passing through the region near the primary vertex with the largest sum of charged-tracks, jets, and missing energy values (PV):

- $p_T > 1.9$  GeV
- $|\eta| < 2.4$
- track iso<sub>rel</sub> < 0.1, using  $\Delta R(\text{track}, \text{other tracks}) < 0.3$
- $d_{xy}(\text{track}, \text{PV}) < 0.02$  cm w.r.t the PV
- $d_z(\text{track}, \text{PV}) < 0.02$  cm w.r.t the PV
- no match to an electron or muon within a cone of size 0.01

For the training, a set of 10 variables listed in decreasing order of their ranking (in the muon case of phase 0) is used, as shown in Table 6.6.6.

Figure 6.32 shows the distribution of input variables, where signal tracks are shown in blue and background tracks in red.

Table 6.4: Track BDT input variables

Rank	Variable	Description
1	$\Delta R(t, \ell)$	$t$ is the track and $\ell$ the lepton
2	$ \Delta\eta(t, \ell) $	
3	$p_T(\ell)$	
4	$ \Delta\phi(t, \vec{H}_T^{\text{miss}}) $	
5	$ \Delta\eta(t, j_1) $	$j_1$ is the leading jet
6	$ \Delta\phi(t, \ell) $	
7	$ \eta(t) $	
8	$ \eta(\ell) $	
9	$\Delta R(\ell, j_1)$	
10	$m_{t\ell}$	invariant mass

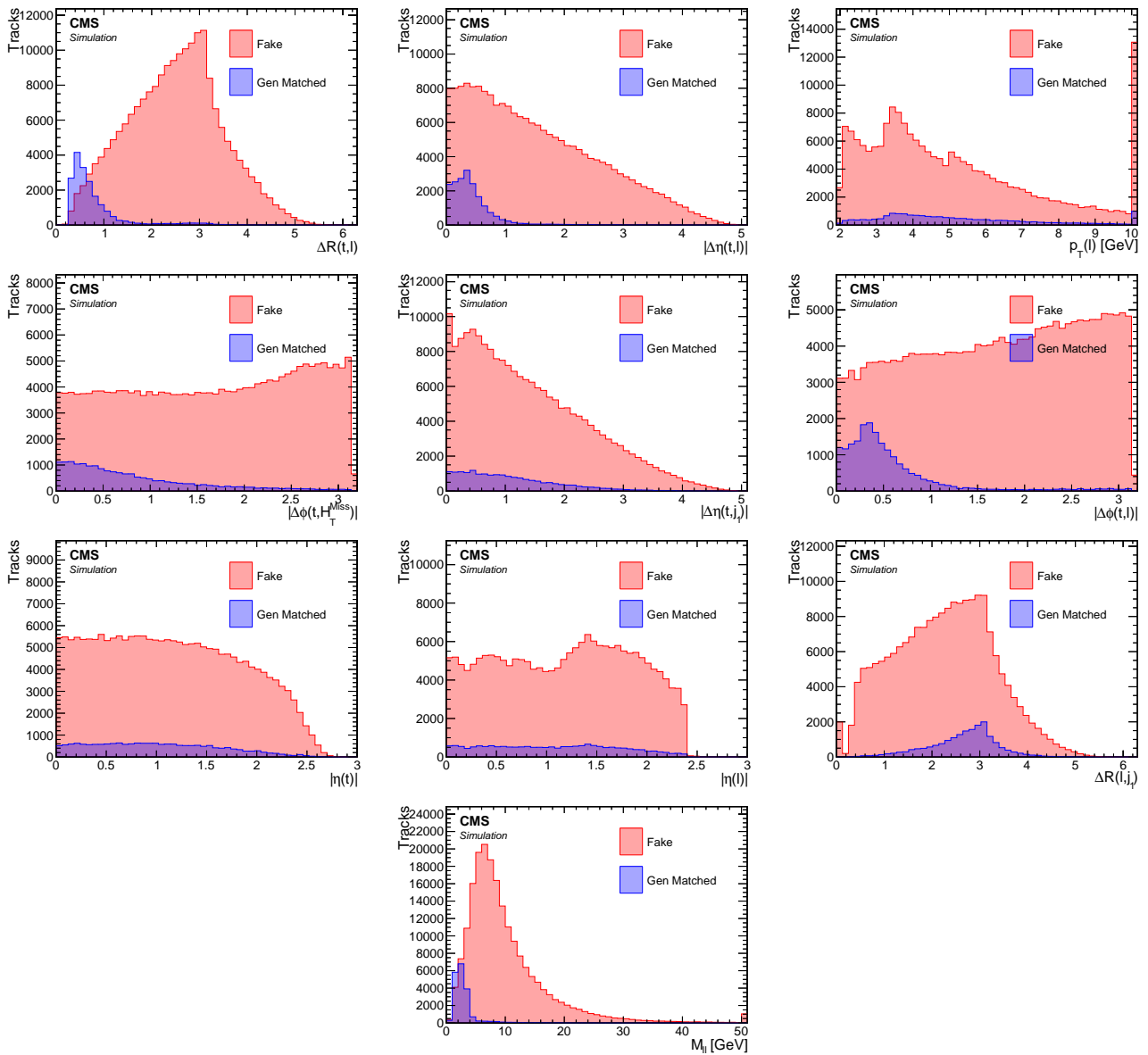


Figure 6.32: Distributions of the inputs for training for the track BDT in the Muon exclusive track category.

The output of the training for the 4 BDTs is displayed in Figure 6.33, where the testing distributions are superimposed on the training sample of the BDT. No obvious over-training

is observed. The ROC curves are then plotted in Figure 6.34, and the red point shows the efficiency of the signal and background tracks of the BDT cut, which is selected to be 0.0. A good separation between signal tracks and fake tracks is obtained, as evidenced by the relatively high signal efficiency of over 90% (86%) for muons (electrons) and background rejection of around 86% (76%) for muons (electrons).

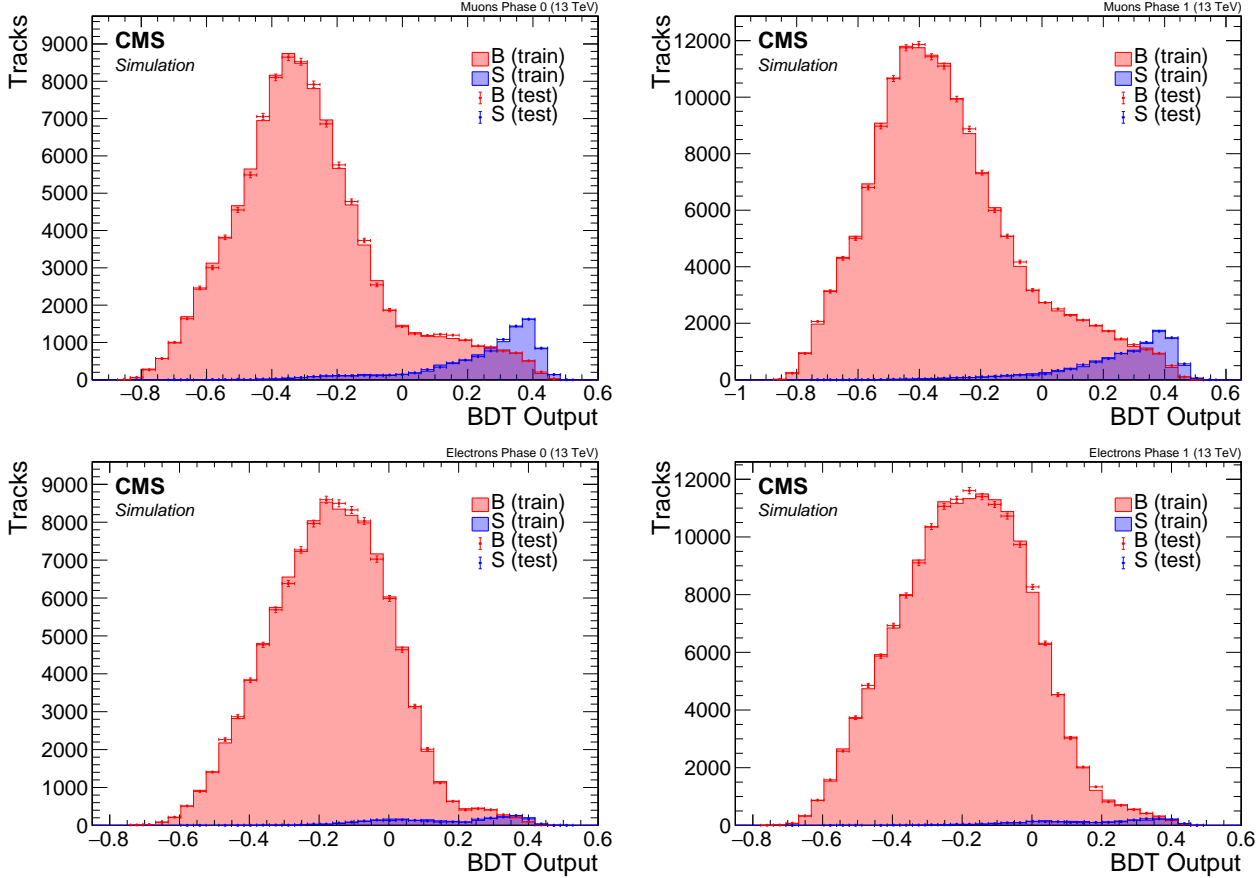


Figure 6.33: Track BDT output plots for Muons (top) and Electrons (bottom) in phase 0 (left) and phase 1 (right). Blue shows signal tracks, while Red are fake tracks. Test sample overlay on top of training sample.

After the training process, the track with the maximum BDT score is selected as the missing lepton in the event. Only events with a track with a score greater than 0.0, corresponding to the red dot in the ROC curves shown in Figure 6.34, are considered.

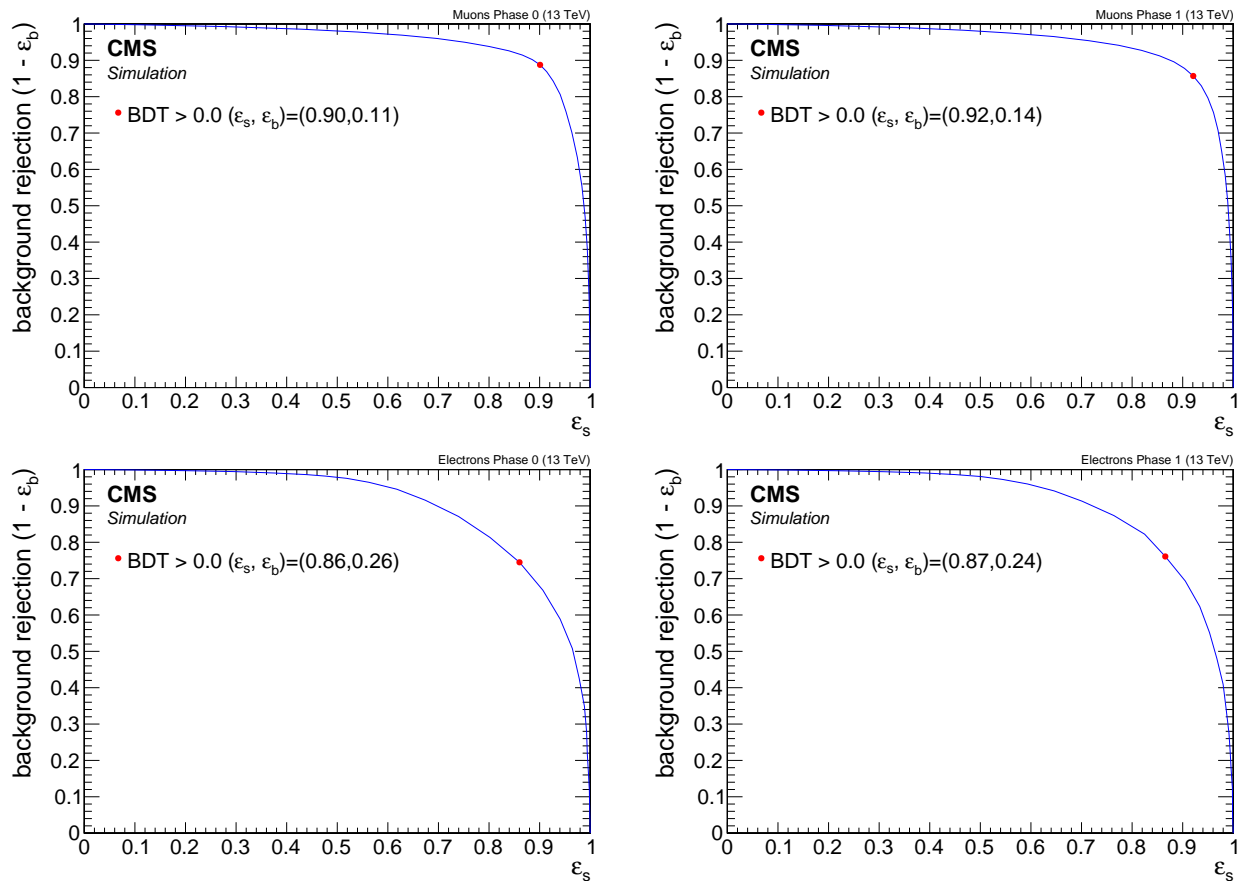


Figure 6.34: Track BDT ROC curves for Muons (top) and Electrons (bottom) in phase 0 (left) and phase 1 (right). Minimum working point showed as a red dot.

### 6.6.7 Isolation

The leptons produced from the neutralino decay  $\tilde{\chi}_2^0 \rightarrow \tilde{\chi}_1^0 \ell^+ \ell^-$  are typically clean and isolated, with very little hadronic activity around them. This is because the only jets in the event come from initial state radiation, which provides a boost to the produced electroweakinos in the opposite direction. Therefore, the leptons originating from those electroweakinos will not exist in proximity to these jets. This signature can be exploited to discriminate between signal and background originating from standard model processes in association with jets. At CMS, various standard isolation criteria were developed and used. The three most widely used isolation criteria are track isolation [9], relative isolation (RelIso), which was first described in [10], and a modified version referred to as relative mini-isolation (miniRelIso), described in [11].

Track isolation is defined as the  $p_T$  sum of all tracks around a given track (or lepton) in a fixed cone size of 0.3:

$$\text{Track Isolation}_\ell = \frac{\sum_{\substack{\text{tracks from PV} \\ \text{in } \Delta R < 0.3}} p_T}{p_T(\ell)} \quad (6.7)$$

Since only tracks are summed, only charged particles are taken into account. Another widely used isolation is the relative isolation which uses a cone size of 0.4 and defined as:

$$\text{RelIso}_\ell = \frac{\sum_{\substack{\text{charged} \\ \text{hadrons} \\ \text{from PV}}} p_T + \max \left( 0, \sum_{\substack{\text{neutral} \\ \text{hadrons}}} E_T + \sum_{\text{photons}} E_T - 0.5 \cdot \sum_{\substack{\text{charged} \\ \text{hadrons} \\ \text{from PU}}} p_T \right)}{p_T(\ell)} \quad (6.8)$$

The last term in the definition is a correction for PU effects. A lepton is considered to have passed isolation if its RelIso value is small. The third commonly used isolation criterion is the mini-relative isolation (miniRelIso), which is a modified version of relative isolation. In mini-isolation, the cone size is dependent on the  $p_T$  of the lepton, as follows:

$$R = \begin{cases} 0.2 & p_T(\ell) \leq 50 \text{ GeV} \\ \frac{10 \text{ GeV}}{p_T(\ell)} & p_T(\ell) \in (50 \text{ GeV}, 200 \text{ GeV}) \\ 0.05 & p_T(\ell) \geq 200 \text{ GeV} \end{cases} \quad (6.9)$$

The variable size cone allows for the recovery of efficiency when leptons are produced in the decay chain of a boosted object. In such cases, when the boost is large, the lepton is likely to overlap with a jet produced in the same decay chain, failing a standard isolation cut.

The drawback of standard isolation criteria is that if two leptons are in proximity to each other, as is often the case in the signal, they compromise each other's isolation. As shown in Section 6.4.4.3, access to low  $\Delta m$  model-points requires including the  $\Delta R < 0.3$  phase-space region. Requiring any of the standard isolation criteria will thus result in rejecting valuable signal events. An alternative isolation criterion is proposed to help retain some of the desired phase-space while rejecting the majority of the standard model background. Another crucial use for an alternative isolation criterion is background estimation, as described in Section 6.9.2.1. The steps to construct the alternative *jet isolation* are described below. It is defined for each lepton flavor individually, since the produced leptons are of the same flavor. The steps are as follows (introducing parameters  $p$  and  $r$ ):

1. Create a copy set of the jets collection

2. Create a *lepton-corrected* set of the jets by subtracting all leptons within the jet cone of 0.4
3. Clean the set of jets by keeping only jets with positive energy and  $p_T$  greater than threshold  $p$
4. Lepton is said to pass *jet-isolation* if it does not lie within a cone of size  $r$  from a *lepton-corrected* jet
5. Lepton is said to fail *jet-isolation* for background estimation if it fails *jet-isolation*, and the original jet closest to it has  $15 < p_T < 30 \text{ GeV}$  (see 6.9.2.1 for use of such lepton)

The main idea behind defining jet-isolation is to reject leptons with hadronic activity around them while not losing a lepton that is close to another lepton of the same flavor. The process described introduces two free parameters: the  $p_T$  threshold of the lepton-corrected jets that cause a lepton's isolation to fail ( $p$ ), and the cone size ( $r$ ), which determines how close a corrected jet is allowed to be to a lepton. To choose the thresholds for these parameters, a scan has been performed ranging  $p \in [0, 20] \text{ GeV}$  and  $r \in [0.4, 0.6]$ . The scan is used to compare different criteria for the optimal values. Since the isolation is also used for background estimation, some of the criteria of interest stem from that method. The criteria of interest include signal efficiency (which should be high), background efficiency (which should be low), signal contamination in control-regions (ideally low), jetty-background transfer factor (ideally less than 1), and lastly, the significance, which is computed taking into account transfer factor error on the background (which should be maximized). To demonstrate the effect that this parameter space has on these criteria, a scan was done for the muons using 2016 MC and data.

Table 6.5: Signal Efficiency

		$\Delta R$				
		0.4	0.45	0.5	0.55	0.6
$p_T$	0	0.38	0.37	0.36	0.35	0.35
	1	0.39	0.38	0.37	0.37	0.36
	5	0.65	0.64	0.63	0.62	0.60
	6	0.71	0.70	0.69	0.67	0.66
	7	0.77	0.76	0.74	0.73	0.72
	8	0.82	0.82	0.80	0.78	0.77
	9	0.87	0.86	0.85	0.84	0.82
	10	0.89	0.89	0.87	0.86	0.85
	10.5	0.90	0.90	0.89	0.88	0.87
	11	0.92	0.92	0.91	0.90	0.89
	11.5	0.93	0.92	0.91	0.91	0.90
	12	0.94	0.93	0.92	0.91	0.90
	12.5	0.94	0.94	0.93	0.92	0.91
	13	0.95	0.95	0.94	0.93	0.93
	15	0.98	0.98	0.97	0.97	0.97
	20	1.00	1.00	1.00	0.99	0.99

From the scan, it is evident that the transfer factor of the jetty background estimation method increases with larger  $p_T$  but decreases with larger  $\Delta R$ . A transfer factor that is less than unity is preferred, and therefore, choices that do not meet this criteria are excluded. After taking into account all factors, the vaules  $(p, r) = (10 \text{ GeV}, 0.6)$  are selected for muons and  $(p, r) = (10 \text{ GeV}, 0.5)$  for electrons.

Table 6.6: Background Efficiency

	$\Delta R$				
	0.4	0.45	0.5	0.55	0.6
$p_T$	0	0.08	0.07	0.06	0.06
	1	0.08	0.07	0.06	0.06
	5	0.12	0.12	0.10	0.09
	6	0.15	0.14	0.12	0.11
	7	0.18	0.16	0.15	0.14
	8	0.20	0.18	0.17	0.17
	9	0.25	0.23	0.19	0.18
	10	0.26	0.25	0.22	0.19
	10.5	0.27	0.24	0.23	0.20
	11	0.29	0.26	0.24	0.22
	11.5	0.28	0.27	0.24	0.23
	12	0.29	0.27	0.26	0.24
	12.5	0.31	0.28	0.26	0.26
	13	0.33	0.29	0.27	0.27
	15	0.36	0.33	0.30	0.29
	20	0.45	0.41	0.39	0.36

Table 6.7: Transfer Factor

	$\Delta R$				
	0.4	0.45	0.5	0.55	0.6
$p_T$	0	0.19	0.16	0.13	0.13
	1	0.18	0.16	0.14	0.13
	5	0.31	0.30	0.26	0.23
	6	0.43	0.36	0.32	0.30
	7	0.55	0.48	0.44	0.40
	8	0.68	0.58	0.52	0.52
	9	0.83	0.78	0.65	0.58
	10	0.99	0.93	0.76	0.67
	10.5	1.07	0.95	0.85	0.74
	11	1.19	1.10	0.93	0.85
	11.5	1.24	1.19	0.96	0.91
	12	1.34	1.29	1.09	0.99
	12.5	1.55	1.35	1.21	1.10
	13	1.70	1.46	1.27	1.23
	15	2.39	2.17	1.80	1.63
	20	6.12	5.86	4.82	4.13

Table 6.8: Significance  $s/\sqrt{b + \epsilon_b^2}$ 

	$p_T$	$\Delta R$				
		0.4	0.45	0.5	0.55	0.6
	0	4.29	6.08	6.13	5.89	5.46
	1	4.92	5.18	6.34	5.33	5.84
	5	6.44	5.27	6.20	8.63	5.98
	6	4.72	5.06	6.22	6.99	7.92
	7	4.83	6.55	5.09	5.63	6.28
	8	3.80	5.48	4.60	5.24	4.61
	9	3.60	4.43	5.66	6.25	4.60
	10	3.37	4.08	5.57	4.78	6.23
	10.5	3.72	4.03	4.90	4.48	4.17
	11	3.05	3.51	4.37	4.98	5.41
	11.5	3.21	3.21	3.84	3.54	4.65
	12	3.48	3.51	3.80	3.30	3.54
	12.5	2.79	3.19	2.82	3.36	4.60
	13	3.16	2.68	3.59	6.60	3.50
	15	4.46	3.19	3.06	3.64	3.85
	20	7.21	1.46	1.60	8.10	2.09

## 6.7 Trigger

## 6.8 Event selection

In the upcoming section, the event-level selection applied in this analysis will be described. As discussed in Section 6.3, three categories are used in this analysis: the dimuon category and exclusive track categories for each lepton flavor. The preselection is summarized in Section 6.8.1, followed by the selection that defines each category in section 6.8.2. Finally, the multivariate selection for each category is discussed in Section 6.8.3.

### 6.8.1 Baseline selection

In Section 6.4.3, the base selection criteria that apply to all categories were reviewed. This section reiterates the reasons for these selections as well as describes other event-level selections.

- $H_T^{\text{miss}} \geq 220 \text{ GeV}$  and  $E_T^{\text{miss}} \geq 140 \text{ GeV}$  cuts are intended to boost sensitivity by rejecting SM background and to operate in the acceptance regime of the MET trigger, as described in Section 6.7. These cuts are especially efficient in rejecting QCD background, which does not produce real  $E_T^{\text{miss}}$ . Any  $E_T^{\text{miss}}$  apparent in QCD is due to jet energy miss-measurements. The harder cut on  $H_T^{\text{miss}}$  is made instead of  $E_T^{\text{miss}}$  because  $H_T^{\text{miss}}$  sums jets with  $p_T > 30 \text{ GeV}$  and is blind to objects with  $p_T < 30 \text{ GeV}$ . Since background estimation relies on jets with  $p_T$  in the range of  $[15, 30] \text{ GeV}$ ,  $H_T^{\text{miss}}$  is more appropriate than  $E_T^{\text{miss}}$  and does not introduce bias in the data-driven background estimation methods. The two observables describe are highly correlated and describe similar physics.
- $N_{\text{jets}} (p_T \geq 30 \text{ GeV} \text{ and } |\eta| < 2.4) \geq 1$ . At least one jet is required in the event because such an ISR jet gives a boost to the produced neutralino, thus increasing the missing transverse energy and the sensitivity of the analysis.
- $N_{b-\text{jets}} (p_T \geq 30 \text{ GeV} \text{ and } |\eta| < 2.4) = 0$ . Any event with b-tagged jet is vetoed since our signal does not contain real b-tagged jets. This veto is efficient in rejecting background from  $t\bar{t}$ , in which the b quarks arise from a t quark decay.
- $\min \Delta\phi (\vec{H}_T^{\text{miss}}, \vec{j}) > 0.4$ . Requiring an ISR jet in the event leads to the expectation that the  $H_T^{\text{miss}}$  should point in the opposite direction of the jet or at an angle close to  $\pi$ . Events with multiple jets in the SM background, such as those arising from QCD, will not exhibit such a feature. Therefore, this cut reduces the QCD background.
- veto events with isolated loose-ID lepton having  $p_T \geq 30 \text{ GeV}$ . Lepton can be either muon or electron. The signal does not have high- $p_T$  leptons, as has been seen in Section 6.4.
- $0.4 < m_{\ell\ell} < 12 \text{ GeV}$ . The signal resides in an invariant mass window with an edge at the mass difference between  $\tilde{\chi}_2^0$  and  $\tilde{\chi}_1^0$ . This is a relatively loose cut that is expected to be further tightened by the boosted decision tree.

The object level selection has already been described in Section 6.6. For the sake of completeness it is reiterated. The electrons in the analysis require are required to pass the following selection (also described in Section 6.6.1):

- $5 \leq p_T \leq 15 \text{ GeV}$
- $|\eta| < 2.5$
- pass jet isolation

- loose ID

The muons in the analysis are required to pass the following selection (see also Section 6.6.2):

- $2 \leq p_T \leq 15 \text{ GeV}$
- $|\eta| < 2.4$
- pass jet isolation
- medium ID

## 6.8.2 Category selection

The analysis includes two main categories: the dilepton category and the exclusive track category. The dilepton category requires two fully-identified leptons, both of which are muons. In contrast, the exclusive track category includes a single lepton and a track that has not been identified as a lepton. Both electrons and muons are accepted as the single lepton in the exclusive track category. The selection criteria for the dilepton category are described in Section 6.8.2.1, while those for the exclusive track category are detailed in Section 6.8.2.2.

### 6.8.2.1 Dilepton selection

In the dilepton category, the analysis requires two reconstructed and identified muons, and the following selections are applied (see also Section 6.8.2.1):

- $N_\mu = 2$  opposite charge passing the muons selection.
- $p_T(\mu_2) \leq 3.5 \text{ GeV}$  or  $\Delta R(\mu_1, \mu_2) < 0.3$ . This requirement makes this analysis orthogonal to the SOS analysis [1].
- event level BDT cut of  $\text{BDT} > 0$ . This is the main method of selecting signal events while rejecting the SM background. See Section 6.8.3 for details.
- $\Delta R(\mu_{1,2}, \text{leading jet}) > 0.4$ . The leptons should not be inside the ISR jet.
- $\omega$ ,  $\rho^0$  and  $J/\psi$  invariant mass vetoes.  $m_{\ell\ell} \notin [0.75, 0.81] \text{ GeV}$ ,  $m_{\ell\ell} \notin [3, 3.2] \text{ GeV}$ .

### 6.8.2.2 Exclusive track selection

The exclusive track category requires one reconstructed and identified lepton, which can be either an electron or a muon, and an exclusive track, meaning a track that is not identified as a lepton. The track with the highest track BDT score, as described in Section 6.6.6, is chosen to act as the misidentified lepton. The following lists the selections for this category:

- $N_\ell = 1$  lepton passing the muons selection.
- track picking BDT cut of  $\text{BDT} > 0$ . See 6.6.6.
- event level BDT cut of  $\text{BDT} > 0$ . This is the main method of selecting signal events while rejecting the SM background. See Section 6.8.3 for details.
- $\Delta R(\ell, \text{leading jet}) > 0.4$ . The lepton should not be inside the ISR jet.

### 6.8.3 Boosted decision trees

To reject Standard Model (SM) background, select signal events, and define Signal Regions (SRs), this analysis employs multivariate Boosted Decision Trees (BDTs). For the dimuon category, one BDT is trained, while for the exclusive track category, a BDT is trained for each lepton flavor and for the two phases of the tracker detector (phase 0 and phase 1), making a total of five BDTs.

All BDTs use the same structure of 120 trees with a maximum depth of 3, with the TMVA package [8]. The BDT training is performed with AdaBoost and GiniIndex separation. We are taking all other values as the defaults set by the TMVA package.

For training, tracks are taken from a pool of privately produced FASTSIM signal simulations listed in Section 6.5.2 for the signal, and standard model background simulation listed in Section 6.5.1 for the background. For the exclusive track category, simulations from 2016 and 2017 are used to represent phase 0 and phase 1 of the tracker, respectively. For the dimuon category, only 2017 simulations are used to represent both phases, with an added systematic uncertainty resulting from this choice.

For the pool of the privately produced FASTSIM signal simulations, the full range of simulated higgsino parameter  $\mu$  (or the mass of  $\tilde{\chi}_1^\pm$  in case of phase 1) is being selected, but only the range of  $\Delta m$  targeted by the analysis. For phase 0,  $\Delta m^0$  is selected in the range of [0.3, 4.3] GeV and  $\mu$  is selected in the range of [100-130] GeV. For phase 1,  $\Delta m^\pm$  is selected in the range of [0.3-4.6] GeV and  $\mu$  is selected in the range of [100-500] GeV. The baseline selection described in Section 6.8.1 has been applied, and a subset of the selections listed in Section 6.8.2.1 and Section 6.8.2.2 is used for training:

- $N_\mu = 2(1)$  opposite charge passing the muons selection for the dimuon category (for the exclusive track category).
- $\Delta R(\ell, \text{leading jet}) > 0.4$ .
- track picking BDT cut of  $\text{BDT} > 0$  for the exclusive track category.

The training was conducted without using MC weights to avoid overtraining that can arise from high weighted MC events. The training produced satisfactory results because the kinematics of low- $p_T$  leptons are expected to be similar across all SM background processes. When examining the training input variable distributions in the following sections, this fact must be taken into account. The distributions are plotted without MC weights and with signal events taken from a pool of different parameter values as described above. Therefore, the ROC curves cannot be understood as a simple signal efficiency versus background rejection. Each BDT output working point results in a different signal efficiency depending on the signal parameter values. As will be seen later, one does not use a single value of BDT with a simple cut and count. Instead, the SRs are binned according to BDT output values. Therefore, the ROC curve is plotted with a default cut of 0.0 for the sake of completeness. To fully estimate the power of the training, one needs to consider the significance when each signal point has been properly weighted together with the background processes from the SM.

#### 6.8.3.1 Dimuon category

The training samples for the dimuons category contain 4350 signal events and 21842 background events. The training samples are then tested against test samples of the same size. The distributions of the testing samples overlay on the training samples, as well as the ROC curve, as shown in Figure 6.35. No significant overtraining is observed.

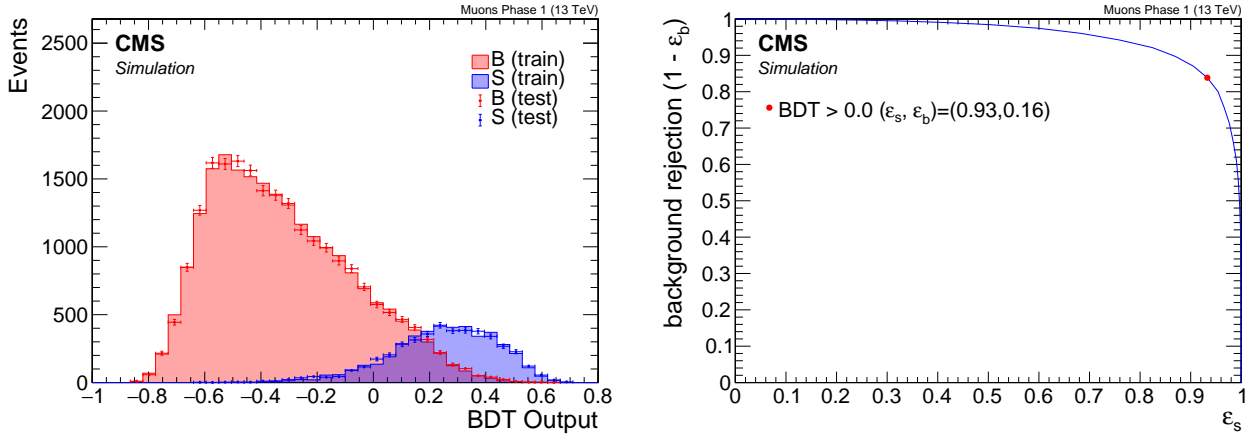


Figure 6.35: Dimuon BDT output (left) and ROC curve (right).

Table 6.9: Dimuon BDT input variables

Rank	Variable	Description
1	$m_{\ell\ell}$	invariant mass
2	$p_T(\ell_1)$	leading lepton $p_T$
3	$H_T^{\text{miss}}$	
4	$H_T$	
5	$\Delta R(\ell\ell)$	
6	$\min \Delta\phi \left( \vec{H}_T^{\text{miss}}, \vec{j} \right)$	
7	$p_T(\vec{\ell}_1 + \vec{\ell}_2)$	dilepton $p_T$
8	$p_T(\text{leading jet})$	
9	$p_T(\ell_2)$	subleading lepton $p_T$
10	$\eta(\ell_1)$	leading lepton $\eta$
11	$m_T(\ell_1)$	leading lepton transverse mass
12	$ \Delta\phi \left( \ell_2, \vec{H}_T^{\text{miss}} \right) $	
13	$ \Delta\phi \left( \ell_1, \vec{H}_T^{\text{miss}} \right) $	
14	$ \Delta\phi(\ell\ell) $	
15	$N_{\text{jets}}$	Number of jets
16	$\eta(\text{leading jet})$	
17	$ \Delta\eta(\ell\ell) $	
18	$m_{\tau\tau}$	collinear approximation of $m_{\tau\tau}$

The training uses 18 different variable listed in Table 6.8.3.1 in decreasing order of importance ranking.

Distributions of the input variables to the BDT training can be seen in Figure 6.36. As mentioned before, the signal is taken from a pool of a range of model points, and events are not weighted to any luminosity or cross section in order to avoid over training.

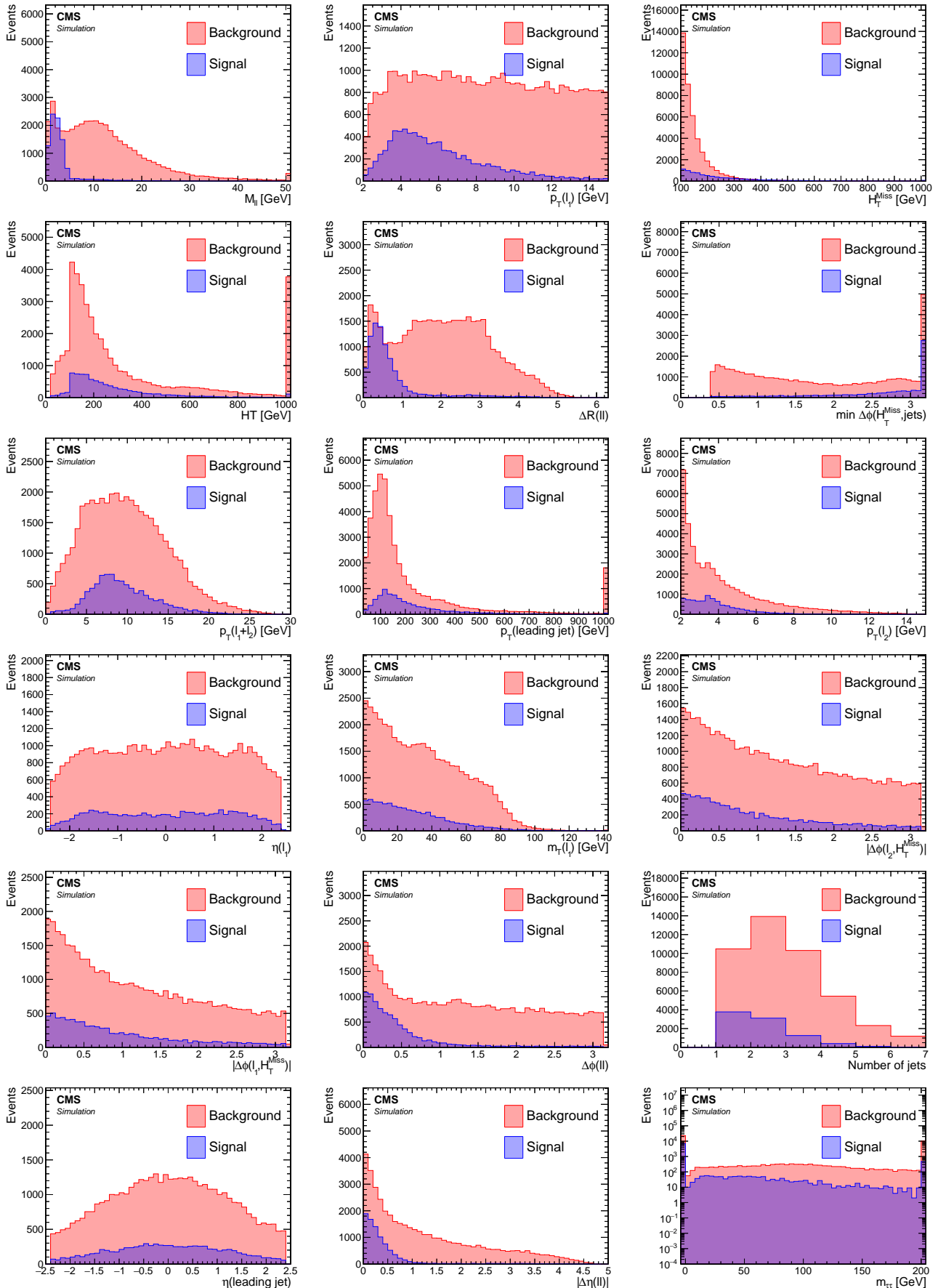


Figure 6.36: Dimuon BDT training input variables. Ordered by importance ranking.

### 6.8.3.2 Exclusive track category

The training samples in phase 0 for the exclusive category contain 7863 (1750) signal events and 55765 (29135) background events for muons (electrons) flavor. For phase 1, the exclusive category contain 5266 (1332) signal events and 51308 (31149) background events for muons (electrons) flavor. The training samples are then tested against the test samples of equal size. The distributions of the testing samples overlay on the training samples are seen in Figure 6.37. No significant over training is observed. The ROC curves are seen in Figure 6.38.

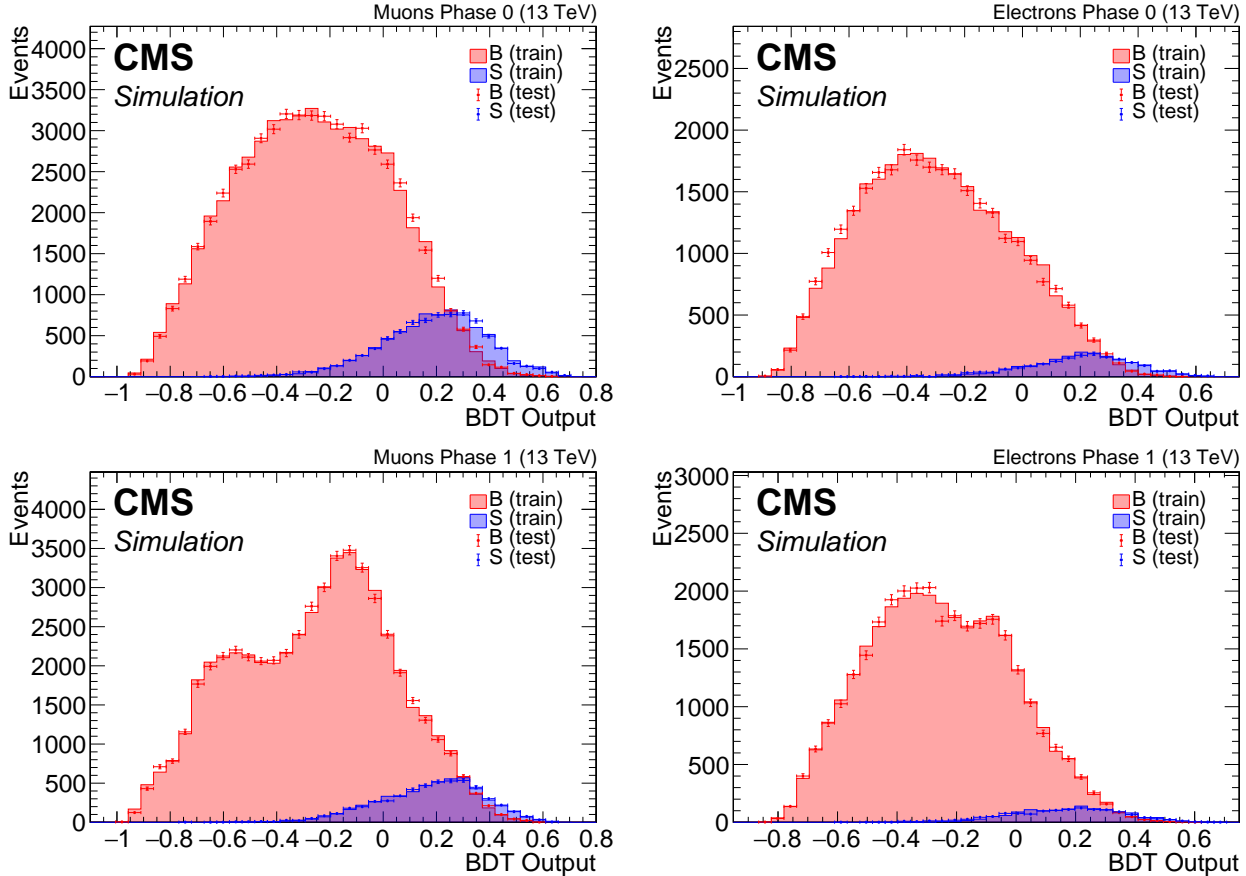


Figure 6.37: Exclusive track category BDT output in phase 0 (top) and phase 1 (bottom) for muons (left) and electrons (right)

The training uses 18 different variables listed in Table 6.8.3.2 in decreasing order of importance ranking. Since the ranking is slightly different in the four trainings, the order in the case of the muons of phase 1 is chosen to be listed here. The fully identified lepton is denoted as  $\ell$  and the non-identified lepton track as  $t$ .

Distributions of the input variables to the BDT training can be seen in Figure 6.39. As mentioned before, the signal is taken from a pool of a range of model points, and events are not weighted to any luminosity or cross section in order to avoid over training. In the following sections we fully weighted distributions will be shown in order to asses the performance of the training for different model points and to understand the different components of the standard model background and how to estimate it properly.

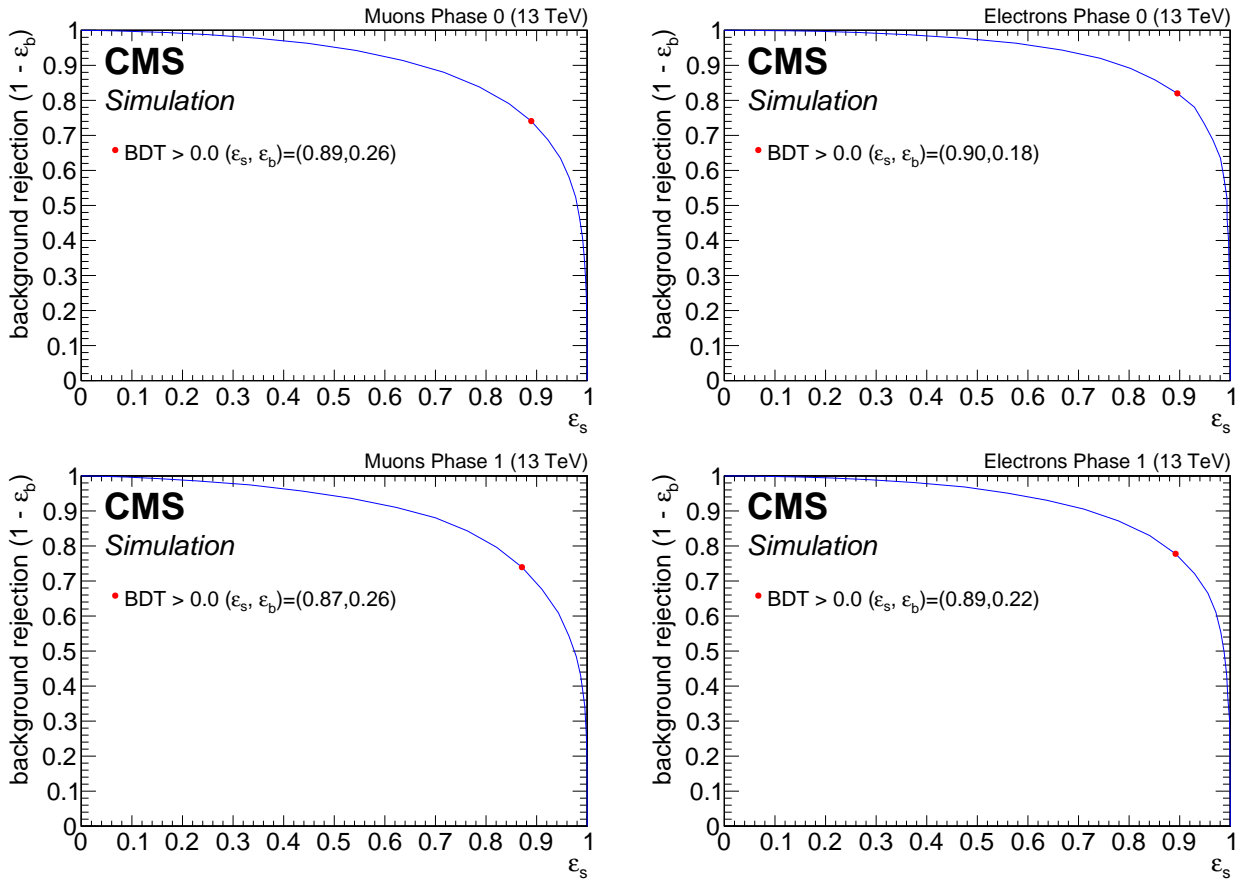


Figure 6.38: Exclusive track category ROC curves in phase 0 (top) and phase 1 (bottom) for muons (left) and electrons (right)

Table 6.10: Exclusive track BDT input variables

Rank	Variable	Description
1	$p_T(\ell)$	lepton $p_T$
2	$H_T$	
3	$H_T^{\text{miss}}$	
4	$\min \Delta\phi \left( \vec{H}_T^{\text{miss}}, \vec{j} \right)$	
5	$p_T(\text{leading jet})$	
6	$N_{\text{jets}}$	Number of jets
7	track BDT output	
8	$\eta(t)$	
9	$p_T(t)$	track $p_T$
10	$\eta(\text{leading jet})$	
11	$m_{\ell\ell}$	invariant mass
12	$\eta(\ell)$	
13	$m_T(\ell)$	lepton transverse mass
14	$\Delta R(\ell, t)$	
15	$\phi(\ell)$	
16	$\phi(t)$	
17	$ \Delta\phi(\ell, t) $	
18	$ \Delta\eta(\ell, t) $	

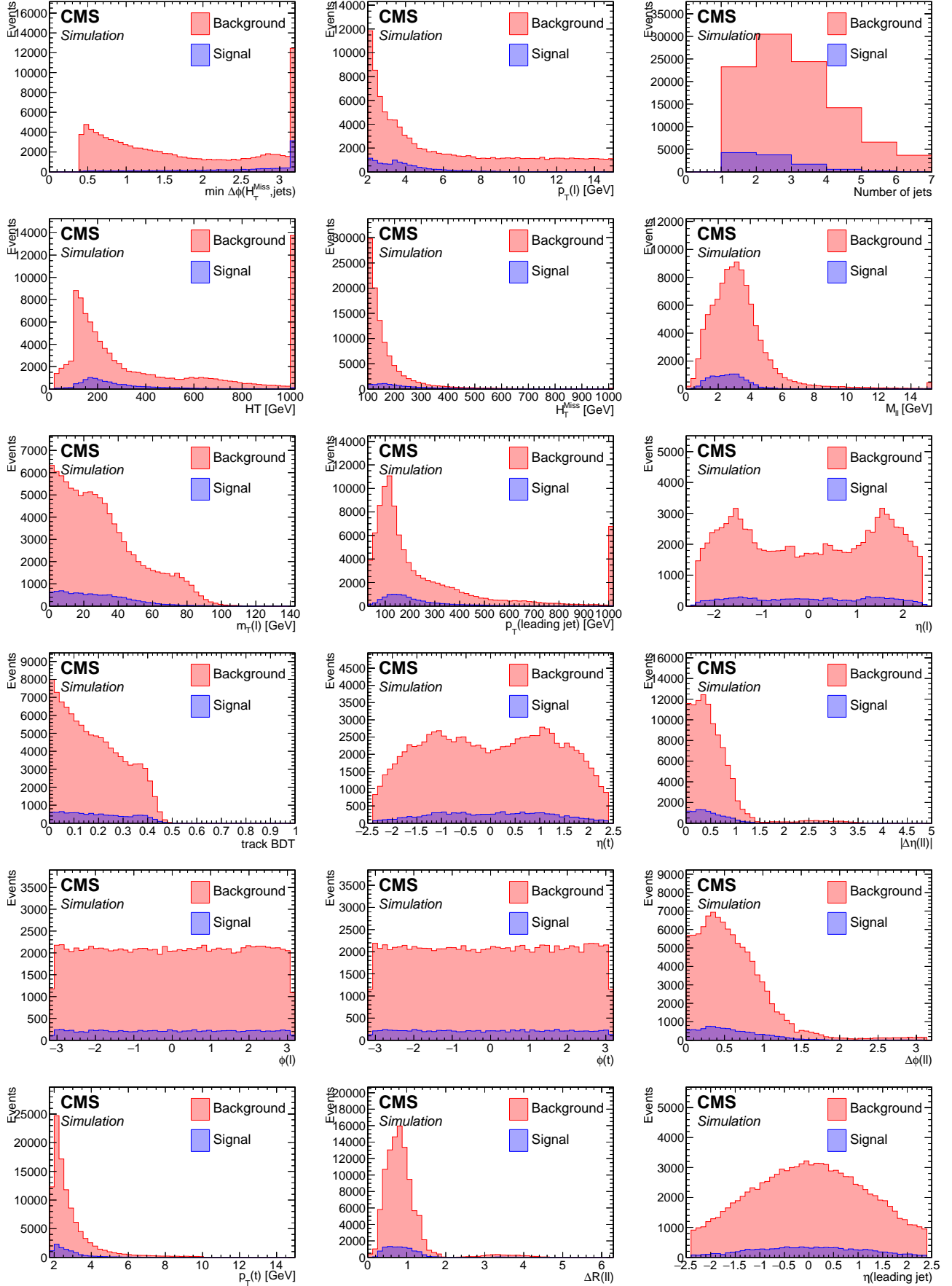


Figure 6.39: Exclusive track BDT training input variables. Ordered by importance ranking.

## 6.9 Characterization and estimation of the Standard Model backgrounds

To have a solid analysis strategy, a thorough study and estimation of the Standard Model (SM) background is necessary. It is important to fully understand the characteristics and composition of the SM background, both to maximally reject it in the Signal Regions (SRs) and to construct a reliable method for estimating it. The characterization of the SM backgrounds is examined in Section 6.9.1, while the estimation of the backgrounds is explored in Section 6.9.2.

### 6.9.1 Characterization of the Standard Model backgrounds

Signal Regions (SRs) are defined by a set of cuts or selections on observables composed of detector readings. Equivalently, multivariate techniques can be used to cut on a single aggregated output observable devised from a set of input variables, as was done in this analysis. Regardless of how a SR is defined, usually not only signal processes will be measured, but also processes that are not the intentions of the analysis. These processes are referred to as background to the analysis. Background processes can arise due to truly similar final-state physics or due to detector effects and mismeasurements. In the current analysis, an example of a background in the dimuon category that arises from truly similar physics is Drell-Yan. In a Drell-Yan process, opposite-charge same-flavor dilepton pairs are produced from an off-shell  $Z^*$  or  $\gamma^*$ . An example of a background process that is due to mismeasurement is the production of a W in association with jets, where one lepton comes from the leptonic decay of the W, and another lepton is due to either mismeasurement, i.e., a fake lepton, or as part of a hadronization procedure. A full list of the SM processes taken into account in this analysis, along with descriptions, is given below. The processes are ordered according to their contribution in the SRs of the dimuon category.

- **W in association with jets.** In this SM process, a W boson is produced alongside jets and decays leptonically into a lepton and a neutrino. It can be represented symbolically as  $W + \text{jets} \rightarrow \ell\nu$ . There are several reasons why this process is considered as background in this analysis. Firstly, since a neutrino is produced in this process, it contributes to the production of some real missing transverse momentum. Secondly, the presence of jets makes it highly likely to pass the selection of at least one jet in the event. Thirdly, energy mismeasurement of the jets can also contribute to the presence of fake missing transverse momentum, that is,  $E_T^{\text{miss}}$  due to mismeasurements rather than real physics. Lastly, the very loose transverse momentum  $p_T$  range of the analysis muons makes it highly probable to pick an additional lepton in the event. In the exclusive track category, the extra track is mostly a fake lepton, that is, a track that was misidentified by the BDT selection as the second lepton. In the dimuon category, it is either a fake misidentified lepton or a low- $p_T$  lepton originating from a decay chain in a hadronization process.
- **Z in association with jets.** In this SM process, there is a production of a Z boson alongside jets, decaying into two neutrinos. It can be written schematically as  $Z + \text{jets} \rightarrow \nu\bar{\nu}$ . The two neutrinos in this process contribute to true missing transverse momentum in the event. The two leptons will then come from either a decay of a meson produced in the hadronization procedure, or from unrelated decays. Another highly likely scenario is for one of the leptons to be fake, just like in the  $W + \text{jets} \rightarrow \ell\nu$  case.
- **Drell-Yan process.** It takes place when a quark from one proton and an antiquark from another proton annihilate, creating a virtual photon or  $Z^*$  boson that decays into a pair of oppositely-charged leptons. When two electrons are produced via  $Z \rightarrow e^+e^-$  or two

muons via  $Z \rightarrow \mu^+ \mu^-$ , true missing transverse momentum is not part of the production. Therefore, a relatively high  $E_T^{\text{miss}}$  cut, as used in this analysis, is successful in suppressing these types of backgrounds. However, in the production of two taus via  $Z/\gamma^* \rightarrow \tau^-\tau^+$ , each tau can decay into a muon alongside two neutrinos, i.e.,  $\tau \rightarrow \mu\bar{\nu}_\mu\nu_\tau$ , producing real missing transverse momentum in the event alongside two real leptons, which then become a background to this analysis.

- **Ditop in association with jets.** When two top quarks are produced,  $t\bar{t}$ , they mostly decay into a W boson and a b quark, with a decay rate close to 100%. Therefore,  $t\bar{t}$  becomes a background when each top quark decays into a b quark and a leptonically decaying W boson. The W boson produces neutrinos in the decay alongside the leptons, contributing to real missing transverse momentum. Although vetoing b-tagged jets, as listed in Section 6.8.1, is successful in suppressing most of this background, it is not effective in eliminating it entirely.
- **Numerous bosons production.** In the plots presented in the following section, diboson production (VV) is distinguished from higher-order productions such as three bosons, which are collectively referred to as *rare*. The ways in which they can be selected in the SRs are similar to the single boson case. However, the higher-order multiplicity events have much lower production cross sections, and are therefore almost negligible in this analysis.
- **QCD production.** Quantum Chromodynamics (QCD) comprises events arising from the production and radiation of quarks and gluons followed by their hadronization and showering into highly columnar sprays of particles known as jets. QCD events contain no real  $E_T^{\text{miss}}$ . Any  $E_T^{\text{miss}}$  present in a QCD event is due to mismeasurements. The relatively high  $E_T^{\text{miss}}$  cut in this analysis, in combination with requiring  $\min \Delta\phi(\vec{H}_T^{\text{miss}}, \vec{j}) > 0.4$ , reduces almost all QCD background, and therefore it is a very negligible background in this analysis. That is the reason why it can be safely disregarded in most contexts, and we can assume that any remaining events will be successfully estimated using the jetty-background data-driven background estimation method in Section 6.9.2.1.
- **Resonances.** Resonances are composite particles, namely mesons or baryons, which can later decay into leptons. The highest contribution in this category comes from the  $J/\psi$ , which has a mass of 3.1 GeV with a relatively high cross section. In order to reduce this background, invariant mass vetoes for the  $\omega$ ,  $\rho^0$ , and  $J/\psi$  are applied in the range of  $m_{\ell\ell} \in [0.75, 0.81]$  GeV and  $m_{\ell\ell} \in [3, 3.2]$  GeV.

The optimal way to gain an understanding of the proportion of each background process in the Signal Regions (SRs) is to examine correctly weighted MC simulations, where each process is weighted according to its corresponding production cross section, and the overall background is weighted to match the era luminosity. It is useful to examine the final SRs defined and discussed in Section 6.11, as well as some of the important inputs to the BDT discussed in Section 6.8.3. In the following sections, note that the SRs are all the bins with a BDT value greater than zero. Each of the following sections presents figures relevant to the respective analysis category, beginning with the BDT output distributions and SRs bins, followed by important inputs to that BDT. Although input distributions have been previously seen in Section 6.8.3, here the background processes and individual signal models are appropriately weighted. The year 2017 was chosen as a representative data-taking year.

### 6.9.1.1 Dimuon category

The weighted dimuon 2017 simulation BDT output, both in log and linear scales, can be seen in Figure 6.40. The SRs are the six bins with a BDT output greater than zero, ordered by increasing sensitivity. The largest backgrounds in the dimuon channel are  $t\bar{t}$ ,  $Z + \text{jets} \rightarrow \nu\nu$ , and  $W + \text{jets} \rightarrow \ell\nu$ , with a small contribution from Drell-Yan processes mainly due to  $Z/\gamma^* \rightarrow \tau^-\tau^+$ . Figure 6.41 shows the top ten input observables to the BDT ranked by importance for the training. All figures are weighted to the 2017 luminosity.

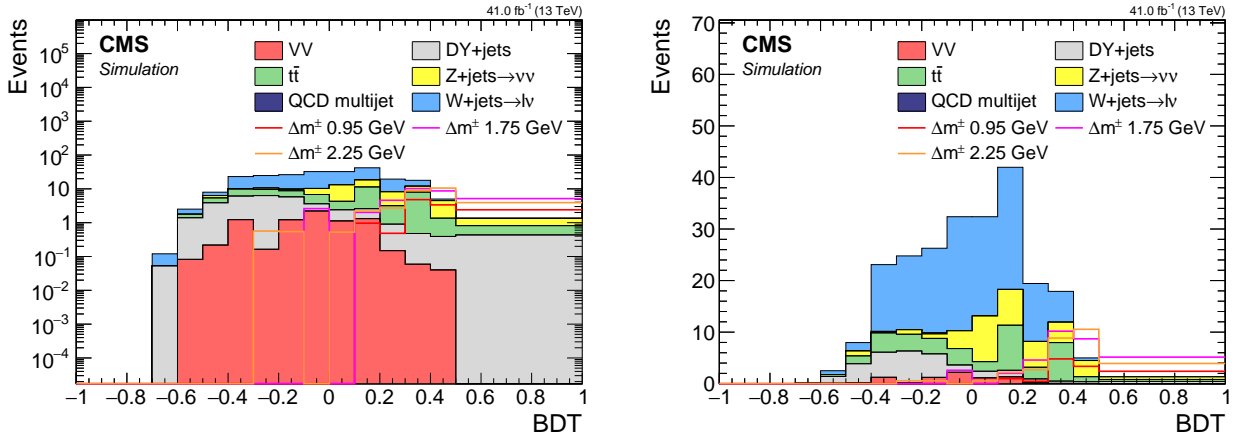


Figure 6.40: Dimuon 2017 simulation BDT output in log scale (left) and linear scale (right).

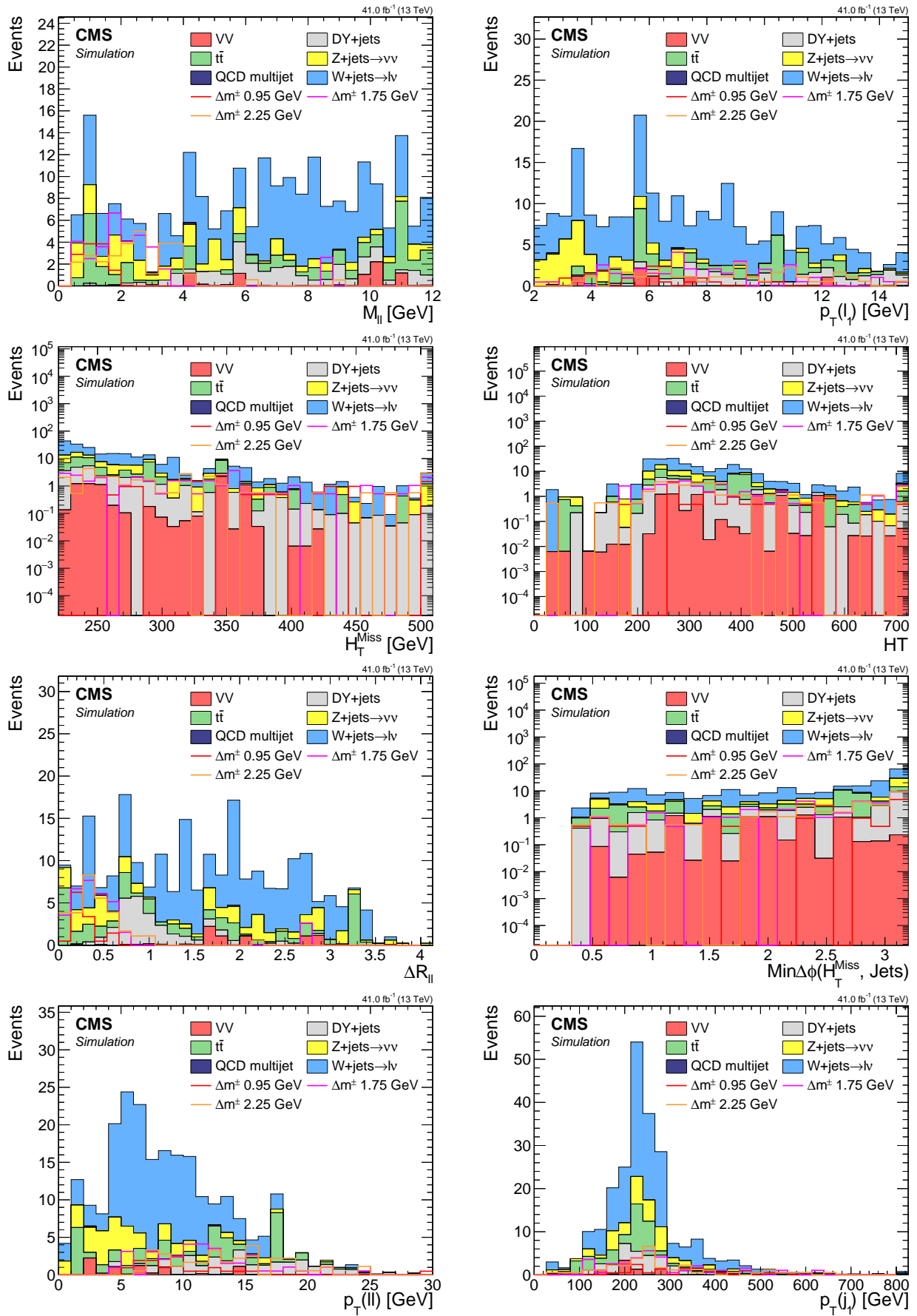


Figure 6.41: Dimuon 2017 simulation BDT inputs for the top 10 ranked observables.

### 6.9.1.2 Exclusive track category

As described before, there are four BDTs in the exclusive track category, for each of the two lepton flavors there are two track phases.

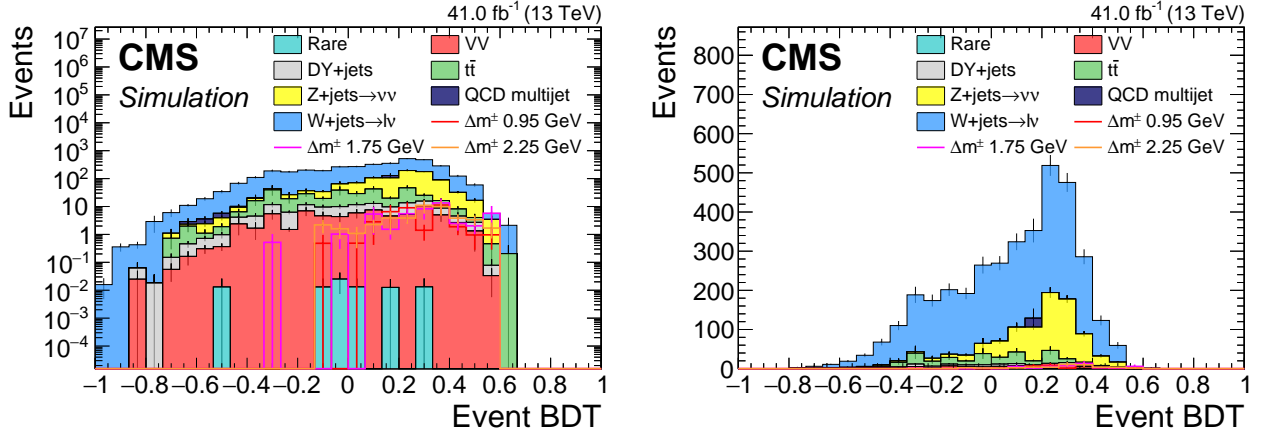


Figure 6.42: Exclusive track plus muon category 2017 simulation BDT output in log scale (left) and linear scale (right).

The muon flavor in phase 1 is chosen to represent background composition in the exclusive track category in order to avoid repetition, and can be seen in Figure 6.42. Figure 6.43 shows the top eight input observables to the BDT, ranked by importance for the training. It is weighted to 2017 luminosity and uses 2017 simulation. A few signal points are also plotted in order to point to the signal-like regions of phase space.

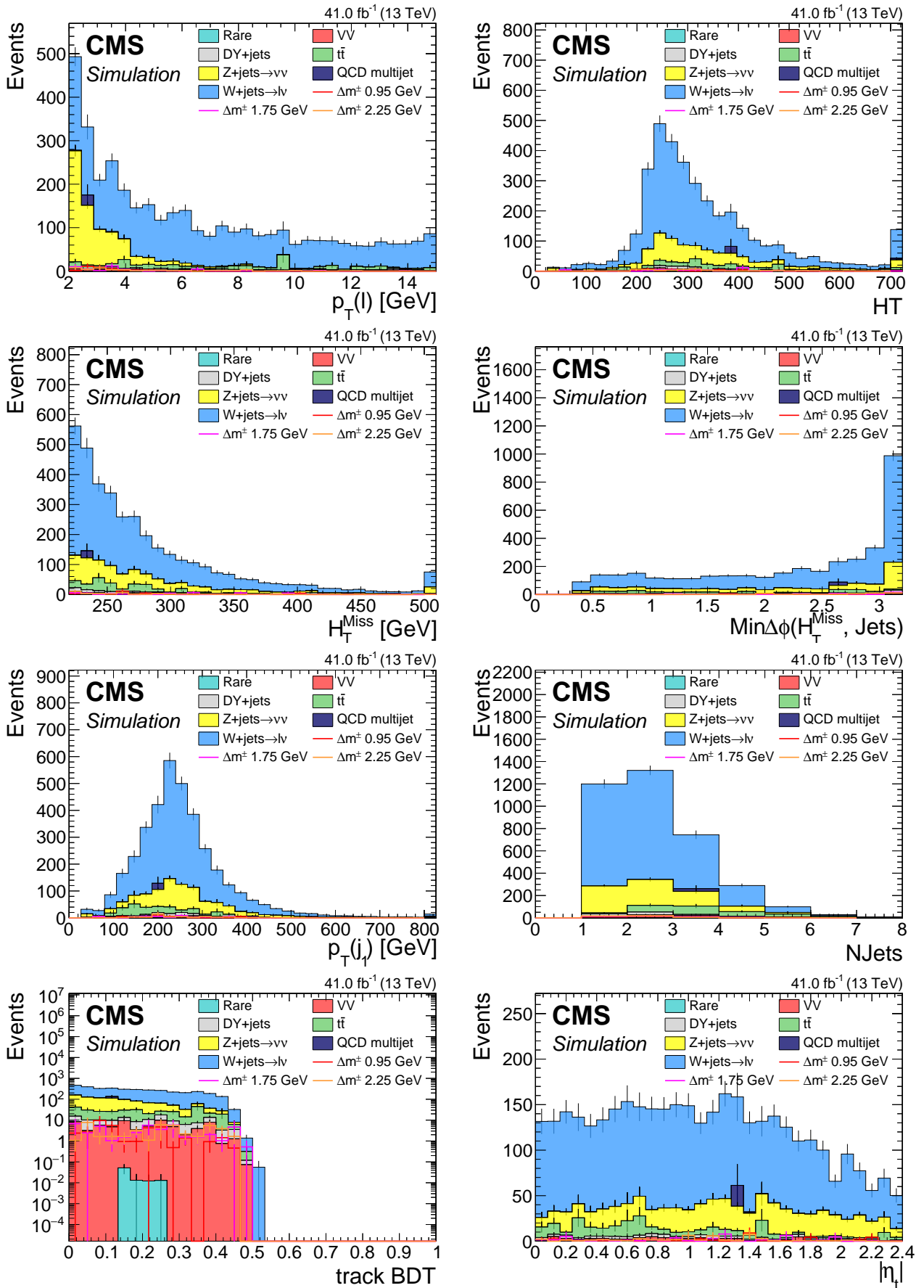


Figure 6.43: Exclusive track plus muon 2017 simulation BDT inputs for the top 8 ranked observables.

### 6.9.2 Estimation of the Standard Model backgrounds

In analyses such as the one described in this thesis, in which new physics or physics beyond the Standard Model is searched for, predicting event counts for the signal and Standard Model background is crucial. The signal event count is denoted as  $s$ , and the background event count as  $b$ . Using these counts and their uncertainties, a *significance* is computed. A widely used method for predicting these counts is Monte Carlo (MC) simulation, sometimes referred to as *simulation*. The simulation process involves generating many events using the MC technique, taking into account the detector's geometry (through algorithms like FASTSIM or FULLSIM). These events are then weighted to account for production cross-sections and luminosity. Additional correction factors and weights may apply to account for measurement errors, discrepancies between data and simulation, non-ideal algorithms, misidentifications, normalization corrections computed from data in a dedicated Control Region (CR), and other factors. The nominal prediction for the event count becomes the fully-weighted simulation count in the relevant Signal Region (SR), with an uncertainty taken from the statistical error on the simulation count in that bin and an optional systematic uncertainty determined by other means. The signal count  $s$  has been determined in this way using FASTSIM. As described in the following sections, only a small fraction of the background count  $b$  has been estimated using simulation. The majority of the background processes have been estimated using *data-driven methods*.

Using simulation to estimate the Standard Model background has limitations and disadvantages that are specific to each analysis, as the background process composition changes. The main limitation of simulation is its imperfection. Simulation can never precisely simulate real data due to several factors. Theoretical uncertainties, such as uncertainties on cross sections or branching fractions, can lead to incorrect production rates or normalization. Therefore, simulation is often reweighted using a normalization factor derived from a dedicated CR. Another challenging limitation of simulation is the misrepresentation of the detector's delicate geometry and response, as well as real-time data-taking challenges and faults that need to be taken into account for the simulation to accurately represent the events that would have been recorded by the detector. Some objects and phase-spaces are more prone to discrepancies than others.

In this analysis, a significant challenge arises from the soft nature of the leptons, with low transverse momentum ( $p_T$ ) and low invariant mass of the order of a few GeV. The sources of background for such events in the standard model include low- $p_T$  resonances produced in hadronization processes, and events where one of the leptons or exclusive tracks is misidentified as one of the signal leptons. These leptons or tracks are often in close proximity to jets in the event. The analysis uses two strategies to estimate this type of background, depending on whether two identified leptons are present, as in the dimuon category, or only one, as in the exclusive track category. The jetty background estimation for dimuon is described in Section 6.9.2.1, while the exclusive track background estimation is described in Section 6.9.2.3. As described earlier, a small portion of the background, namely  $Z/\gamma^* \rightarrow \tau^-\tau^+$ , is not produced near jets at all, and the method for estimating this background is described in Section 6.9.2.2.

### 6.9.2.1 Jetty background estimation

In the description of the object selection in Section 6.6, it has been demonstrated that the leptons in the signal are isolated. The isolation criterion used in this analysis has been described in Section 6.6.7, and is referred to as *jet-isolation*. It has been mentioned there that customized isolation is also a key part of the background estimation, which is now described in this section. This background estimation method is relevant to the dimuon category. It is a *data-driven* background estimation method, meaning that data, rather than simulation, is used to estimate this background. The name *non-isolated jetty background* refers to the background in which one or both of the leptons are generally produced in association with jets and are typically close to one. Most of these leptons are rejected by the jet-isolation criteria, but some do manage to pass the isolation if they happen to have been produced far enough from a jet.

The signal regions are detailed in Section 6.11, and it is worth noting that they are defined as bins in the BDT output with a score greater than zero. The strategy employed in this method involves identifying a Control Region (CR) that produces a BDT output distribution that is shape-consistent with the original BDT distribution. This is achievable when a CR can be found that has almost the same characteristics as the main region, ideally only differing in rate. To ensure correct normalization, a normalization control region is defined to account for the different production rate.

Note on terminology for clarity: The SRs are defined by taking BDT output greater than zero, and therefore, by definition, the region with less than zero becomes a CR. Furthermore, a new region using isolation is being introduced in this section. Since the orthogonal region only varies from the main region by isolation, it is referred to as the *isolation sideband*. The main region that was used to define the SRs using the BDT output is referred to as the *main band*. The SRs are then regions in the *main band* with BDT output greater than zero. The events in the *isolation sideband* are used to predict the jetty-background in the *main band*. The *normalization region* is taken to be in the CR with  $BDT < 0$ , and can also be referred to as the *BDT sideband* or, more elaborately, the *BDT normalization sideband*. Of course though, a *sideband* is still a type of CR.

The goal of this estimation method is to estimate the jetty-background, and an isolation sideband is defined by requiring either one or two of the leptons to fail the jet-isolation criterion, which was defined in step 5 in Section 6.6.7. This means that the lepton is within a distance of less than 0.6 in  $\Delta R$  from a lepton-corrected jet. The jet that caused the lepton to fail the jet-isolation is required to have an original transverse momentum, i.e., transverse momentum before the subtractions, satisfying  $15 < p_T < 30 \text{ GeV}$ . The upper bound of 30 GeV is chosen because 15 GeV is the upper bound on the leptons, and 30 GeV is the lower bound on the objects being summed in the calculation of  $H_T^{\text{miss}}$  and the number of jets in the event. If the upper bound had not been set, a bias in the isolation sideband would have been introduced because requiring a lepton to fail jet-isolation would potentially mean requiring an extra jet with  $p_T > 30 \text{ GeV}$ , a requirement that did not exist in the main band. The distributions of the number of jets and  $H_T^{\text{miss}}$  are blind to jets with  $15 < p_T < 30 \text{ GeV}$ , which makes it safe to potentially have extra jets in that region. The BDT training will be blind to those jets, and the BDT shape in the sideband should not be affected by those, thus achieving the goal of having consistent shapes between the main band and the sideband.

The main assumption underlying the use of the isolation sideband is that, in the background, the leptons are not isolated but are created in association with jets. Most of them are produced inside the jets, with a smoothly falling distribution outwards from the jet. By setting a cone of size 0.6 around the jets and selecting leptons inside those cones, events are picked up that have similar behavior to events where the leptons are outside of those cones. The rate of lepton production inside jets will be much higher than those outside of the jets, but since their behavior is similar kinematically, their distributions will agree with those in the main band by fixing the

normalization. The normalization factor is calculated by taking the ratio between the main band and the isolation sideband in the CR of  $\text{BDT} < 0$ . The event count in the sideband is then multiplied by the normalization factor to make up the prediction. The prediction in the SR then becomes:

$$N_{\text{predicted}}^{\text{SR}} = \frac{N_{\text{main band}}^{\text{CR}}}{N_{\text{sideband}}^{\text{CR}}} \cdot N_{\text{sideband}}^{\text{SR}}. \quad (6.10)$$

To test the assumption that the isolation sideband, i.e., events with at least one of the leptons failing the jet isolation criterion, correctly predicts the shape of the main band in the signal region, a shape comparison is performed in simulation. This shape comparison, also known as a *closure test*, is carried out by simultaneously plotting the main band and the jet isolation sideband and checking that they statistically agree in terms of shape. A normalization factor is computed to correctly normalize the isolation sideband. In this section, we present the treatment of phase 1 (2017-2018), which in simulation is represented by 2017 MC. Special care has been taken in the case of phase 0 (2016 data taking year), which is discussed in Section 6.12.

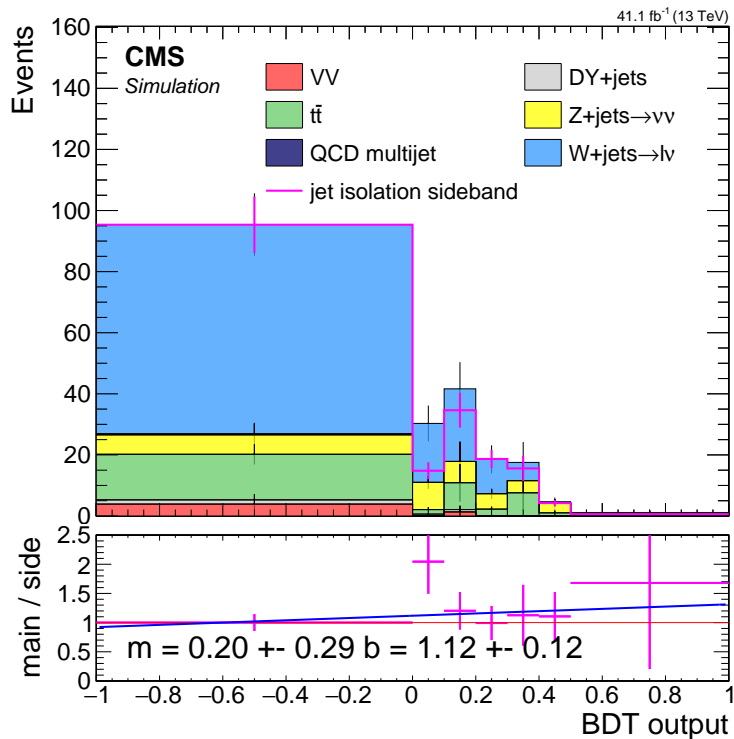


Figure 6.44: Dimuon 2017 jetty background closure plot. The stack represents simulation in the main isolation band after  $Z/\gamma^* \rightarrow \tau^-\tau^+$  has been removed, while the pink line represents simulation in the isolation sideband. The isolation sideband is normalized to match the isolation in the CR of  $\text{BDT} < 0$ . The ratio panel shows the ratio between the isolatoin main band and sideband. A line fit of the ratio is performed and the parameters of the slope  $m$  and interception point  $b$  with their respective errors are stamped.

Figure 6.44 shows the jetty background closure plot. This plot tests the assumption that the background in the isolation main band can be predicted by the isolation sideband. After proper normalization, which is achieved by dividing the event count in the main band with the event count in the sideband (0.59 in this case), a flat ratio distribution is expected in the SR. As can be seen from the plot, such a flat ratio distribution has been achieved, and most bins are statistically consistent with unity. To check for any trend, a line fit has been performed for the ratio panel. Taking into account the errors, the slope  $m$  is consistent with 0 and the intercept  $b$

is consistent with 1 within  $1\sigma$ , indicating that the line is consistent with a flat line intercepting 1. Therefore, it can be concluded that the closure plot confirms the shape assumption, and no trend needs to be taken into account. The full list of transfer factors with the associated uncertainties can be found in Section 6.12.1, while the special treatment of the 2016 case is discussed in Section 6.12.2.

### 6.9.2.2 Ditaum Drell-Yann background estimation

It has been observed in Section 6.9.1.1 that the majority of the Standard Model background is composed of processes that produce leptons in association with jets. Therefore, it can be estimated using the jetty-background data-driven estimation method described in Section 6.9.2.1. However, a small amount of background arising from  $Z/\gamma^* \rightarrow \tau^-\tau^+$  is also present. Since the leptons resulting from the leptonic decay  $\tau \rightarrow \mu\bar{\nu}_\mu\nu_\tau$  are isolated, it requires an alternative background estimation method.

The  $Z/\gamma^* \rightarrow \tau^-\tau^+$  background in this category is estimated using MC simulation. The event counts are weighted according to a data correction normalization factor calculated in a dedicated CR that is rich and relatively pure in  $Z/\gamma^* \rightarrow \tau^-\tau^+$  background. To achieve this, the observable  $m_{\tau\tau}$  must be introduced. The background arises from a Drell-Yann process where a Z decays into two tau leptons, which in turn decay into muons via  $\tau \rightarrow \mu\bar{\nu}_\mu\nu_\tau$ . If the taus could be reconstructed, their invariant mass,  $m_{\tau\tau}$ , could be used, which is expected to peak around the Z mass. The Z resonance could then be used as the desired CR rich in ditaum background. However, since leptonic taus are not directly reconstructed at CMS, an alternative approach must be found to calculate the invariant mass.

A widely used method for the reconstruction of the invariant mass  $m_{\tau\tau}$  is the *collinear approximation*. First described in [12], it has been used widely in ATLAS [13] and CMS [14]. In the collinear approximation, one assumes that the tau pair produced from  $Z/\gamma^*$  are highly energetic, such that their leptonic decays are collinear, and the source of missing transverse momentum is due to the neutrinos only. If both  $\tau$ -leptons are sufficiently boosted, the neutrinos from each  $\tau$  decay are collinear with the visible lepton momentum. One can then use the visible daughter-lepton momentum together with  $\vec{p}_T^{\text{miss}}$  to reconstruct the  $\tau$ -lepton pair and calculate the would-be  $m_{\tau\tau}$  invariant mass. Depending slightly on the mathematical details of the approximation, one can arrive at a strictly positive distribution for  $m_{\tau\tau}$ , as was done, for example, in [15], or one that also has negative values, as was done in [16, 17]. Since the negative values arising from the second variation of the approximation are due to events where  $\vec{p}_T^{\text{miss}}$  points away from one of the leptons, and therefore not arising from underlying boosted ditaum events, it is useful to reject negative values in order to purify the CR by rejecting those events. The collinear approximation does not work when the taus are back-to-back. However, since in this analysis an ISR jet is required together with a high threshold of missing transverse momentum, it is expected to work well on the remaining boosted events. The signal, as well as other Standard Model processes, are expected to have a flat distribution in  $m_{\tau\tau}$ , while events arising due to  $Z/\gamma^* \rightarrow \tau^-\tau^+$  are expected to peak around the Z boson mass.

To put these assumptions into practice, let's lay out an explicit definition of  $m_{\tau\tau}$ . The invariant mass is defined as:

$$m_{\tau\tau}^2 = (p_{\tau_1} + p_{\tau_2})^2 \quad (6.11)$$

Assuming that the  $\tau$ -pair is boosted and the fully leptonic decay products are fully collinear to the  $\tau$ -leptons, it follows that the transverse momentum of each neutrino pair is proportional to the corresponding  $\tau_i$ 's transverse momentum by a scale factor  $\xi_i$ :

$$\vec{p}_T^{\nu_i} = \xi_i \vec{p}_T^{\tau_i} \quad (6.12)$$

Since by assumption, all of the missing transverse momentum is due to the neutrinos, it follows that:

$$\vec{p}_T^{\text{miss}} = \xi_1 \vec{p}_T^{\tau_1} + \xi_2 \vec{p}_T^{\tau_2} \quad (6.13)$$

One solves the above two equations 6.13 for the two parameters  $\xi_1$  and  $\xi_2$  for each event. The solution becomes:

$$\begin{aligned} \xi_1 &= \frac{\vec{p}_{T_x}^{\text{miss}} \cdot \vec{p}_y^{\ell_2} - \vec{p}_{T_y}^{\text{miss}} \cdot \vec{p}_x^{\ell_2}}{\vec{p}_x^{\ell_1} \cdot \vec{p}_y^{\ell_2} - \vec{p}_x^{\ell_2} \cdot \vec{p}_y^{\ell_1}}, \\ \xi_2 &= \frac{\vec{p}_{T_y}^{\text{miss}} \cdot \vec{p}_x^{\ell_1} - \vec{p}_{T_x}^{\text{miss}} \cdot \vec{p}_y^{\ell_1}}{\vec{p}_x^{\ell_1} \cdot \vec{p}_y^{\ell_2} - \vec{p}_x^{\ell_2} \cdot \vec{p}_y^{\ell_1}}. \end{aligned} \quad (6.14)$$

Equation 6.11 is expended with the assumption that the  $\tau$ 's are boosted and that the four-momenta of the taus is  $p_{\tau_i} = (1 + \xi_i)p_{\ell_i}$ :

$$\begin{aligned} m_{\tau\tau}^2 &= (p_{\tau_1} + p_{\tau_2})^2 \\ &= ((1 + \xi_1)p_{\ell_1} + (1 + \xi_2)p_{\ell_2})^2 \\ &= 2m_\tau^2 + 2(1 + \xi_1)(1 + \xi_2)p_{\ell_1} \cdot p_{\ell_2} \\ &\approx 2(1 + \xi_1)(1 + \xi_2)p_{\ell_1} \cdot p_{\ell_2}. \end{aligned} \quad (6.15)$$

This can be negative is  $\xi_i < -1$ . This can happen if the missing transverse momentum vector nearly opposite to a lepton's  $\vec{p}_T$  and also  $p_T^{\text{miss}} > p_T^\ell$ . This can easily happen in other background processes, such as WW+jets , when a neutrino and a lepton (possibly coming from different decay legs) are nearly back-to-back. Therefore, the final definition of  $m_{\tau\tau}$  is

$$m_{\tau\tau} = \text{sign}(m_{\tau\tau}^2) \sqrt{|m_{\tau\tau}^2|}. \quad (6.16)$$

The CR to be used for normalization should have low signal contamination. Figure 6.40 shows that the region of  $\text{BDT} < 0$  has hardly any signal contamination, and is therefore used to build the  $\tau\tau$  CR. Figure 6.45 displays the  $m_{\tau\tau}$  distributions for the  $\tau\tau$  simulation in red and the rest of the standard model backgrounds in the stack. The two tracker phases are presented side by side. A clear peak in the  $\tau\tau$  background is observed around the mass of the Z boson. A window around the Z boson's mass of [40, 130] GeV is chosen to achieve high purity of 73% in both phases. The contamination in data is removed by first predicting the jetty background count using the data-driven method described in Section 6.9.2.1, and subtracting those counts from the data counts in the  $\tau\tau$  dedicated CR. A data divided by simulation normalization factor is then computed in said  $m_{\tau\tau}$  window to obtain  $1.2 \pm 0.46$  ( $0.29 \pm 0.26$ ), which has a relative error of 38% (90%) for phase 0 (phase 1).

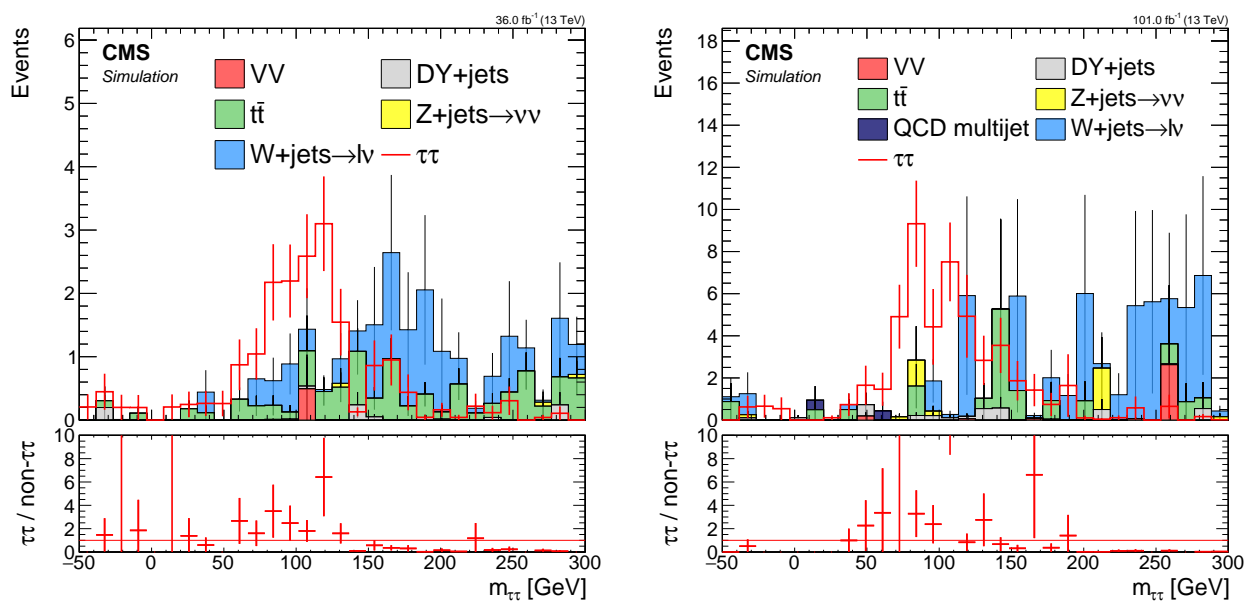


Figure 6.45: Dijet invariant mass  $m_{\tau\tau}$  distributions for phase 0 2016 simulation (left) and phase 1 2017 simulation weighted to luminosity of 2017-2018 data taking period (right). The red line corresponds to  $\tau\tau$  simulation, and the stack represents the rest of the standard model background simulation. No overflow bins are plotted in order to clearly show the resonance peak.

### 6.9.2.3 Exclusive track background estimation

The exclusive track category consists of four different BDTs, one for each lepton flavor, and for each of those, one for each phase. However, the background estimation method is the same for all of them, and it is a data-driven method.

The exclusive track category requires one fully identified lepton according to the selection listed in Sections 6.6.1 and 6.6.2, and one track selected by a procedure described fully in Section 6.6.6. The track that is selected to be paired with the single identified lepton is chosen as the track in the event with the highest BDT score among all tracks using a BDT that was trained on signal events in order to reject in-signal background and potentially pick up the track that corresponds to the non-identified second lepton in the signal event. In the background, the same selection procedure applies. However, unlike in the signal, it cannot be expected that the pairing of the selected track has a special relationship to the identified lepton other than passing some selections on the phase space. The chance of selecting a track in the background that, in combination with the identified lepton, forms an opposite-sign same-flavor pair that is a result of a resonance decay, is vanishingly small. It is highly likely that the track corresponds either to a lepton produced independently of the identified lepton in the event or that it doesn't correspond to a lepton at all. Such a track is referred to as a *fake* track, and almost all tracks in the event are fakes.

To devise a successful data-driven background estimation for the exclusive track category, advantage is taken of the fact that the tracks in the background are independent of the identified lepton in the event. The selection process considered only tracks with opposite charge to the identified lepton, but if the track is independent of the lepton, events with a track of the same charge will be picked at the same rate as opposite charge ones. Not only is it expected to be selected at the same rate, but the shape of the BDT output will also be blind to this choice, making it an excellent proxy to the opposite charge background.

A CR is defined by selecting a same-charge lepton-track pair rather than an opposite-charge pair as in the SR. It is expected that the same-charge CR is consistent with the normalization of the SR, since it is expected that these events are selected at the same rate as each other. Despite this, the normalization is fixed by calculating a normalization factor as the ratio between the opposite-charge and same-charge event count in a dedicated normalization sideband CR satisfying  $\text{BDT} < 0$ , and applying it to the same-charge event count in the SRs satisfying  $\text{BDT} > 0$ . In order to test the independence assumption and to demonstrate the correct shape and normalization prediction, a closure test is performed in simulation. Figure 6.46 demonstrates closure tests for muons and electrons for both tracker phases. The stack represents standard model background for the opposite-charge analysis selection lepton-track pair (oc), while the orange line represents the same-charge lepton-track pair (sc). Both are weighted to represent each phase's luminosity. In the ratio panel, which shows the ratio between the opposite-charge to same-charge backgrounds for each bin, a shape agreement is demonstrated which supports the assumptions made above.

After establishing that the method can be used to correctly predict the background, a data-driven normalization factor is computed as the ratio between opposite-charge to same-charge data event count in the CR of  $\text{BDT} < 0$ . The final prediction in the SRs then becomes the same-charge data event count in the SR multiplied by the normalization factor.

The computed normalization factor for phase 0 (2016) is  $1.12 \pm 0.044$  ( $1.037 \pm 0.05$ ) for muons (electrons), and for phase 1 (2017-2018) is  $1.066 \pm 0.024$  ( $1.049 \pm 0.03$ ) for muons (electrons). The relative errors on the normalization factors are between 2% to 5%.

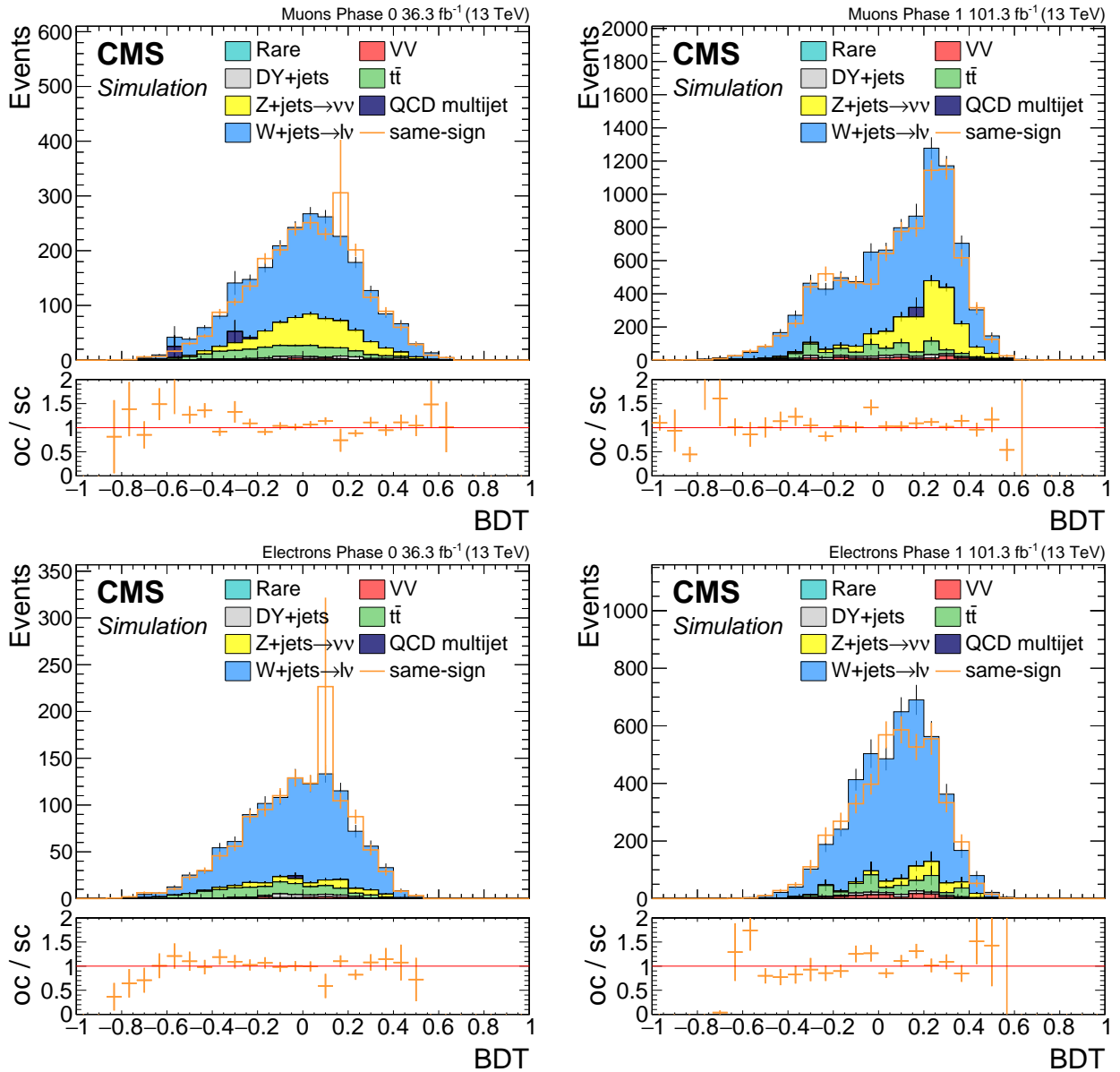


Figure 6.46: Exclusive track category closure tests for muons (top) and electrons (bottom) for phase 0 (left) and phase 1 (right). The stack represents standard model background for opposite-charge analysis lepton-track pair (oc), while the orange line represents same-charge lepton-track pair (sc). Both are weighted to represent each phase's luminosity. The ratio panel shows the ratio between opposite-charge to same-charge backgrounds for each bin.

## 6.10 Data control region plots

Monte Carlo simulation is being used in this analysis both to train the BDTs and to gain understanding of the composition of the standard model processes in the background. It is therefore useful to compare data and simulation plots to verify that the simulation does not significantly diverge from the data. However, to avoid unblinding the data in sensitive regions, the comparison plots are done in a CR. A straightforward CR is the same as the normalization region for the background estimation methods of  $\text{BDT} < 0$ . For this study, the most sensitive category, namely the dimuon category, was chosen. The data taking period used is tracker phase 1, which has higher luminosity and is expected to suffer from some data quality issues that are further addressed in Section 6.13. The simulation has been normalized for phase 1 luminosity, and the comparison plots can be seen in Figure 6.47. Good agreement between data and simulation can be observed in the ratio panel.

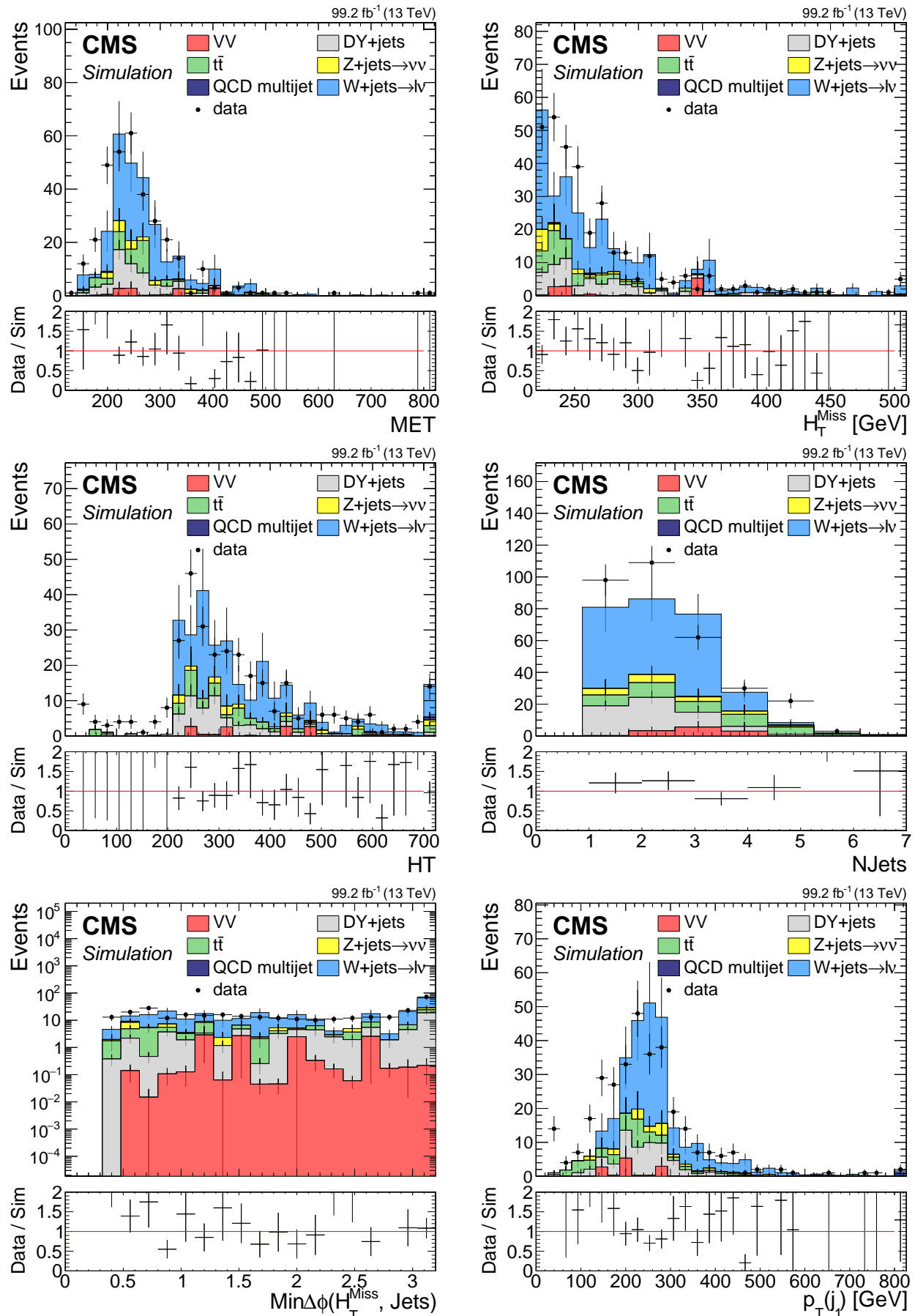
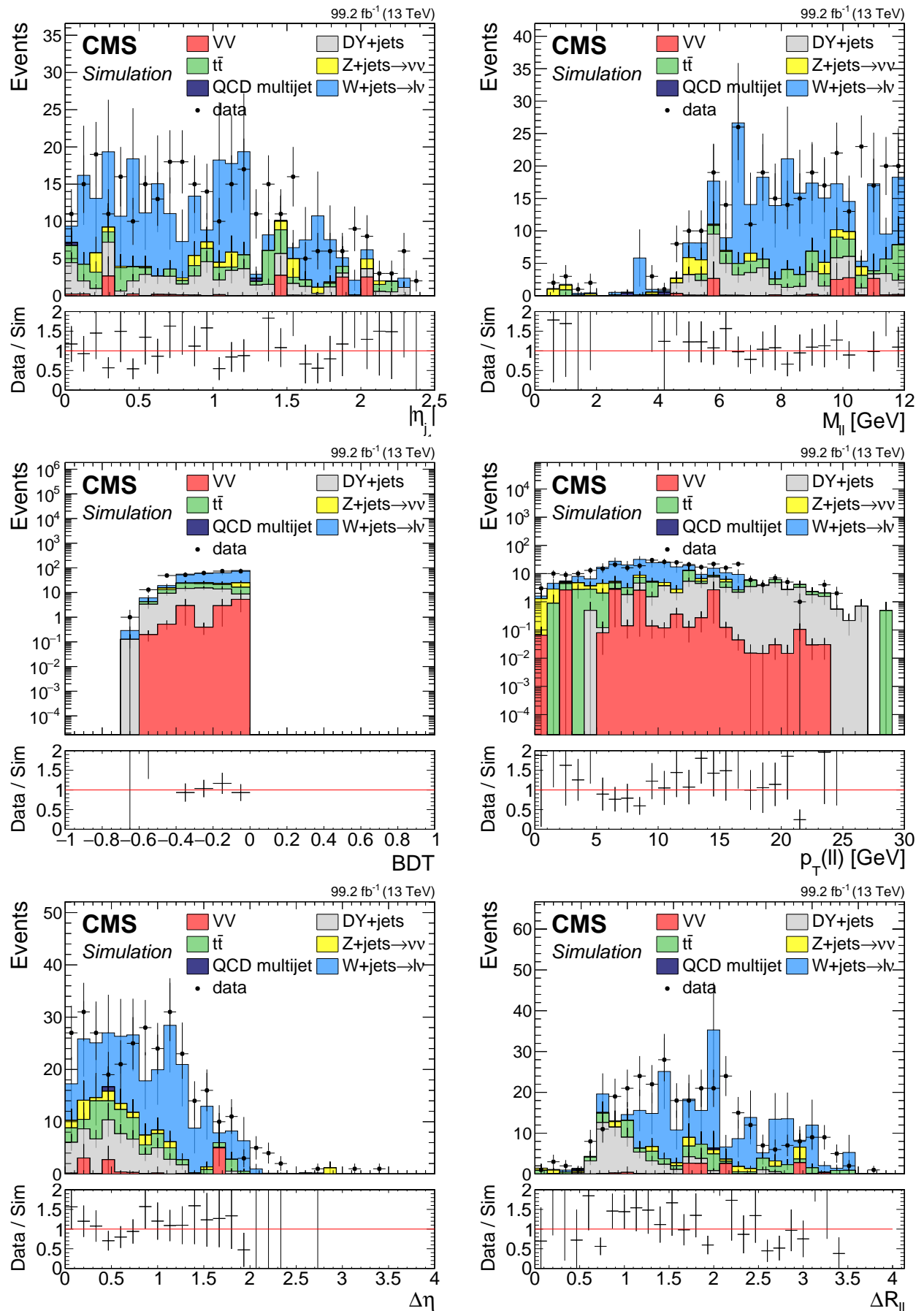


Figure 6.47: Data control region plots for dimuon category in phase 1.



## 6.11 Signal regions definition and optimization

The signal regions in this analysis consist of bins in the BDT output distributions with BDT output values greater than zero, and this type of search is sometimes referred to as a *shape analysis*. The significance is computed in each bin of the BDT output, and then the different values are statistically combined to produce a single significance value. Therefore, it is necessary to decide on the binning of the BDT output distribution. Since the most important factor in a beyond the standard model search like this one is the significance, it is desirable to find a binning that maximizes the significance or at least close to the supremum.

Because of the nature of how BDTs are trained, as the BDT value increases, so do the signal counts, while the background counts decrease. This means that the most significant bin will be closer to the right end of the distribution. The problem of finding an ideal binning is not as straightforward as one might think since the distributions are not smooth, but are made up of statistical events with potentially very low statistics. The first step in defining the SRs is defining the rightmost division that becomes the left edge of the most sensitive bin, stretching all the way up to the maximum BDT output value of 1. This is performed by first defining a step size  $\varepsilon$ . Then, a series of computations is performed, whereby in each step  $i$ , a significance is computed for a bin of size  $i \cdot \varepsilon$ , i.e., in the interval  $[1 - i \cdot \varepsilon, 1]$ . One can then pick the left bin by taking the maximum of the series of values resulting in the previous step.

There are a few points that need to be addressed. The first is which measure to choose for estimating the significance. Since the final significance, combination, and exclusion limit are calculated using the Higgs combination tool [18], an estimate is used for the purpose of optimization, which is reviewed in [19, 20] and referred to as the Z-value. The Z-value communicates the  $p$ -value by specifying the corresponding number of standard deviations in a one-tailed test of a Gaussian (normal) variate:

$$Z = \Phi^{-1}(1 - p) = -\Phi^{-1}(p). \quad (6.17)$$

Given the number of signal events count  $\hat{s}$ , background events count  $\hat{b}$  and its corresponding error  $\delta\hat{b}$ , an estimator for the significance is given by

$$Z = \frac{\hat{s}}{\sqrt{\hat{b} + \delta\hat{b}^2}}. \quad (6.18)$$

The background event count is estimated using the data-driven methods described in 6.9.2. They all involve counting events in a sideband and multiplying them by a transfer factor computed in a control region:

$$\hat{b} = N_{\text{sideband}}^{\text{SR}} \cdot \text{TF} \quad (6.19)$$

where the transfer factor TF is given by

$$\text{TF} = \frac{N_{\text{main band}}^{\text{CR}}}{N_{\text{sideband}}^{\text{CR}}} \quad (6.20)$$

The error propagation formula yields

$$\left( \frac{\delta\hat{b}}{\hat{b}} \right)^2 = \left( \frac{\delta N_{\text{sideband}}^{\text{SR}}}{N_{\text{sideband}}^{\text{SR}}} \right)^2 + \left( \frac{\delta \text{TF}}{\text{TF}} \right)^2, \quad (6.21)$$

which results in

$$\delta\hat{b}^2 = \hat{b}^2 \left[ \left( \frac{\delta N_{\text{sideband}}^{\text{SR}}}{N_{\text{sideband}}^{\text{SR}}} \right)^2 + \left( \frac{\delta \text{TF}}{\text{TF}} \right)^2 \right]. \quad (6.22)$$

The second point that needs to be addressed is the choice of which signal point or points to optimize. Each model point yields a different signal event count  $\hat{s}$  and therefore produces different significance values. To select the optimal values, a range of signal points is considered that are on the edge of the exclusion limit and maximize the significance.

The third and final point to address is what step size  $\varepsilon$  to choose. If a step size that is too small is picked, there will be steps where no events are encountered in either the signal or the background due to the low statistics nature of the problem as the BDT values are being scanned downwards from 1. Therefore, each signal event added will create a step upwards in the significance, while each background event will reduce it. This procedure will produce a highly-tuned value which is not believed to be maximizing the significance, but rather it will produce wildly different results given a different set of events (from a different simulation set, for example). To avoid overtraining, a step size of  $\varepsilon = 0.5$  was chosen since its behavior is regular in the sense that every step adds both signal and background events, while also maintaining granularity.

Lastly, after the most significant bin has been fixed, the remaining BDT range from 0 to the left edge of the significant bin is divided equally in order to pick up any sensitivity that might remain in those bins. For the dimuon category, the bin width is chosen as 0.1, while for the exclusive track categories, it is 0.05. The final signal regions are as follows:

Table 6.11: Signal Regions

Category	Flavor	Phase	SR	Signal Regions
Dilepton	Muons	all	6	[0, 0.1, 0.2, 0.3, 0.4, 0.5, 1]
Exclusive Track	Muons	0	13	[0, 0.05, 0.1, 0.15, 0.2, ⋯, 0.5, 0.55, 0.6, 1]
Exclusive Track	Muons	1	12	[0, 0.05, 0.1, 0.15, 0.2, ⋯, 0.5, 0.55, 1]
Exclusive Track	Electrons	all	11	[0, 0.05, 0.1, 0.15, 0.2, ⋯, 0.5, 1]

## 6.12 Systematic uncertainties

In an experimental analysis, most if not all of the measured and predicted observables have uncertainties associated with them. These uncertainties can be experimental in nature, such as an uncertainty on the reconstruction efficiency of the muons in the detector, or theoretical, such as an uncertainty on a cross section. As a general rule, an uncertainty that scales with the number of events is referred to as statistical, while one that cannot be reduced by increasing the statistics is referred to as a systematic uncertainty. It could well be that a statistical uncertainty in one study becomes a systematic uncertainty in another.

As mentioned, there are uncertainties associated with theoretical calculations and simulation mismodeling (both for FASTSIM and FULLSIM), among other factors. This analysis follows all the recommendations listed by the CMS SUSY Physics Analysis Group (PAG) [21], which includes the study of muon scale factors described in Section 6.6.3. In this section, only the systematic uncertainties that are unique to this analysis are introduced, aside from the muon scale factors. The systematic uncertainties in this analysis are primarily due to the background estimation methods used.

### 6.12.1 Data driven transfer factors

Data-driven background estimations are used in both the dimuon category, to estimate the jetty non-isolated background, and in the exclusive track background. They involve computing a transfer factor in a dedicated CR of  $BDT < 0$  and applying it in the SRs. The transfer factors are computed as the ratio between the data counts in the main band and the sideband. In the dimuon category, the sideband is the isolation sideband, as described in Section 6.9.2.1, and for the exclusive track category, the sideband is the same-charge sideband, as described in Section 6.9.2.3. These transfer factors have an associated uncertainty due to the statistics in the CR. Table 6.12.1 lists all transfer factors and their associated uncertainties.

Table 6.12: Transfer factors and their associated uncertainties

Method	Flavor	Phase	Transfer Factor	Uncertainty	Relative Error
Jetty	Muons	0	0.548	0.078	14.2%
Jetty	Muons	1	0.533	0.039	7.3%
$\tau\tau$	Muons	0	0.518	0.411	79%
$\tau\tau$	Muons	1	0.283	0.26	91.8%
Exclusive Track	Muons	0	1.12	0.044	3.9%
Exclusive Track	Muons	1	1.066	0.024	2.2%
Exclusive Track	Electrons	0	1.037	0.05	4.8%
Exclusive Track	Electrons	1	1.049	0.03	2.8%

### 6.12.2 Data driven shape uncertainties

In the section about the background estimation methods, it is explained that the data-driven methods rely on the assumption that the shape of the background in a sideband is the same as in the main band and, therefore, require only a normalization factor to correctly predict the background. The exclusive track category closure plots in Figure 6.46 show no trend, and neither does the Phase 1 closure plot of the jetty background in Figure 6.44. This is also supported by the line fit performed in the ratio panel, which is statistically consistent with a flat line intersecting 1.

In the dimuon category, only one BDT is trained using 2017 simulation, but evaluated for phase 0 (2016) as well. This introduces a slight trend when a line is fit in the ratio panel of the

closure plot in Figure 6.48. The line fit is then used to introduce weights that are applied in an event-by-event manner with the value of the line for the specific BDT value of the event. On the right side of Figure 6.48, one can see the closure plot after said weights have been applied, and it is clear that the trend has been successfully eliminated.

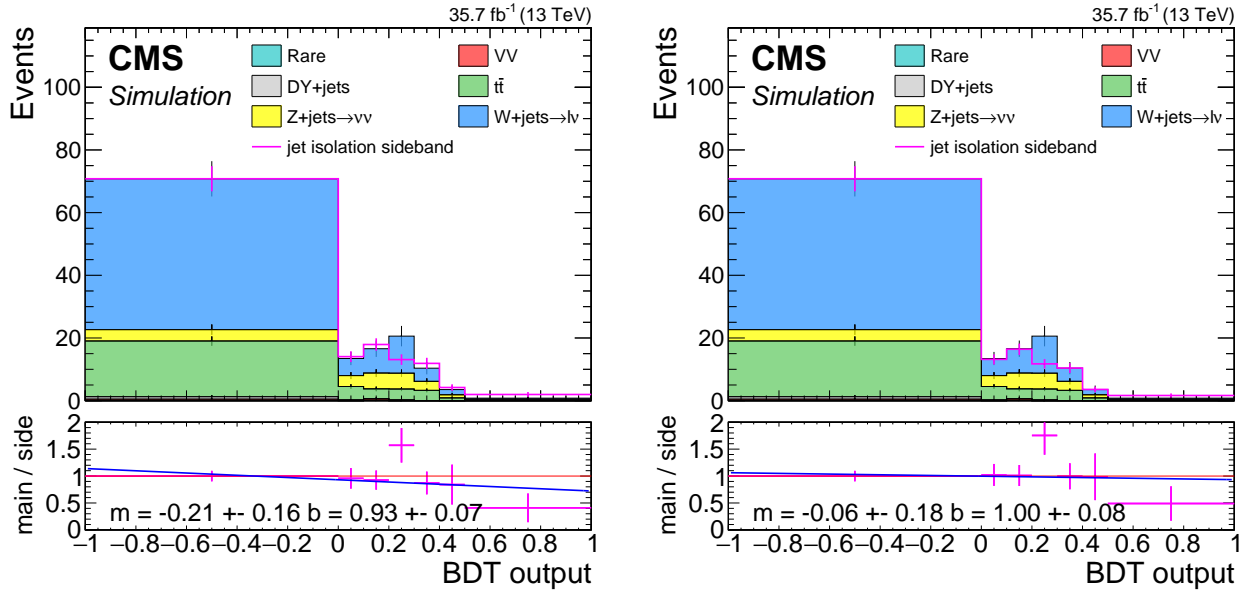


Figure 6.48: Dimuon 2016 jetty background closure plot with (right) and without (left) fit line weights. The stack represents simulation in the main isolation band after  $Z/\gamma^* \rightarrow \tau^-\tau^+$  has been removed, while the pink line represents simulation in the isolation sideband. The isolation sideband is normalized to match the isolation in the CR of  $\text{BDT} < 0$ . The ratio panel shows the ratio between the isolatoin main band and sideband. A line fit of the ratio is performed and the parameters of the slope  $m$  and interception point  $b$  with their respective errors are stamped. In the plot on the right, the line fit weights obtained from the fit on the left plot have been applied.

On top of the transfer factor uncertainties listed in Table 6.12.1, shape uncertainties taken from the line fits are also taken into account. For phase 1, since the closure plot line fit did not show any trend, the nominal values are taken without applying the line weights. For 2016, the nominal values are taken after the line weights were applied, i.e., from the right plot in Figure 6.48. The alternative prediction, which is fed into the combine tool as the shape systematic uncertainty, is for 2017 the histogram with the line weights applied, and for 2016, since the weights were already applied as the nominal value, the weights of the fit line with the slope varied by  $1\sigma$  are applied ( $m = -0.21 - 0.16 = -0.37$ ).

### 6.12.3 Simulated background uncertainties

The last background estimation method to consider is the  $\tau\tau$  background estimation, which uses simulation normalized to data in a CR, as explained in Section 6.9.2.2. For background methods that use simulation rather than data, normally a list of uncertainties associated with simulation uncertainties have to be applied. However, as could be seen in Figure 6.49, this background is non-existent in the most sensitive bin, and is very small in the rest of the bins. Therefore, the already very large uncertainties on this background (79%-92%) are dominant enough that all other uncertainties can be safely neglected.

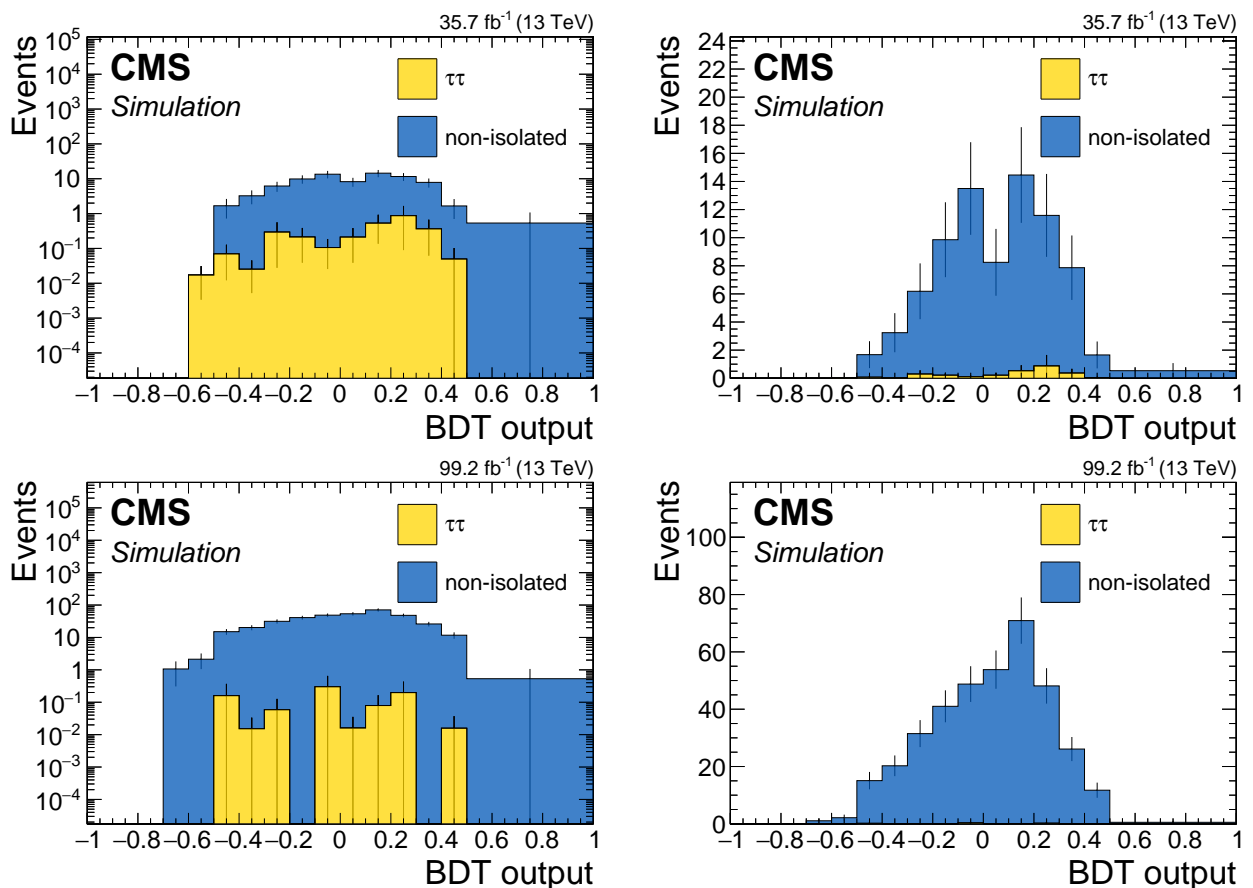


Figure 6.49: Dimuon full background prediction for phase 0 (top) and phase 1 (bottom) both in log scale (left) and linear scale (right). Blue represents the data-driven jetty non-isolated background, while yellow is the  $\tau\tau$  background.

## 6.13 Data quality aspects and background validation

During the run 2 data taking period of CMS, there have been a few detector issues that require some special care. Following the central recommendations, three issues are handled here, namely, L1 prefire rate in 2016 and 2017, ECAL Endcap (EE) noise in 2017, and the HE minus side (HEM) failure in 2018. In the process of dealing with these issues, the jetty background data-driven method is also validated in data.

### 6.13.1 L1 prefire issue in 2016 and 2017 data

The L1 prefire issue in 2016 and 2017 happened due to an ECAL timing error, which was propagated to the L1 trigger primitives. This issue occurred because the trigger system used data from the previous bunch crossing rather than the current one to determine whether an event should be triggered. Events with significant ECAL energy in the region  $2.5 < |\eta| < 3$  are affected in 2016 and 2017 data. This can lead to inefficiency and was studied for signal Monte Carlo samples, as it can potentially lower the signal event count. Prefiring weights were added to signal and checked against the unweighted events, and no significant effect was observed. Data was also checked with and without the prefiring weights for the most affected period of 2017 by looking at closure plots in a same-charge CR. This serves both to validate that the prefire issue does not affect this analysis and to act as a data validation for the jetty background. Plots can be seen in Section 6.13.4.

### 6.13.2 EE noise in 2017 data

In 2017 data, an observed excess of fake  $p_T^{\text{miss}}$  compared to simulation was caused by increased noise in low- $p_T$  jets. Additional noise in the ECAL endcaps in data was identified as the cause of this effect. To deal with this issue, the recommendation is to recalculate  $p_T^{\text{miss}}$ , excluding jets in the affected phase space. This was done centrally in the process of creating the samples used in this analysis.

### 6.13.3 HEM failure in 2018 data

Following the power interruptions generated by false fire alarms on Saturday, June 30th, negative endcap Hadron Calorimeter (HCAL) sectors HEM15 and HEM16 could no longer be operated until the end of the 2018 run. The affected  $\eta - \phi$  region is  $-3.0 < \eta < -1.3$  and  $-1.57 < \phi < -0.87$ . The first regular physics run affected is 319077. Data and simulation vetoes for objects in the affected region are applied. Same-sign validation plots are made pre-HEM and post-HEM in order to see their effects. The well-behaved validation plots suggest that this analysis is not badly affected by this issue.

### 6.13.4 Same-sign validation plots

Figure 6.50 shows data validation plots for the same-charge control region. They serve both as background method validation and to check the data taking issues mentioned above. The plots are divided into different data taking periods to check the effects of the data taking issues. The same-sign control region has been selected since it can validate the assumption that the isolation sideband properly predicts the shape of the main band and can therefore be used as the estimation method. Overall, good shape agreement is demonstrated between the main band and the isolation sideband.

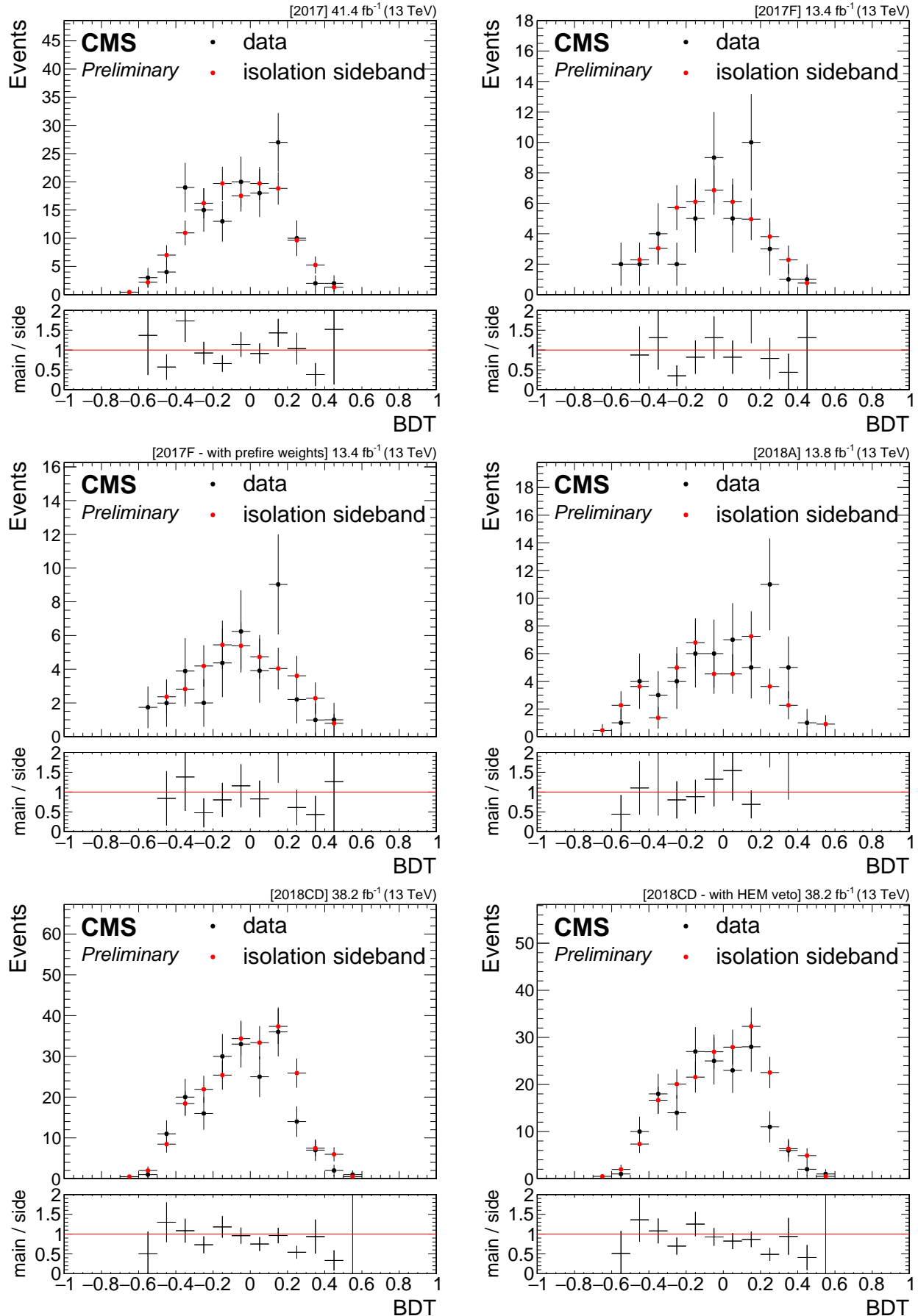


Figure 6.50: Data same sign control validation plots. Black dots show same sign data in the main band, while red dots show same sign data in the isolation side band, normalized in the  $\text{BDT} < 0$  region. Ratio panel shows the ratio between them. Going line by line from left to right, the corresponding plots are shown: 2017 data taking period, 2017F data taking period, 2017F data taking period with prefire weights, 2018A data taking period (pre HEM), 2018CD data taking period (post HEM), 2018CD data taking period with HEM veto (post HEM).

## 6.14 Results and interpretation

# Chapter 7

## Summary



# Chapter 8

## Latex stuff

### 8.1 Some examples

#### 8.1.1 Multiline comment

This is a line in introduction.

#### 8.1.2 Fixme note

This is the introduction to the thesis. **FiXme Note:** This is a fixme note **FiXme Note:** what **FiXme Note:** WHAT THE HELL AFTER

#### 8.1.3 Tables

h - here t - top b - bottom p - special page ! - even if not pretty

Table 8.1: Table captions are above the table whereas figure captions are below.

Parameter	Value 1	Value 2
$s$	10.0	20.0
$t$	20.0	30.0
$u$	30.0	40.0

#### 8.1.4 Cross References

8.1.4 85 section 8.1.4

#### 8.1.5 Particles

Hello World  $\tilde{\chi}_1^0 \pi \eta_c$  GeV  $E_T^{\text{miss}}$  hey GeV  $E_T^{\text{miss}}$   $\pi$  new one  $\tilde{\chi}_1^0 \tilde{\chi}_1^0$

#### 8.1.6 Citing

[1] SOS analysis

#### 8.1.7 Glossary

Using glossary for computer plural form computers upper case first Computer upper case first plural Computers. To use for symbol  $\pi$

### 8.1.8 Acronyms

First use of acronym SOS and second SOS. You can reset this and do again Soft-Opposite-Sign (SOS) and second time again SOS. Long version Soft-Opposite-Sign. Full version Soft-Opposite-Sign (SOS). Short version SOS.

### 8.1.9 fractions

Here's a fraction with a slash:

$$\text{Track Isolation}_\ell = \sum_{\substack{\text{tracks from PV} \\ \text{in } \Delta R < 0.3}} p_T / p_T(\ell) \quad (8.1)$$

### 8.1.10 Quarantine

From 7.5.1

A Weakly Interacting Massive Particle (WIMP) is a new elementary particle that interacts via gravity and potentially other forces, not part of the SM itself, and is as weak as or weaker than the weak nuclear force, but also non-vanishing in strength. This essentially means that such a candidate is neutral and does not interact via the electromagnetic force.

# List of Corrections

Note: fill in signal model stuff . . . . .	11
Note: make sure we define the different deltaM somewhere . . . . .	11
Note: This is a fixme note . . . . .	85
Note: what . . . . .	85
Note: WHAT THE HELL . . . . .	85



# Glossary

**computer** is a programmable machine that receives input, stores and manipulates data, and provides output in a useful format. 85

**$\Delta m$**  mass difference between electroweakinos. If not explicitly said otherwise, it is the mass difference between  $\tilde{\chi}_2^0$  and  $\tilde{\chi}_1^0$ , i.e.,  $\Delta m = \Delta m^0 = m_{\tilde{\chi}_2^0} - m_{\tilde{\chi}_1^0}$ . 26, 27, 31

**$\Delta m^0$**  mass difference between the neutral electroweakinos  $\tilde{\chi}_2^0$  and  $\tilde{\chi}_1^0$ , i.e.,  $\Delta m^0 = m_{\tilde{\chi}_2^0} - m_{\tilde{\chi}_1^0}$ . 26

**$\Delta R$**  separation. 18, 21, 22, 24

**$\eta$**  pseudorapidity. 21

**$E_T^{\text{miss}}$**  add description. 13, 14

**$H_T^{\text{miss}}$**  add description. 13, 14, 50

**$m_{\ell\ell}$**  invariant mass. 18, 20

**neutralino** add description. 13

**$\phi$**  azimuthal angle measured in radians. 21

**$\pi$**  ratio of circumference of circle to its diameter. 85

**$p_T$**  transverse momentum. 13, 17, 22, 26, 27, 31



# Acronyms

- ATLAS** A Toroidal LHC Apparatus. 67
- BDT** Boosted Decision Tree. 31, 41–43, 51–53, 55, 58–60, 62, 65, 70, 72, 75, 77, 78
- CERN** European Organization for Nuclear Research. 7
- CMS** Compact Muon Solenoid. 7, 45, 67, 77, 80
- CR** Control Region. 64–68, 70, 72, 77, 78, 80
- CSV** Combined Secondary Vertex. 40
- DM** Dark Matter. 13
- ECAL** Electromagnetic Calorimeter. 27, 80
- HCAL** Hadron Calorimeter. 80
- ISR** Initial State Radiation. 13, 14, 26, 27, 50, 51, 67
- LHC** Large Hadron Collider. 7
- LSP** Lightest Supersymmetric Particle. 13
- MC** Monte Carlo. 35, 36, 46, 52, 59, 64, 66, 67
- PAG** Physics Analysis Group. 77
- PF** Particle Flow. 40
- POG** Physics Object Group. 35, 36
- PU** Pile-Up. 40, 45
- QCD** Quantum Chromodynamics. 13, 14, 50, 59
- SF** Scale Factor. 35
- SM** Standard Model. 13, 14, 21, 24, 33, 34, 50–52, 58, 86
- SOS** Soft-Opposite-Sign. 20–23, 51, 86
- SR** Signal Region. 52, 58–60, 64–66, 70, 75, 77
- SUSY** Supersymmetry. 13, 77
- WIMP** Weakly Interacting Massive Particle. 86



# Bibliography

- [1] CMS Collaboration, A. Tumasyan *et al.*, “Search for supersymmetry in final states with two or three soft leptons and missing transverse momentum in proton-proton collisions at  $\sqrt{s} = 13$  TeV,” *JHEP* **04** (2022) 091, arXiv:2111.06296 [hep-ex].
- [2] [https://gitlab.cern.ch/cms-muonPOG/MuonReferenceEfficiencies/-/tree/master/EfficienciesStudies/2016\\_legacy\\_rereco/Jpsi](https://gitlab.cern.ch/cms-muonPOG/MuonReferenceEfficiencies/-/tree/master/EfficienciesStudies/2016_legacy_rereco/Jpsi).
- [3] <https://indico.cern.ch/event/791428/contributions/3287172/attachments/1781977/2899551/2016LegacyReReco2.pdf>.
- [4] BRIL Group, “Bril work suite.”  
<http://cms-service-lumi.web.cern.ch/cms-service-lumi/brilwsdoc.html>, 2017.
- [5] [https://lguzzi.web.cern.ch/lguzzi/Tau3Mu/muonPOG\\_mediumID\\_dR.pdf](https://lguzzi.web.cern.ch/lguzzi/Tau3Mu/muonPOG_mediumID_dR.pdf).
- [6] T. C. collaboration, “Performance of the CMS missing transverse momentum reconstruction in pp data at  $\sqrt{s} = 8$  tev,” *Journal of Instrumentation* **10** no. 02, (Feb, 2015) P02006–P02006. <https://doi.org/10.1088%2F1748-0221%2F10%2F02%2Fp02006>.
- [7] M. Cacciari, G. P. Salam, and G. Soyez, “The anti-kt jet clustering algorithm,” *Journal of High Energy Physics* **2008** no. 04, (Apr, 2008) 063–063.  
<https://doi.org/10.1088%2F1126-6708%2F2008%2F04%2F063>.
- [8] A. Hoecker, P. Speckmayer, J. Stelzer, J. Therhaag, E. von Toerne, H. Voss, M. Backes, T. Carli, O. Cohen, A. Christov, D. Dannheim, K. Danielowski, S. Henrot-Versille, M. Jachowski, K. Kraszewski, A. Krasznahorkay, M. Kruk, Y. Mahalalel, R. Ospanov, X. Prudent, A. Robert, D. Schouten, F. Tegenfeldt, A. Voigt, K. Voss, M. Wolter, and A. Zemla, “Tmva - toolkit for multivariate data analysis,” 2007.  
<https://arxiv.org/abs/physics/0703039>.
- [9] <https://twiki.cern.ch/twiki/bin/view/CMS/SWGuideMuonIdRun2>.
- [10] S. Chatrchyan, , V. Khachatryan, and A. M. et. al, “Search for new physics with same-sign isolated dilepton events with jets and missing transverse energy at the LHC,” *Journal of High Energy Physics* **2011** no. 6, (Jun, 2011) .  
<https://doi.org/10.1007%2Fjhep06%282011%29077>.
- [11] K. Rehermann and B. Tweedie, “Efficient identification of boosted semileptonic top quarks at the LHC,” *Journal of High Energy Physics* **2011** no. 3, (Mar, 2011) .  
<https://doi.org/10.1007%2Fjhep03%282011%29059>.
- [12] R. Ellis, I. Hinchliffe, M. Soldate, and J. Van Der Bij, “Higgs decay to  $\tau^+\tau^-$ -a possible signature of intermediate mass higgs bosons at high energy hadron colliders,” *Nuclear Physics B* **297** no. 2, (1988) 221–243.  
<https://www.sciencedirect.com/science/article/pii/0550321388900193>.

- [13] **ATLAS** Collaboration, G. Aad *et al.*, “Expected Performance of the ATLAS Experiment - Detector, Trigger and Physics,” arXiv:0901.0512 [hep-ex].
- [14] **CMS** Collaboration, G. L. Bayatian *et al.*, “CMS technical design report, volume II: Physics performance,” *J. Phys. G* **34** no. 6, (2007) 995–1579.
- [15] Z. Han, G. D. Kribs, A. Martin, and A. Menon, “Hunting quasidegenerate higgsinos,” *Physical Review D* **89** no. 7, (Apr, 2014) .  
<https://doi.org/10.1103%2Fphysrevd.89.075007>.
- [16] H. Baer, A. Mustafayev, and X. Tata, “Monojet plus soft dilepton signal from light higgsino pair production at LHC14,” *Physical Review D* **90** no. 11, (Dec, 2014) .  
<https://doi.org/10.1103%2Fphysrevd.90.115007>.
- [17] A. Barr and J. Scoville, “A boost for the EW SUSY hunt: monojet-like search for compressed sleptons at LHC14 with 100 fb-1,” *Journal of High Energy Physics* **2015** no. 4, (Apr, 2015) . <https://doi.org/10.1007%2Fjhep04%282015%29147>.
- [18] <https://cms-analysis.github.io/HiggsAnalysis-CombinedLimit/>.
- [19] L. Demortier, “P values and nuisance parameters,” in *Statistical issues for LHC physics. Proceedings, Workshop, PHYSTAT-LHC, Geneva, Switzerland, June 27-29, 2007*, p. 23. 2008. <http://cds.cern.ch/record/1099967/files/p23.pdf>.
- [20] R. D. Cousins, J. T. Linnemann, and J. Tucker, “Evaluation of three methods for calculating statistical significance when incorporating a systematic uncertainty into a test of the background-only hypothesis for a Poisson process,” *Nucl. Instrum. Meth. A* **595** (2008) 480, arXiv:physics/0702156 [physics.data-an].
- [21] <https://twiki.cern.ch/twiki/bin/view/CMS/SUSRecommendationsRun2LegacyTable>.

# List of Figures

6.1	Signal Models Feynman Diagrams . . . . .	11
6.2	Signal $E_T^{\text{miss}}$ and $H_T^{\text{miss}}$ distributions . . . . .	14
6.3	Signal number of jets and leading jet $p_T$ distributions . . . . .	15
6.4	Signal number of $b$ -tagged jets distributions . . . . .	15
6.5	Signal $\min \Delta\phi(\vec{E}_T^{\text{miss}}, \vec{j})$ and $\min \Delta\phi(\vec{H}_T^{\text{miss}}, \vec{j})$ distributions . . . . .	16
6.6	Signal $p_T$ distributions . . . . .	17
6.7	Signal $p_T$ distributions split into barrel and endcaps . . . . .	18
6.8	Signal $ \eta $ distributions . . . . .	19
6.9	Signal generator level $m_{\ell\ell}$ distributions . . . . .	20
6.10	Signal $m_{\mu\mu}$ vs. $p_T$ . . . . .	21
6.11	Distributions of reconstructed $m_{\mu\mu}$ in signal events . . . . .	22
6.12	Signal generator level $\Delta R$ distributions . . . . .	22
6.13	Event distributions in the plan of $\Delta R(\mu\mu)$ vs. $p_T$ for signal models . . . . .	23
6.14	Distributions of the reconstructed $\Delta R(\mu\mu)$ in signal events . . . . .	23
6.15	Spatial seperation between reconstructed electrons and the leading jet $\Delta R(j_1, e)$ . . . . .	26
6.16	$p_T$ distribution of reconstructed electrons with loose ID . . . . .	27
6.17	$ \eta $ distribution of reconstructed electrons with loose ID . . . . .	27
6.18	medium and tight ID working points distribution of reconstructed electrons . . . . .	28
6.19	standard isolation and jet-isolation distribution of reconstructed electrons . . . . .	29
6.20	$ \eta $ distribution of reconstructed electrons with loose ID passing jet-isolation . . . . .	29
6.21	Spatial seperation between reconstructed muons and the leading jet $\Delta R(j_1, \mu)$ . . . . .	31
6.22	Reconstructed muons $p_T$ . . . . .	32
6.23	$ \eta $ distribution of reconstructed muons with loose ID before and after $p_T > 2 \text{ GeV}$ cut . . . . .	32
6.24	medium ID working point distribution of reconstructed muons . . . . .	33
6.25	tight ID working point distribution of reconstructed muons . . . . .	33
6.26	jet-isolation distribution of reconstructed muons . . . . .	34
6.27	Simluation barrel muons fits . . . . .	37
6.28	Simluation endcaps muons fits . . . . .	37
6.29	Data barrel muons fits . . . . .	38
6.30	Data endcaps muons fits . . . . .	38
6.31	Efficiencies and scale factors . . . . .	39
6.32	Muon track BDT training inputs . . . . .	42
6.33	Track BDT output plots . . . . .	43
6.34	Track BDT ROC curves . . . . .	44
6.35	Dimuon BDT output and ROC curve . . . . .	53
6.36	dimuon training input distribution . . . . .	54
6.37	Exclusive track category BDT outputs . . . . .	55
6.38	Exclusive track category ROC curve . . . . .	56
6.39	exclusive track training input distribution . . . . .	57

6.40 Dimuon simulation BDT output . . . . .	60
6.41 Dimuon simulation BDT inputs . . . . .	61
6.42 Exclusive track plus muon 2017 simulation BDT output . . . . .	62
6.43 Exclusive track plus muon simulation BDT inputs . . . . .	63
6.44 Dimuon 2017 jetty background closure plot . . . . .	66
6.45 Ditau invariant mass distributions . . . . .	69
6.46 Exclusive track category closure tests . . . . .	71
6.47 Data control region plots for dimuon category in phase 1 . . . . .	73
6.48 Dimuon 2016 jetty background closure plots with and without fit line weights . .	78
6.49 Dimuon full background prediction for both phases . . . . .	79
6.50 Data same sign control validation plots . . . . .	81

# List of Tables

6.1	The preselection criteria, which are applied to all analysis categories.	15
6.2	Generator level efficiency on muons selections	20
6.3	Selection criteria for Tags and Probes	36
6.4	Track BDT input variables	42
6.5	Signal Efficiency	46
6.6	Background Efficiency	47
6.7	Transfer Factor	47
6.8	Significance $s/\sqrt{b + \epsilon_b^2}$	48
6.9	Dimuon BDT input variables	53
6.10	Exclusive track BDT input variables	56
6.11	Signal Regions	76
6.12	Transfer factors and their associated uncertainties	77
8.1	Table captions are above the table whereas figure captions are below.	85